Estimation of Energy Released from Crack in Concrete using Acoustic Emission and Comparison with the Numerical Results

MSc Thesis Report

Jayant Srivastava

TU Delft

Estimation of Energy Released from Crack in Concrete using Acoustic Emission and Comparison with the Numerical Results

by

Jayant Srivastava

to obtain the degree of Master of Science
at the Delft University of Technology,
defended publicly on 29th October 2020.

Student Number: 4799283

Thesis Committee:		
	Dr. Ir. Y. Yang	Chair of the Committee
	Dr. Ir. M.A.N. Hendriks	Supervisor
	Ir. F. Zhang	Daily Supervisor

TU Delft

Preface

This thesis work marks the end of my master's degree at Delft University of Technology. This eleven-month long journey has been unforgettable. The experience has been an academically rewarding one and has also allowed me to grow on a personal level. During this period, I have learned to handle new challenges and push my limits further. Finishing the thesis work during the pandemic made the task even harder, but with the support of people around me I completed this journey as planned.

I would like to thank the chair of my thesis committee, Yuguang Yang. He helped me design the thesis topic based on my interests, which allowed me work on this interesting project. I am also thankful for his invaluable suggestions and constructive feedbacks during the progress meetings, which helped me develop better insight about my research. His creative opinions helped me present my results in a more interactive manner.

I would also like to express my gratitude towards my daily supervisor, Fengqiao Zhang. It was her patience and constant support which helped me steer through the difficult parts of my research. She gave me enough time to develop my own ideas and gave valuable inputs to improve on those ideas. In addition to this, she also invested her time in helping me design my thesis report and helped me organize the progress meetings effectively. She has been a good friend during the whole journey.

Further, I would like to extend my gratitude towards Max Hendriks for his inputs and support during the thesis. His creative remarks have helped me develop novel methods and have also helped me structure my thesis in a much better format.

I would also like to thank my mother, father and brother for keeping faith in me and providing unconditional support. They have kept me motivated during this journey far away from home. In the end, I would also like to thank my friends with whom I could discuss my thesis related issues and share my problems. They have helped make this journey at TU Delft a memorable one.

Jayant Srivastava
Delft, October 2020

Abstract

Study relating Acoustic Emission (AE) energy to fracture energy has been conducted in the past and a correlation has been reported between the two. The scope of these studies has remained limited to laboratory size specimens with known crack location and the energy release being investigated on a global scale. The objective of this research is to track the local energy release due to cracking in concrete using AE monitoring and understand the relationship between AE energy and crack energy estimated using nonlinear FE model. This will allow to keep the track of energy release due to cracking and use AE energy as a measure for the structural health condition. The study involves challenges with respect to AE source identification, estimating AE energy at source location accounting for attenuation losses and estimating local energy in the numerical model. These issues are discussed in detail in this thesis and the use of AE in crack monitoring is critically examined.

In the first part of the thesis, AE source classification methods including signal-based approach and parameter-based approach are reviewed. The classification methods help distinguish the AE activities due to crack opening from ones related to friction. An approach for signal-based AE classification using the AE signal in the frequency domain is proposed. This approach is then compared to existing bivariate and multivariate parameter-based classification methods. In addition to this, a novel partial power-based method for AE source classification is also proposed. The existing parameter-based classification methods are found to have a similarity of less than 50% in case of bivariate methods and a little over 50 % in the case of the multivariate method when compared to the signal-based method. This is because these methods are unable to notice small differences in AE signals. On the other hand, the partial power-based method has a similarity of about 75 % to the signal-based method. In addition to this, the partial power-based method is much faster than the signal-based approach, thus providing a good alternative to the existing AE classification methods.

In the second part, attenuation in AE signals is studied. Experiments on sound concrete and cracked concrete have been performed to study the attenuation in concrete media and through a crack, respectively. AE attenuation due to elastic wave propagation is made under the assumption of a Rayleigh wave and the material attenuation factor (α) is estimated to be 2.473 m^{-1}. Crack attenuation factor (C.A.F.) is introduced to determine the energy loss through a crack. Auto Sensor Test (AST) measurements made during the experiment were used to estimate C.A.F. AST measurements are found to be sensitive to the strain changes within the concrete and are thus able to predict the occurrence of the crack in advance.

In the last part, a methodology to estimate the local energy release in the numerical model is proposed and then verified using a notched beam as a test model. A rotating crack approach for modelling is adopted with tension behaviour defined using the Hordijk curve. The proposed methodology is applied to the girder model to estimate the energy released locally. The numerical energy trend thus calculated is compared to the AE energy trend at the crack location. The AE energy predicts the occurrence of the first flexure crack at 90% of the cracking load as per numerical energy. A possible explanation for this is that AE can also detect the presence of the

microcracks, which the current numerical model cannot. On comparing the estimated energies released due to AE and numerical model in the flexure zone it can be concluded that the relationship between the AE energy and numerical energy is non-linear. Local energy release trend for AE and the numerical model with increasing load is similar when the flexure cracks are generated, although slight deviations start to occur when the shear crack is created.

Nomenclature

Abbreviations

SHM	Structural Health Monitoring
AE	Acoustic Emission
AF	Average Frequency
JCMS	Japan Construction Material Standards
PCs	Principal Components
PCA	Principal Component Analysis
SVD	Singular Value Decomposition
AST	Auto Sensor Test
UT	Ultrasonic Testing
GMM	Gaussian Mixture Modelling
PAC	Physical Acoustics Corporation
SHSM	Sensor Highway II- Smart Monitoring
NLFEA	Non-Linear Finite Element Analysis
CAF	Crack Attenuation Factor

Greek Letter

α	Material attenuation factor
$\varepsilon_{1,2}$	Principal strain components
$\sigma_{1,2}$	Principal stress components
θ_p	Principal strain angle at integration point
$\theta_{p,element}$	Principal strain angle at element level
σ_{xx}, σ_{yy}, σ_{xy}	Local axis stress components
ε_{xx}, ε_{yy}, ε_{xy}	Local axis strain components
ν	Poisson ratio

Roman Letter

$V(t)$	Voltage signal
z_G	Grid point location
z_R	Sensor location
c	Wave velocity
N	Number of sensors
t_i	Signal arrival time
cc	Cross-correlation coefficient
n	Signal length
d	Dissimilarity coefficient

d_o	Maximum cophenetic distance
r_i	Radial distance from Source
A_i	Peak amplitude
E_i	Energy in the signal
ΔU_{strain}	Change in strain energy per unit volume
ΔU_{intpt}	Change in energy stored at integration point
U_{intpt}	Total energy stored at integration point
$U_{diss,intpt}$	Energy dissipated at integration point
$\Delta U_{specimen}$	Change in energy stored in the specimen
$U_{Total,specimen}$	Total energy stored in the specimen
$U_{Elastic}$	Stored elastic energy
U	Energy dissipated in the specimen
b	Element height
l	Element length
f_{ct}	Concrete tensile strength
G_f	Mode-I fracture energy of concrete
f_c	Concrete compressive strength

List of Figures

List of Tables

Table of Contents

1 Introduction

This chapter gives a brief introduction of the field of research, outlines the main objectives of the research and explains the procedure adapted to try and answer the formulated research questions.

1.1 Acoustic Emission (AE) Monitoring in Concrete

The second half of the 20th century saw a significant rise in the number of infrastructural facilities, constructed using reinforced or prestressed concrete. Figure 1.1 shows an overview of the bridges constructed in the Netherlands in the last few decades. Many of these concrete structures in the Netherlands and around the world are now exceeding their planned service life. Due to this reason, these structures need to be replaced or repaired in the near future[1]. In the European Union itself, nearly 84,000 reinforced and prestressed concrete bridges require repair and strengthening [2]. Replacing these structures to keep up with prognosticated growth requires huge investment. But to meet the rising economic pressure, these structures need to continue serving [3][4]. Thus, arises a need to increase the service life of the structures without compromising the safety requirements. To meet the specified objective a real-time evaluation of damage detection in the concrete structures, Structural Health Monitoring (SHM) was introduced [5]. The goal of SHM is to identify and quantify the damage to the structure over its service life [6]. Damage quantification in the existing structures is of high importance to determine whether a structure is in immediate need of repair [7]. This will allow in providing the maintenance to these structures on an as-needed basis instead of periodic basis, thus reducing the maintenance cost [8].

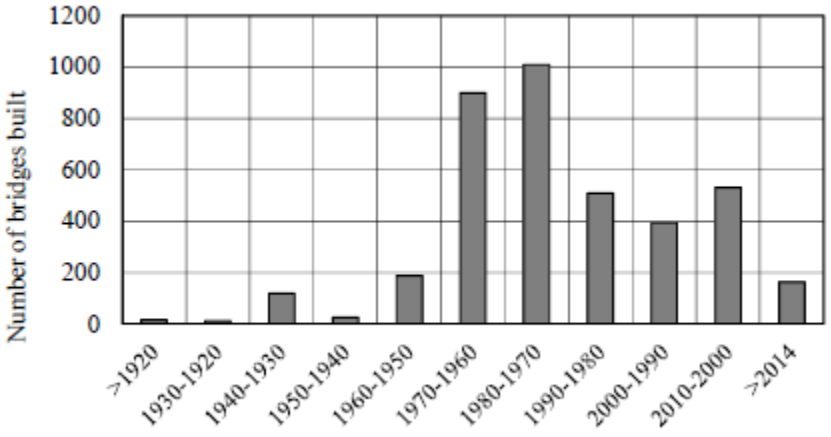

Figure 1.1: Overview of Dutch bridges constructed in the last decades [1]

Acoustic Emission (AE) is being widely used as a tool for Structural Health Monitoring (SHM) in the field of civil engineering [9]. The concept of AE refers to the rapid release of energy, in the form of elastic stress waves, due to mechanical deformations within the material [10]. These elastic waves are then detected using sensors and recorded in the form of an electrical signal. Such individual activities occurring inside the material are referred to as AE event. Acoustic Emission (AE) is a 'passive' technique for identifying the defects in the concrete structure [11][12]. This means that AE can identify the damage processes during the entire loading history, without causing any disturbance to the experiment. This is advantageous when compared to 'active'

techniques like ultrasonic testing (UT) which can be performed only at the start or the end of the loading.

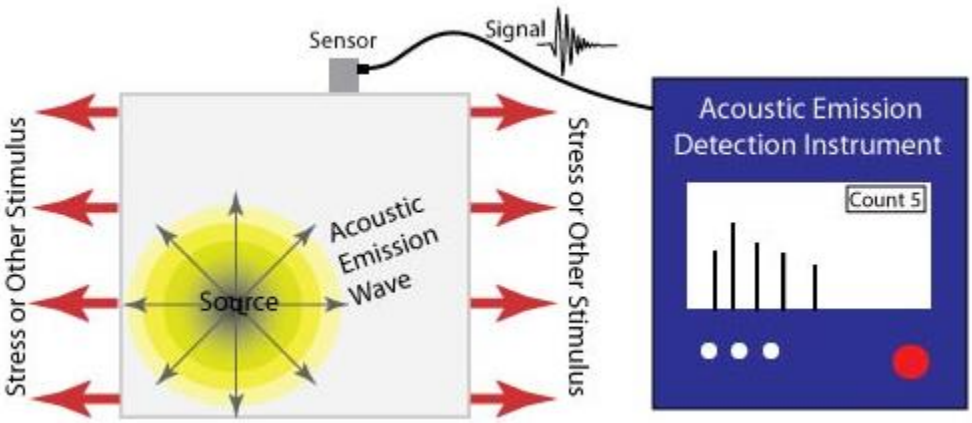

Figure 1.2: Typical AE Acquisition setup [13]

In a history extending over more than 50 years, AE has been thoroughly applied in the field of civil engineering. Ohtsu [9] and Behnia et al [14] have given a detailed overview of the usage of AE based methods in the field of civil engineering, with focus on concrete structures. AE monitoring has already been implemented in concrete structures to study crack source location [15]–[17], source discrimination [18]–[24], and severity of damage [25]–[27]. Landis and Baillon [28] used AE energy as a measure of fracture in concrete and it was found to provide a good measure for failure in concrete. Other researchers [29]–[32] have reported similar observation for concrete under bending as well as compression.

AE energy is influenced by the concrete microstructure which affects the failure mechanism; thus, AE is supposed to provide a good account of failure in concrete [32]. Study relating the bulk fracture energy with the energy released at microstructure level using AE has already been performed on laboratory size notched beam specimen. The results obtained show a promising relation between released AE energy and estimated fracture energy. This provides the motivation to further investigate the released AE energy in a larger specimen, thus taking a step forward in implementing AE energy-based fracture monitoring to real-life structures.

1.2 Research Objective and Scope

Although research has already been performed to link the released AE energy to the fracture energy in concrete [28]–[32], the scope of these studies has remained limited. Researchers have limited their work to mostly notched beam specimen under three-point bending. Thus, the location of the crack (or AE event) was known beforehand. In this thesis, the experiments conducted on the beams obtained from the Helperzoom viaduct are referred to. Thus, the crack location is not known beforehand. Also, in the previous studies, AE on a global scale (specimen level) was focused upon, whereas in this thesis local AE energy released along the cracks is studied, which enables us to keep track of energy release along the crack tip.

Proper account for energy attenuation in concrete has not been made yet. Researchers such as Landis [28] and Vidyasagar [33] have acknowledged the presence of attenuation in their studies but have mostly limited themselves to existing theoretical formulations. AE attenuation has also not been included in existing literature due to small specimen size (depth=100-200 mm). Due to the small size of the specimen, the released AE elastic waves do not have to travel for a larger distance before reaching the sensor, thus the propagation-based energy losses are not significant. This study aims towards providing a proper account of energy attenuation occurring in the prestressed concrete girder (depth=1100 mm) in the uncracked as well as in the cracked state. Thus, focusing on attenuation due to propagation and attenuation due to cracking in concrete.

As mentioned earlier, the AE waves generated in a structure can be associated with several factors, which can be related to crack opening or friction. To determine the energy released only due to cracking from total energy received by the sensors, secondary AE hits (hits which are a result of friction) must be differentiated. Thus, in this thesis, the AE source classification methods are discussed in detail to separate the AE events due to tension and friction. Existing parameter-based methods for AE source classification are reviewed and compared with the proposed signal-based classification method.

AE study is primarily performed using two approaches: AE parameter-based approach and AE signal-based approach. In the case of the parameter-based approach, the information about the AE activities is reduced to a limited number of parameters. Thus, compromising the available information. Signal waveform approach, on the other hand, utilizes the whole waveform recorded by AE sensors. Thus, enabling departure from reliance on the statistical methods. Availability of computers with advanced computational processor nowadays makes the signal-based study an attractive choice. In this thesis, the AE signal waveform approach is focused upon.

A part of this thesis also focusses on comparing the energy released locally as estimated from AE to local energy release in a finite element model. A detailed numerical analysis of existing structures can be computationally expensive, and it also requires exact knowledge of the material inputs which is often not available for structures built a few decades back. A comparison is thus made to test the applicability of AE measurement to indicate energy released at a local level due to crack. In this thesis, the rotating crack approach for crack modelling is implement with concrete fracture defined using the Hordijk softening curve.

1.3 Research Questions

To meet the abovementioned research objectives, the following research questions are formulated and are answered in this thesis.

1. How to account for the energy attenuation of the detected AE signal at the sensor location in uncracked as well as cracked concrete media and use the attenuation relationship to determine AE energy release along the crack path?
    - The first step is to determine the AE energy loss due to attenuation in the concrete beam. Firstly, the attenuation in energy due to propagation is estimated in the uncracked stage. This includes the energy loss due to geometrical spreading as well as material scattering. Then, the attenuation through cracks is determined using the Auto-Sensor Test (AST)

measurements made during the experiment. The measured losses are then used to correct the recorded AE energy and estimate the energy released at the crack location.

2. Can a part of AE signal be separated from the total AE data to relate to the AE energy release due to cracking only in the concrete?
   - AE activities recorded during the experiment can result from various sources which can be either tension or friction-related. Using the source classification algorithms, the AE events related to tension and friction are separated, thus the AE energy released due to tension only can be obtained. In addition to this, a comparison between the signal-based classification algorithm and parameter-based classification algorithms is also made.

3. Is the energy released due to cracking as estimated from the AE signal waveform comparable with the energy obtained from the finite element model?
   - In the last part, the estimated AE energy is compared to the locally dissipated energy in the numerical model. To answer this, a methodology is proposed to estimate the locally dissipated energy in the numerical model based on the stresses and strains obtained at the integration points. The methodology is tested on a simple notched beam model and then implemented on the main beam. A conclusion is then made regarding the relationship between locally released energy estimated using AE and the numerical model.

1.4 Outline of the Thesis

Chapter 1: Gives a brief introduction to the topic research. Structural Health Monitoring and Acoustic Emission (AE) is introduced briefly and the motivation to study AE energy is provided. The chapter also provides the research questions and defines the scope of the study.

Chapter 2: Provides the background to AE study in general and AE energy in detail. A literature review exploring the studies relating AE energy to fracture energy, source localization, source classification methods and attenuation in conducted.

Chapter 3: Discusses the methodology to estimate the local energy release in the numerical model. A methodology based on stress-strain is introduced and validation of the methodology is made using a notched beam model.

Chapter 4: Experiments conducted on the Helperzoom girders are discussed. Details regarding the AE acquisition setup are provided with sensor plans and loading schemes.

Chapter 5: Results from Helperzoom models are discussed concerning the crack propagation and released AE energy. Initial AE clustering results and source localization results are provided.

Chapter 6: AE source classification methods used in this thesis are discussed for parameter-based classification and signal-based classification. Source classification results from signal-based clustering are compared with the parameter-based clustering results.

Chapter 7: Discusses attenuation in AE energy due to wave propagation and AE attenuation through cracks using Auto Sensor Tests.

Chapter 8: Numerical techniques used to model the Helperzoom beams are discussed along with the analysis methods. Some preliminary results from the numerical models are also discussed in this chapter.

Chapter 9: Released energy from Helperzoom numerical models are compared with energy detected using AE sensors.

Chapter 10: Key conclusions related to this research are outlined and recommendations are made for future studies.

2 Background and Literature

2.1 AE Monitoring Approach

The process of recording and analyzing an AE signal can be performed using two approaches. They are the parameter-based approach and the signal-based approach [14].

Figure 2.1 shows an AE signal along with some of its associated parameters. In the parameter-based approach for AE monitoring, the recorded waveform is reduced to a set of parameters. The characteristics of these AE parameters are studied to infer physical phenomenon. Some of the conventional AE parameters that have been used by the researchers are- AE hit, count, amplitude, duration, rise time and energy. In addition to these conventional parameters, parameters like average frequency (AF) and RA value are also used. These parameters are derived from the conventional AE parameters. The parameter-based approach is economical and is associated with high data storage and processing speed. Conversely, reducing the whole waveform to a limited set of parameters has significant limitation and can in some cases be misleading [11].

where,

$$RA value = Rise Time / Peak Amplitude$$

$$AF = Count / Duration$$

In the signal-based approach to monitoring, the whole AE waveform as shown in Figure 2.1 is recorded and stored. This approach allows removing signals which have a poor signal to noise ratio as the signal is available for post-processing. The process, in this case, is time-consuming and requires more computational power but provides more accurate results.

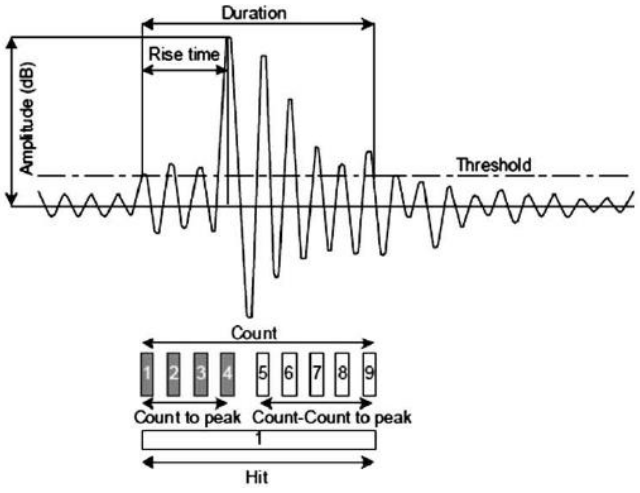

Figure 2.1: Typical AE signal [14]

2.2 AE Energy

In response to the local material changes, AE activities are generated which results in the release of elastic energy. The energy contained by the AE signal can be linked to this released energy [29]. The energy of the AE signal is proportional to the square of the voltage (*V(t)*) and is obtained by squaring and integrating the voltage transients over time [34]:

$$AE\ Energy = \int_{t_o}^{t_e} V(t)^2\, dt \qquad (1)$$

When compared to traditional AE parameters like AE amplitude, count and duration, AE energy provides a better account of failure and is less affected by the threshold criteria. Study relating the bulk fracture energy with the energy released at the microstructure level using AE has been performed in [28], [29], [33]. AE energy has been used in the past to study the severity of the damage, determination of fracture process zone and developing laboratory tools for estimation of fracture energy of concrete.

Landis and Baillon [28] made the first attempt to link AE energy to fracture energy. A series of mortar and concrete beam specimen were tested to estimate the concrete fracture energy while simultaneously monitoring the energy release through AE. Figure 2.2 shows a comparison between the released AE energy and fracture energy. It is observed that for large aggregate specimen the scatter in AE energy is very high. The material scatter increases with the heterogeneity of the specimen, as the signal attenuation becomes more prominent. A good correlation has been reported between the AE energy and fracture energy for fine-aggregate specimen, but a relatively poor correlation is observed for coarse-aggregate specimens. Concrete toughening mechanisms such as friction are held accountable for the poor correlation in the case of a coarse-grained specimen.

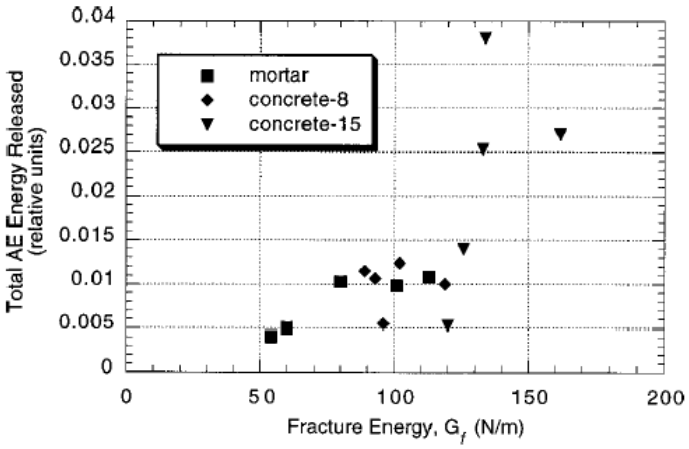

Figure 2.2: AE Energy vs Fracture Energy [28]

Sagar and Prasad [29][33] tested 3 notched beam specimens under three-point bending and observed that the AE energy can be related to the fracture energy as per RILEM draft recommendation [35]. The three beams tested had a different notch to depth ratio. Based on the results a linear relationship could be established between the fracture energy and AE energy.

Additionally, the concept of local fracture energy and boundary effect was used to estimate the size-independent fracture energy.

Otsuka et al [36] and Muralidhara et al [30] used the released AE energy during the experiment to decide the fracture process zone and estimate size-independent (true) fracture energy. Notched beam specimen designed as per the RILEM recommendations were tested. The fracture process zone was termed as the zone in which 75% to 80% of the AE energy was released. The released AE energy was thus used to calculate the transition length and then determine size-independent fracture energy. Figure 2.3 shows the combined load-time and cumulative energy-time plot. The steep rises in the cumulative AE energy plot represent the creation of the macro crack and the flatter portions correspond to crack propagation.

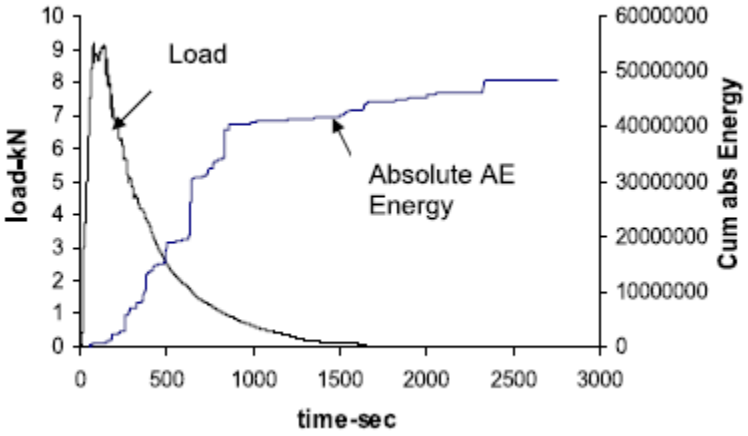

Figure 2.3: Load-time-cumulative AE energy plot [30]

Lu and Li [31] studied the relationship between AE energy and fracture energy in concrete under uniaxial compression and a linear relation was observed between the two during the stable crack development stage. Embedded cement-based piezoelectric sensors were used. AE signal modes related to P- and S-wave component were separated, and they were found to have a linear relationship individually.

Based on the existing literature the relationship between the concrete fracture energy and AE energy has been very well established on the laboratory size specimen on a global scale. The results have been obtained under laboratory conditions and can only be used to develop a laboratory tool [33]. For AE energy-based method to work as a field technique a relationship must be established for real-life size specimens and crack energy needs to be monitored on a local scale.

2.3 AE Source Localization

One of the starting points in crack monitoring using AE is source localization. It refers to estimating the location of the source of the AE activity, irrespective of the nature of the source. A review of the existing source localization methods is given in [16] for both isotropic and anisotropic cases. Tobias [37] carried out early works in the case of the source localization in an isotropic media. Sachse and Sancar [38] conducted similar research for anisotropic media. Source localization-based algorithms for the isotropic and homogenous medium are usually based on

triangulation techniques. The technique assumes a uniform wave speed in the medium and works based on the difference in arrival times of the AE waves at different sensor locations.

A grid search method based source localization algorithm is discussed in [39]. The method uses an arrival-time based algorithm which demands the knowledge of wave velocity in advance. The source localization methodology works under an assumption of homogenous and isotropic media, thus allowing the waves to travel in a straight path with constant velocity. For a two-dimensional localization problem, a minimum of three sensors are needed.

The part of the specimen under consideration is first divided into grids. The best-fitted grid point is then picked by minimizing the following expression:

$$r(z_G) = \sum_{i=1}^{N-1} \sum_{j=i+1}^{N} \left(\left\| z_G - z_{S,i} \right\| - \left\| z_G - z_{S,j} \right\| - c \cdot (t_i - t_j) \right)^2 \tag{2}$$

where z_G represents the grid point, z_S is the sensor location, c is the wave velocity and N is the number of sensors in the experiment setup.

The accuracy of source localization depends on the grid size. Figure 2.4 shows an example of the applied source localization algorithm for a grid size of 0.15 m and the matched grid point is picked as S_o^*. The red line indicates the localization solution resulting from sensor pairing 1 and 2, the blue line denotes the result from sensor pairing 1 and 3, and the green line indicates the result from sensor pairing 2 and 3. The best-fitted grid location S_o^* is then picked using Eqn (2).

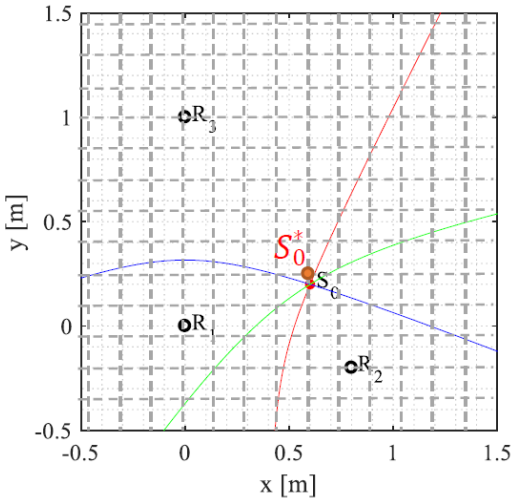

Figure 2.4: Grid Search Method [39]

2.4 AE Source Classification

Within a material, there is a multitude of sources of AE which results in the release of AE stress waves of different characteristics [10][20]. The type of stress wave released depends upon the source of the crack, which can be tensile cracking or friction between existing cracks. Signals from different sources, like tensile cracking and friction, have different features. At tensile cracking, most of the energy is released in the shape of longitudinal waves while friction emits the energy

mostly in the form of S-waves [23]. AE Clustering is the process of forming groups which contain the AE activity released through a similar mechanism.

AE clustering helps in identifying fracture and failure mechanism. Yuyama et al [25] showed that in RC flexure members tensile cracks dominate in the early stages of loading and in later stages of loading the shear cracks dominate. Ohno and Ohtsu [18] used two AE classification methods to investigate the change from tension to shear crack at failure. One of the methods was parameter-based approach involving RA value and Average Frequency (AF) and the other was simplified Green's function for moment tensor analysis (SiGMA) for signal-based classification. Farhidzedah et al [19] introduced a novel approach involving Gaussian Mixture Modeling (GMM) to cluster tension and shear modes of cracking. Van Steen et al [15] proposed a signal-based clustering algorithm based on a virtual distance measure. The proposed algorithm was used to separate different damage sources in the corrosion of RC prisms [20].

2.4.1 Parameter-based Classification

Several parameter-based classification techniques have been successfully implemented in the field of AE, varying from univariate to multivariate analysis methods [27]. The univariate methodology is based on Gutenberg and Richter law [40] from seismology. Shiotani et al [26] and Kurtz et al [41] used AE amplitude to perform b-value analysis in concrete structures to identify damage severity during loading. Other univariate analysis procedures like Z, Ib and RA values have also been used to identify damage [27].

Japan Construction Material Standards (JCMS) [42] recommends a bi-variate parameter-based classification approach which is widely used to differentiate tension cracks from shear cracks [18][19][23][22]. This approach suggests that AE waves generated due to tension cracks have higher AF and lower RA value, and those due to shear crack have lower AF and higher RA (See Figure 2.5). As AE events are random in nature, probabilistic methods are often used to classify the types of cracks. Farhidzadeh et al [19] used Gaussian Mixture Modelling (GMM) to classify the AE parameter set into two clusters. Vidyasagar [43] used GMM besides Support Vector Machine (SVM) to separate the AE clusters using a hyperplane.

Reducing the whole AE waveform to one or two variables can result in loss of information, thus multiple AE parameters are often used for AE classification. Researchers [21][44] have used Principal Component Analysis (PCA) to reduce an n-dimensional space to a reduced p-dimensional PCA space. To deal with a dataset with high order dimensionality (dimension > 2), principal component analysis (PCA) is used. Principal components (PCs) are calculated using Singular Value Decomposition (SVD) methodology as explained in [21]. The AE parameters used were peak AE amplitude, count, rise time and duration of signal. The dimension of the dataset is then reduced to 2 by finding a PCA space representing the direction of maximum covariance.

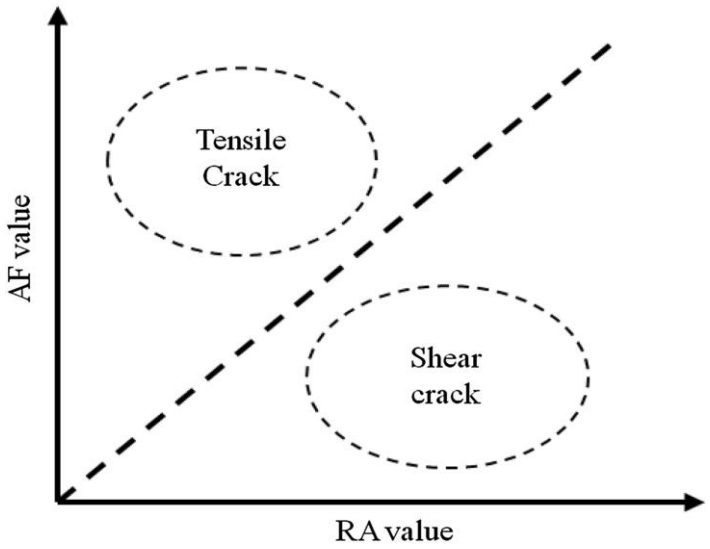

Figure 2.5: JCMS recommendation for crack classification [19]

2.4.2 Signal-Based Classification

Van Steen et al [15] proposed an AE signal-based algorithm used to perform AE source classification. The normalized cross-correlation function is used as a distance parameter to cluster similar waveforms together. Following steps are followed to perform AE clustering, assuming two clusters (Cluster 1 and Cluster 2) initially of lengths m and n:

i. For each signal present in Cluster 1, the cross-correlation coefficient (cc) was determined for every signal present in Cluster 2. Covariance between the time signals is calculated at a certain time lag. The highest value of this covariance matrix is the cross-correlation coefficient between the two signals.

$$cc = \frac{n\sum x_i y_i - \sum x_i \sum y_i}{\sqrt{n\sum x_i^2 - \left(\sum x_i\right)^2}\sqrt{n\sum y_i^2 - \left(\sum y_i\right)^2}}$$

where x and y represent two signals of length n.

ii. Dissimilarity coefficient (d) was calculated for each pair of signals in part (i). Where 'd' is simply defined as, 1 – cc. A total of 'm x n' combinations are obtained for the two clusters.

iii. Cophenetic distance (or inter-cluster distance) is defined as the average of all (m x n) dissimilarity coefficients. If this distance is less than a pre-defined maximum cophenetic distance (d_o), the two clusters are combined.

Following the above methodology, the AE signals can be clustered. Initially, all the AE signals are allotted different cluster number, then two clusters with maximum cophenetic distance are combined at the end of every step. This process is repeated until the step when the cophenetic distance between any two clusters is less than d_o.

2.5 Wave Attenuation in Concrete

Concrete is a heterogeneous material consisting of aggregates, cement particle, voids, microcracks, amongst other things. The microstructural construct of concrete impacts attenuation of AE waves [45]. Ultrasonic AE waves attenuate following two basic mechanisms: (a) Geometric Attenuation; (b) Material Attenuation.

Geometric Attenuation refers to decrease in wave amplitude as the wavefront spreads over a larger area. This is not a true loss of energy but only spreading of the energy which results in a decrease of amplitude as the wave moves away from the source. The rate of geometric attenuation depends on the type of wavefront generated. For body waves spreading with the hemispherical wavefront, the amplitude is proportional to the square root of energy and inversely proportional to distance ($A \alpha 1/r$). But along the surface, the amplitude of the body wave is proportional to the square of distance [46]. For surface waves, which spreads out in the form of a cylindrical wavefront, the amplitude is inversely proportional to the square root of the radial distance [47]. Mathematically the expression for amplitude loss due to geometrical spreading is given by the equation:

$$A_2 = A_1 \left[\frac{r_1}{r_2} \right]^n \tag{3}$$

where A_1 is the amplitude at r_1 distance and A_2 is the amplitude at r_2 distance from the source. 'n' is the factor which represents geometrical attenuation and its value depends on the shape of the wavefront, source location and type of wave. n=1 for body wave, n=0.5 for surface wave.

Material attenuation is the real loss of energy that occurs within the material in the form of absorption (intrinsic attenuation) or scattering (extrinsic attenuation). Absorption loss is the result of an exchange between potential and kinetic energy during wave propagation. Energy loss occurs due to shear heating at grain boundaries. Scattering loss occurs due to scattering of the energy of a wavefield due to material changes or heterogeneity inside the concrete. Mathematical expression accounting for both geometrical and material attenuation for a Rayleigh wave is given by the equation:

$$A_2 = A_1 \left[\frac{r_1}{r_2} \right]^{0.5} e^{-\alpha(r_2 - r_1)} \tag{4}$$

where α is the material attenuation factor which considers material absorption as well as scattering. In addition to geometrical and material-based attenuation, some other factors affect the attenuation during an experimental measurement. Coupling sensitivity between the sensor and the specimen can affect the attenuation measurements considerably, leading to losses even greater than attenuation itself.

In the case of cracked concrete, the AE waves may pass through a crack based on the status of the crack. The crack can be a partially closed one or a fully-open crack [39]. AE waves cannot travel through a fully open crack, thus energy transmission through an open crack can be taken to be zero. For a partially closed crack, a fraction of AE energy can pass through the crack. Zhang [39] reported an attenuation from 14 dB to 46 dB for surface crack opening from 0.05 mm to 3 mm.

The attenuation of AE signals through the crack was observed to be anisotropic. Figure 2.6 shows the amplitude drop caused for different crack widths at different angles.

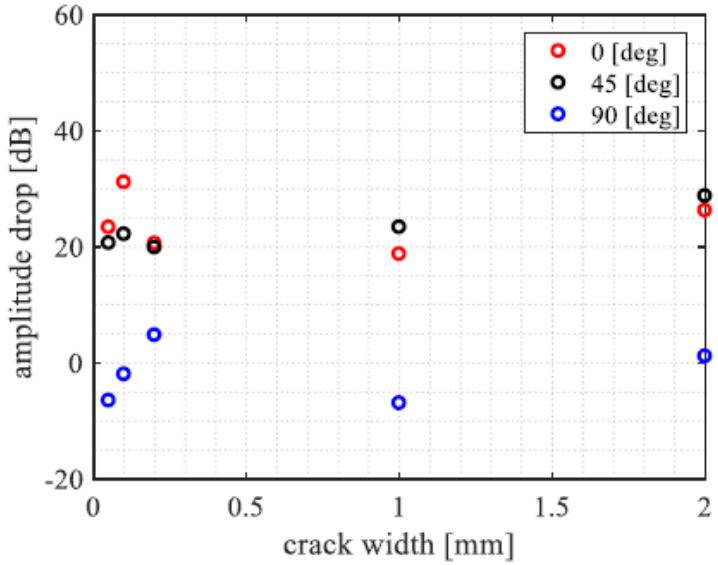

Figure 2.6: Amplitude drop for different crack widths in different directions [39]

3 Methodology for Local Numerical Energy Release

In this chapter following a rotating crack approach for crack modelling, a methodology is proposed to estimate the energy released locally at the integration point in the finite element models. The proposed methodology is then verified using two test models.

3.1 Determination of Dissipated Energy

In the numerical model, the energy released locally due to cracking can be calculated in the form of energy released at the integration points in each element. Firstly, strain energy per unit volume is calculated. Assuming a change in stress from $\sigma_{1,i}$ to $\sigma_{1,i+1}$ and change in strain from $\varepsilon_{1,i}$ to $\varepsilon_{1,i+1}$, the change in strain energy per unit volume is given by Eqn (5).

$$\Delta U_{strain} = 0.5 \cdot (\sigma_{1,i+1} + \sigma_{1,i}) \cdot (\varepsilon_{1,i+1} - \varepsilon_{1,i}) \tag{5}$$

where, σ_1 is the principal stress and ε_1 is the principal strain, and the subscripts *i* and *i+1* represent different load-levels. Using strain energy per unit volume, the change in energy stored at the integration point (ΔU_{intpt}) is given using Eqn (6). ΔU_{intpt} is the amount of energy stored at the integration point when the applied load changes from level *i* to *i+1*. To calculate the total energy stored at an integration point this value is to be summed over all the load increments as shown in Eqn (7).

$$\Delta U_{intpt} = \Delta U_{strain} \cdot (crack\ bandwidth) \cdot (thickness) \cdot (length\ of\ the\ crack) \tag{6}$$

$$U_{intpt} = \sum_{i} \Delta U_{intpt} \tag{7}$$

The energy thus calculated represents the total energy stored at the integration point. This energy includes a recoverable part (elastic energy) and a non-recoverable part (dissipated energy). To calculate the energy dissipated due to the formation of the crack, elastic part of the energy is removed following the secant unloading path. The net dissipated energy at an integration point is calculated using Eqn (8). Index j represents the integration point under consideration. At element level, the dissipated energy is summed up over all the integration points. Thus, total energy dissipated at the element level is given by Eqn (9), where 'm' represents the number of integration points per element.

$$(U_{diss,intpt})_j = U_{intpt} - U_{elastic} \tag{8}$$

$$U_{diss,intpt} = \sum_{j=1}^{m} (U_{diss,intpt})_j \tag{9}$$

In Eqn (6) the thickness of the element is known beforehand; crack bandwidth is obtained as an output from the FEA program and strain energy per unit volume is obtained from stress-strain data using Eqn (5). Length of the crack, on the other hand, is not known in advance. In this study, rotating crack-based material model offered by Diana 10.3 [48] is used, thus the length of the crack is taken in the direction perpendicular to the direction of higher principle stress. Figure 3.1 shows the CQ16M element type used in the analysis. Figure 3.2 shows the same 8-noded element

as it is used in the Diana model. The dimension of the element is 12.5 mm x 12.5 mm. In Figure 3.2, the whole element is divided into 4 parts, where each sub-part represents the area assumed to be covered by one integration point. A randomly directed principal strain is shown in the figure, assuming $\varepsilon 1$ as the higher principal strain. The line perpendicular to this principal strain can be taken as the length of the crack at the given integration point. The length of the crack can be calculated at the integration point level or the element level. Both possibilities for crack length estimation are discussed in the next section.

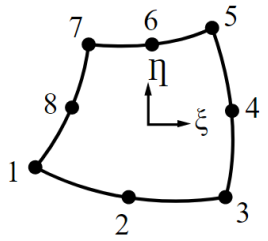

Figure 3.1: Element CQ16M

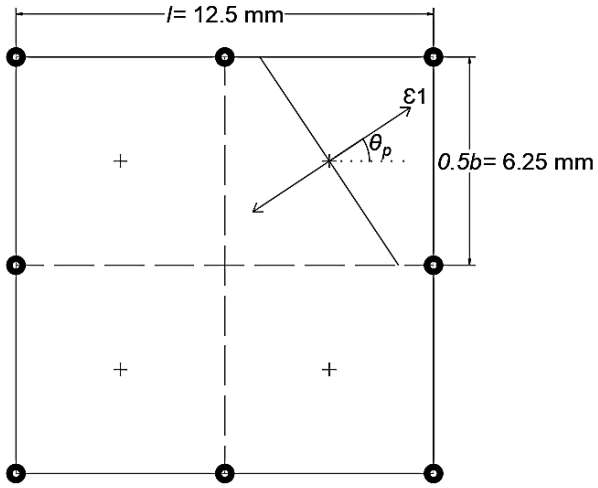

Figure 3.2: Length of crack per integration point

Principal direction angle (θ_p) is calculated using the local strains in x and y direction, Eqn (10).

$$\theta_p = \arctan\left(\frac{\varepsilon_{xy}}{(\varepsilon_{xx} - \varepsilon_{yy})}\right) \cdot 0.5 \tag{10}$$

where ε_{xx} is the strain in local x-direction, ε_{yy} is the strain in the local y-direction and ε_{xy} is the shear strain in the local coordinate system.

The principal stress (σ_1 and σ_2) and principal strain (ε_1 and ε_2) are obtained by rotating the local stress by the principal angle calculated in Eqn (10). The length of the crack is calculated in

the direction perpendicular to the maximum between ε_1 and ε_2. The energy dissipated is calculated in only one direction; the one with the higher principal strain.

$$\sigma_1 = \sigma_{xx} \cdot \cos^2(\theta_p) + \sigma_{yy} \cdot \sin^2(\theta_p) + 2\sigma_{xy} \cdot \cos(\theta_p) \cdot \sin(\theta_p)$$
$$\sigma_2 = \sigma_{xx} \cdot \sin^2(\theta_p) + \sigma_{yy} \cdot \cos^2(\theta_p) - 2\sigma_{xy} \cdot \cos(\theta_p) \cdot \sin(\theta_p) \quad (11)$$

$$\varepsilon_1 = \varepsilon_{xx} \cdot \cos^2(\theta_p) + \varepsilon_{yy} \cdot \sin^2(\theta_p) + \varepsilon_{xy} \cdot \cos(\theta_p) \cdot \sin(\theta_p)$$
$$\varepsilon_2 = \varepsilon_{xx} \cdot \sin^2(\theta_p) + \varepsilon_{yy} \cdot \cos^2(\theta_p) - \varepsilon_{xy} \cdot \cos(\theta_p) \cdot \sin(\theta_p) \quad (12)$$

To calibrate the estimated locally dissipated energy, we compare the summation of the energy dissipated locally with the energy dissipated at the global (specimen) level. The area under the load-displacement curve reflects the amount of energy released at the specimen level. Energy added into the system when applied force increases from F_i to F_{i+1} under a displacement Δx is given as :

$$\Delta U_{specimen} = 0.5 \cdot (F_{i+1} + F_i) \cdot \Delta x \quad (13)$$

The total energy stored under the load-displacement curve is the summation of the energy stored through all the load increments given as:

$$U_{Total,specimen} = \sum_i 0.5 \cdot (F_{i+1} + F_i) \cdot (x_{i+1} - x_i) \quad (14)$$

And the dissipated energy is:

$$U_{diss,specimen} = U_{Total} - U_{Elastic} \quad (15)$$

Where $U_{Elastic}$ refers to the elastic energy stored in the system. As the numerical model uses total strain-based material model, the elastic energy is removed using secant unloading. So, if the final force at the end of loading is F_f and the final displacement is u_f, then the elastic energy stored is given as:

$$U_{Elastic} = 0.5 \cdot F_f \cdot u_f \quad (16)$$

The total dissipated energy at specimen level ($U_{diss,specimen}$ in Eqn (15)) should be equal to the sum of the energy released at integration points ($U_{diss,intpt}$ in Eqn (9)).

3.2 Crack Length Estimation

As discussed earlier, estimation of the length of the crack is a pre-requisite to determining the energy released locally and this can be done at the integration point level or the element level. Both approaches are discussed here.

An element of dimension 100 mm x 100 mm is considered with four integration points, numbered 1 to 4. Assuming that the element is under horizontal tensile stress, Figure 3.3 presents the scenario when the length of the crack is calculated at the integration point level. Cracks are shown

as red zig-zag lines. All four integration points have a crack length of 50 mm. Figure 3.4 shows the scenario when the length of the crack is calculated at the element level. Length of the crack, in this case, is 100 mm. When the crack length is estimated at the integration point the resulting total crack length is twice the expected crack length. To avoid this issue the length of the crack is calculated at the element level. As per this method, for each element, the energy per unit area per load increment is calculated at each integration point using Eqn (17).

$$\Delta U_{intpt} = \Delta U_{strain} \cdot (crack\ bandwidth) \cdot (thickness) \tag{17}$$

where ΔU_{strain} is calculated using Eqn (5).

The principal direction at element level is calculated using Eqn (18). The summation of stresses in the local coordinate system at all the four integration points of the element is used to calculate the representative principal angle. Then, the crack length is calculated using Eqn(19).

$$\theta_{p,element} = \arctan\left(\frac{\sum \varepsilon_{xy}}{(\sum \varepsilon_{xx} - \sum \varepsilon_{yy})}\right) \cdot 0.5 \tag{18}$$

$$length\ of\ \ crack = \begin{Bmatrix} l / \cos(\theta_p); & for\ |\theta_p| < \arctan\left(\frac{b}{l}\right) \\ b / \sin(\theta_p); & for\ |\theta_p| \geq \arctan\left(\frac{b}{l}\right) \end{Bmatrix} \tag{19}$$

where l is the length of the side of the element, b is the height of the element, θ_p is the direction of principal strain.

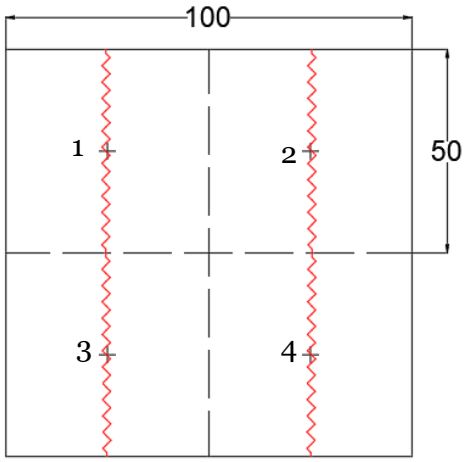

Figure 3.3: Length of Crack at Integration Point Level

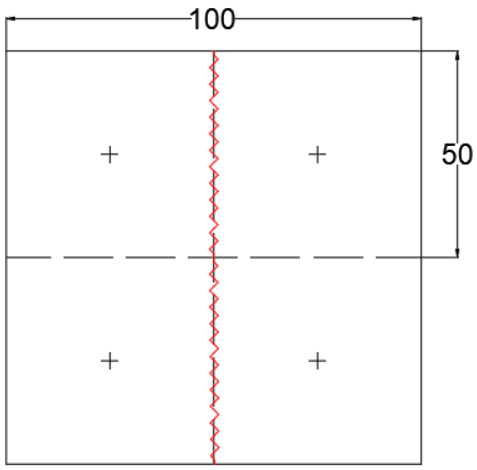

Figure 3.4: Length of Crack at Element Level

Finally, the energy per element per load increment at the element level is determined using Eqn (20). $\sum \Delta U_{intpt}$ is the sum the energy stored per unit area at all the four integration points of the element and number of integration points per element is four in this case. The total energy can be obtained by adding the energy at each load increment, Eqn (21).

$$\Delta U_{element} = \frac{\sum \Delta U_{intpt}}{No.of\ integration\ pts.\ per\ element} \cdot (length\ of\ crack)_{element} \tag{20}$$

$$U_{total} = \sum \Delta U_{element} \tag{21}$$

Total dissipated energy is obtained by removing the elastic energy as per secant unloading.

3.3 Description of Test Finite Element Models

Test Model 1

A 100 mm x 100 mm x 50 mm specimen is modelled as a single element as shown in Figure 3.5. The left edge is restricted in x-direction completely with vertical support only at point A and the right edge is subjected to displacement-controlled load in the positive x-direction. The specified load steps are 10 steps of 0.001 mm and 45 steps of 0.01 mm. The material properties used for this model are presented in Table 3.1. 8-noded quadrilateral plane stress elements (CQ16M) with a regular 2x2 integration scheme are used.

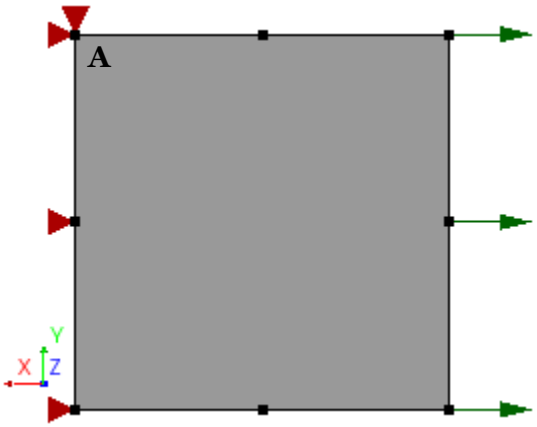

Figure 3.5: Test Model 1

Table 3.1: Material Properties Test Model 1 (Concrete)

Property	Value
Young's Modulus	33550 MPa
Poisson Ratio	0
Mass Density	0
Material Model	Total Strain Based Rotating Crack
Tensile Behavior	Hordijk Curve
Tensile Strength	3.0 MPa
Mode-I Fracture Energy	0.14 N/mm
Crack Bandwidth	Rots
Compressive Behavior	Parabolic Curve
Compressive Strength	38 MPa
Fracture Energy	35 N/mm

Test Model 2

A test concrete notched beam specimen (Figure 3.6) is modelled in DIANA. The beam dimension is 800 mm x 100 mm x 100 mm. The notch is triangular with a width of 5 mm at the bottom and the depth of the notch is 50 mm. The beam is simply supported and loaded under displacement control. Concrete material properties are the same as shown in Table 3.1 with a mass density of 2.4e-9 T/mm^3. 8-noded quadrilateral plane stress elements (CQ16M) with a regular 2x2 integration scheme are used. 75 load steps of 0.03 mm each are applied.

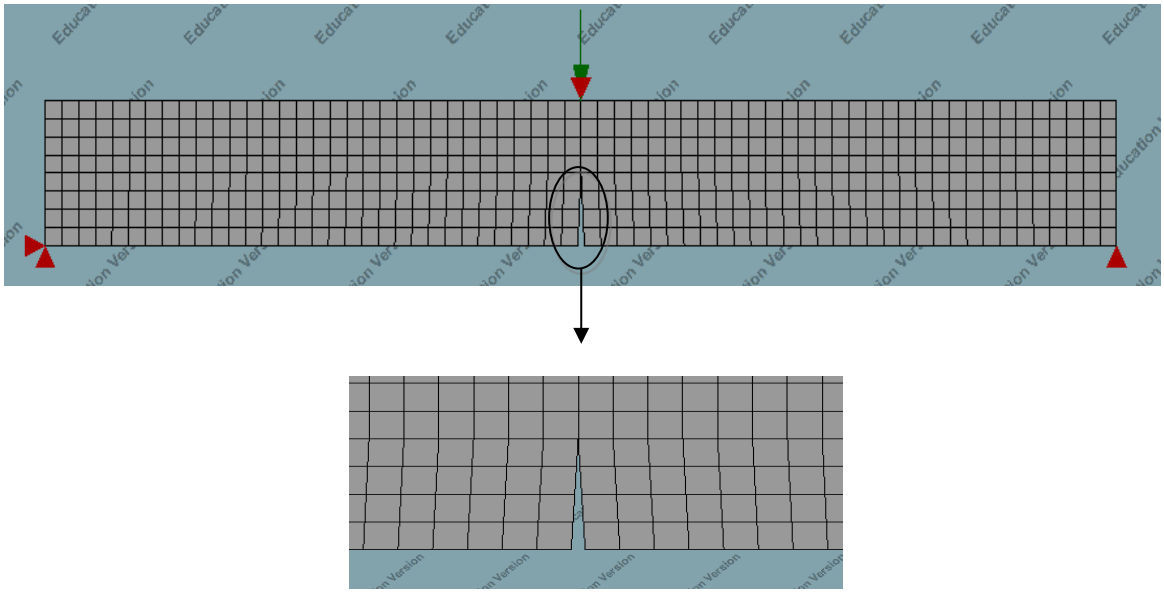

Figure 3.6: Test Model 1 with a triangular notch

3.4 Validation of the methodology using test models

Using the methodology in Section 3.1, the energy released at integration points is calculated. The load-displacement plot for the test model 1 is shown in Figure 3.7, and the stress-strain plot is shown in Figure 3.8. The crack bandwidth is 100 mm and the length of the crack, following the process described in Figure 3.2, is 50 mm. Following the same procedure as in Chapter 3.1, the summation of the released energy at integration points is 703.85 N-mm which is same as the released energy at specimen level. Table 3.2 shows a summary of the result obtained from Test Model 1. Length of the crack is equal to 100 mm which results in the crack area of 5000 mm^2. Based on the energy dissipated under the load-displacement curve, fracture energy of 0.1407 N/mm is obtained. This value is the same as the input value of mode-I fracture energy in Table 3.1.

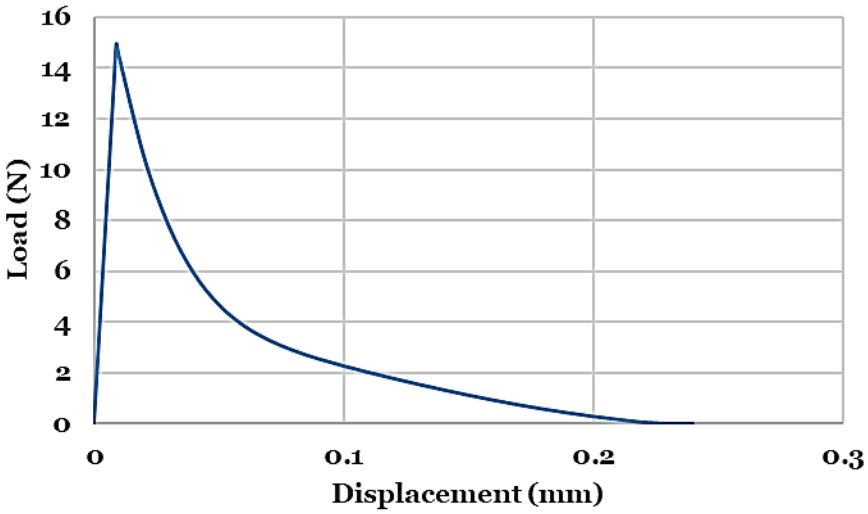

Figure 3.7: Load-Displacement (Test Model 1)

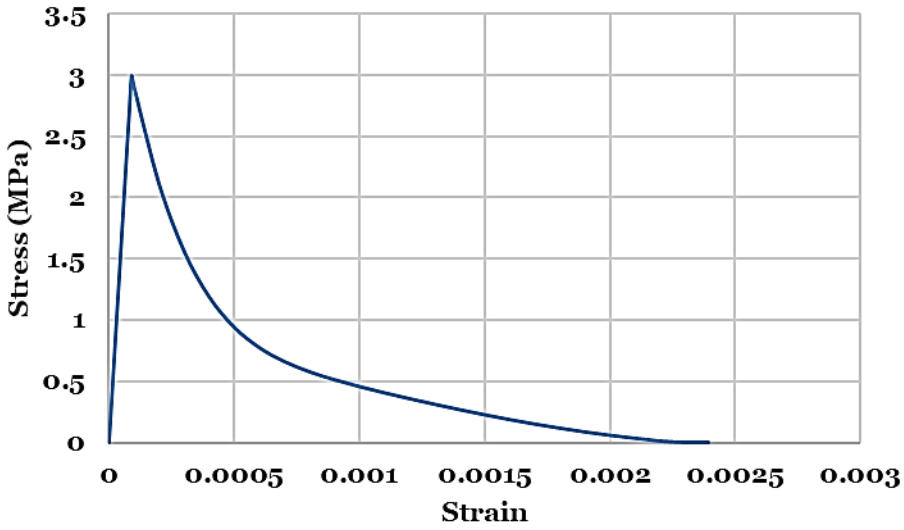

Figure 3.8: Principal Stress (σ_1)-Principal Strain(ε_1) Plot (Test Model 1)

Table 3.2: Test Model 1 Results

Property	Value
Crack Length	100 mm
Thickness	50 mm
Crack Area	5000 mm²
Fracture Energy	0.1407 N/mm
Dissipated Energy	703.85 N-mm

So, for the simple case of one element model, the proposed methodology for crack energy release gives good results. The methodology is also tested for test model 2 which is a notched beam specimen under three-point load. In this calculation, only the cracked elements are considered. Figure 3.9 shows the cracked elements at the end of loading, numbered 1 to 8. Two integration points (from element 6) along the direction of the notch are marked as Point 1 and Point 2. Figure 3.10 and Figure 3.11 show the stress-strain plot at Point 1 and Point 2 respectively. Principal stresses and principal strains calculated as per Eqn (11) and Eqn (12) are used in the stress-strain plots. The area under the curve in Figure 3.10 and Figure 3.11 represents the strain energy per unit volume stored at the integration point. Using Eqn (6), (7) and (8) the energy dissipated at all the cracked integration points is calculated.

Table 3.3 shows the energy dissipated at integration points of all the cracked elements. Initially, the energy dissipated is calculated in both the principal directions, but then the dominant direction is selected and values over it is summed up. Adding the dissipated energies at all the integration points results in a value of 98.7 N-mm.

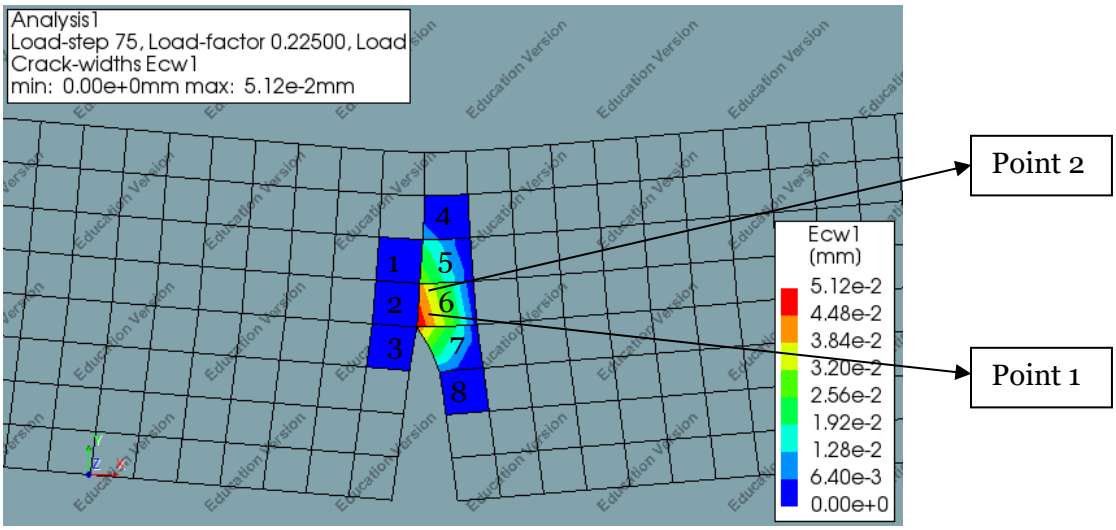

Figure 3.9: Cracked Elements

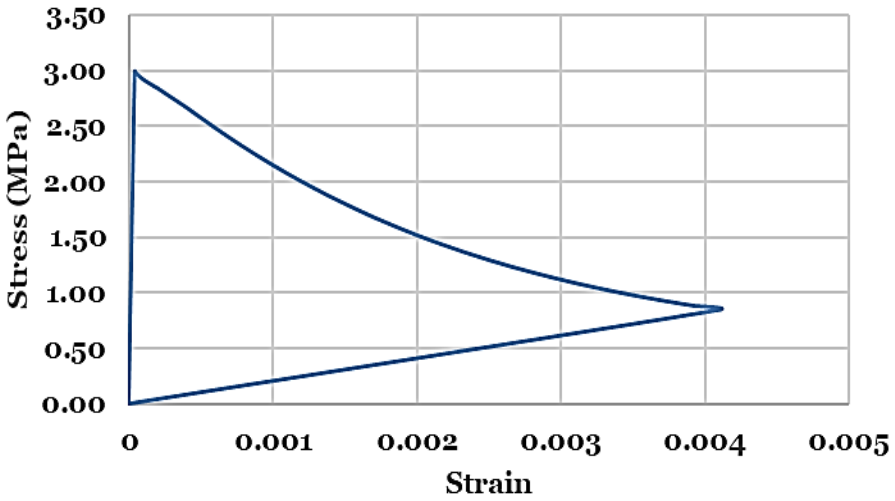

Figure 3.10: Principal Stress (σ_1)-Principal Strain(ε_1) Plot (Point 1)

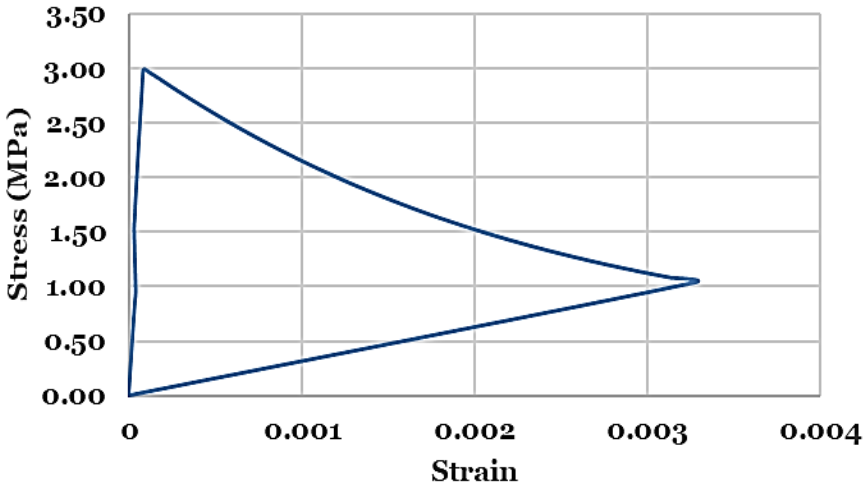

Figure 3.11: Principal Stress (σ_1)-Principal Strain(ε_1) Plot (Point 2)

Table 3.3: Energy Dissipated at Cracked Integration Points

Element	Integration Pt.	Dissipated Energy (N-mm)		Maximum
		Direction 1	Direction 2	
1	1	0.0263	0.501	0.501
	2	0.0793	-0.05	0.0793
	3	0.0138	-0.0582	0.0138
	4	-0.0157	0.118	0.118
2	1	0.0106	2.76	2.76
	2	0.0089	1.2	1.2
	3	0	0.0088	0.0088
	4	0.0002	0.303	0.303
3	1	0	-0.0011	0
	2	0.0006	-0.0006	0.0006
	3	-0.0226	0.0185	0.0185
	4	-0.0001	3.51	3.51
4	1	5.24	0.0372	5.24
	2	0.0046	-0.0007	0.0046
	3	0.402	0.0378	0.402
	4	-0.0385	0.0007	0.0007
5	1	13.8	0.0542	13.8
	2	0.0704	0.0107	0.0704
	3	8.14	0.0398	8.14
	4	0.0176	0.0249	0.0249
6	1	19.4	0.0119	19.4
	2	1.07	0.0004	1.07
	3	16.4	0.0104	16.4
	4	0.0743	0.0003	0.0743
7	1	3.84	0.0016	3.84
	2	0.0563	0.0071	0.0563
	3	21.05	0.0013	21.05
	4	0.0102	0.412	0.412
8	1	-0.0021	0	0
	2	0	-0.01	0
	3	-0.1101	0	0
	4	0.397	0	0.397
Total Dissipated Energy		=		**98.7 N-mm**

The released energy at specimen level was calculated to calibrate the estimated local released energy. The load-displacement plot is shown in Figure 3.12. The unloading path follows the secant unloading as discussed in Section 3.1. The area enclosed by the curve in Figure 3.12 represents the energy dissipated at the specimen level. The dissipated energy ($U_{diss,specimen}$) is equal to 92 N-mm. This value is almost the same as the value from integration points with a dissimilarity of 5 percent. Thus, the methodology for estimation of released crack energy can be used further.

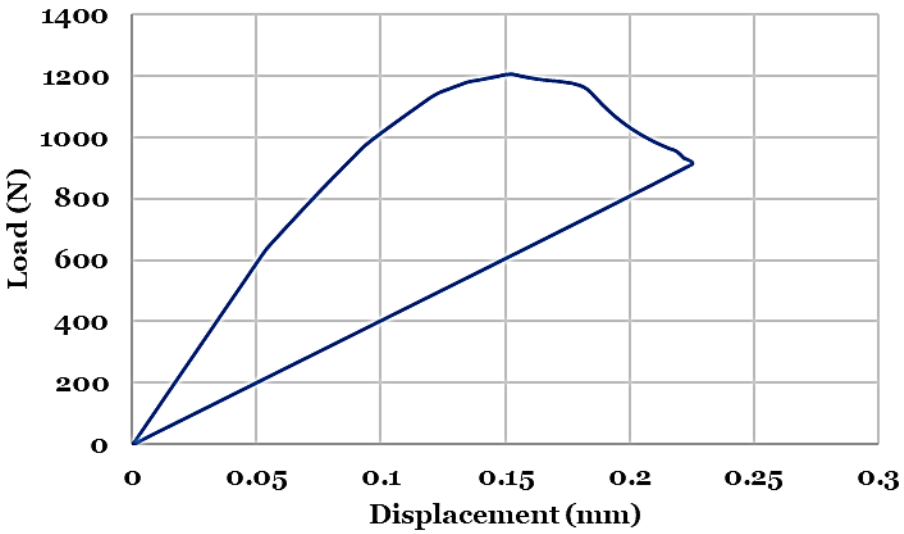

Figure 3.12: Load-Displacement Plot (Test Model 1)

4 Experiments on prestressed concrete girders

Four prestressed concrete girders from the Helperzoom viaduct numbered HPZ01 to HPZ04 were tested to failure. The viaduct is demolished as a part of a development project and the girders are made available for research. The girders are sawn cut and then delivered to the laboratory for testing. The experiments are a part of a larger research project aimed towards investigating the shear capacity of the prestressed concrete girders. The details regarding the experiments can be found in the test measurement report [49] and the analysis report [50]. In this section, the experiment is discussed in brief with only the details that are relevant to this study.

4.1 Beam Geometry

The standard cross-section for the Helperzoom girder is T-shaped, shown in Figure 4.1, along with cross-section reinforcement detail. A side view of the saw cut girder is shown in Figure 4.2, with a detail of the 11.7 m length of the cut girder in Figure 4.3. End block of 800 mm length is present at the end of the beam with the thickness same as the thickness of the bottom flange, i.e., 550 mm. A transition zone of 1000 mm, shown in Figure 4.4, is provided between the end block and the standard cross-section. The beam is post-tensioned using 10 tendons- 7 of these tendons are anchored at the end and 3 of these are anchored at the top flange at a distance of 270 mm, 390 mm and 510 mm from the end (Figure 4.3). Stirrups of diameter 10 mm with the centre to centre spacing of 400 mm are provided across the span of the beam.

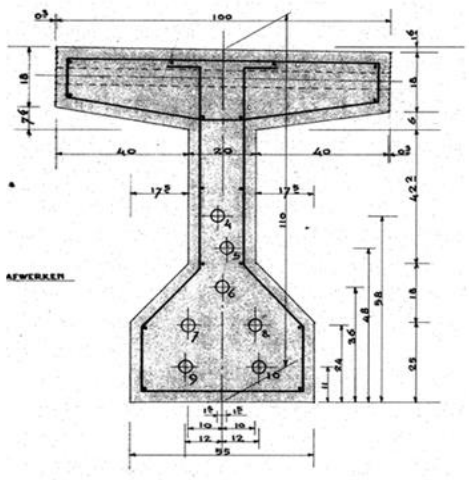

Figure 4.1: Cross-section of the Helperzoom Beam

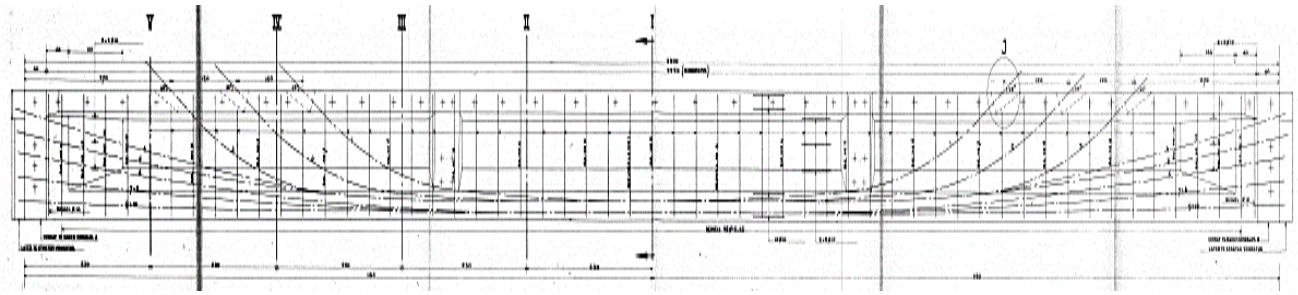

Figure 4.2: Side View of Helperzoom Girder

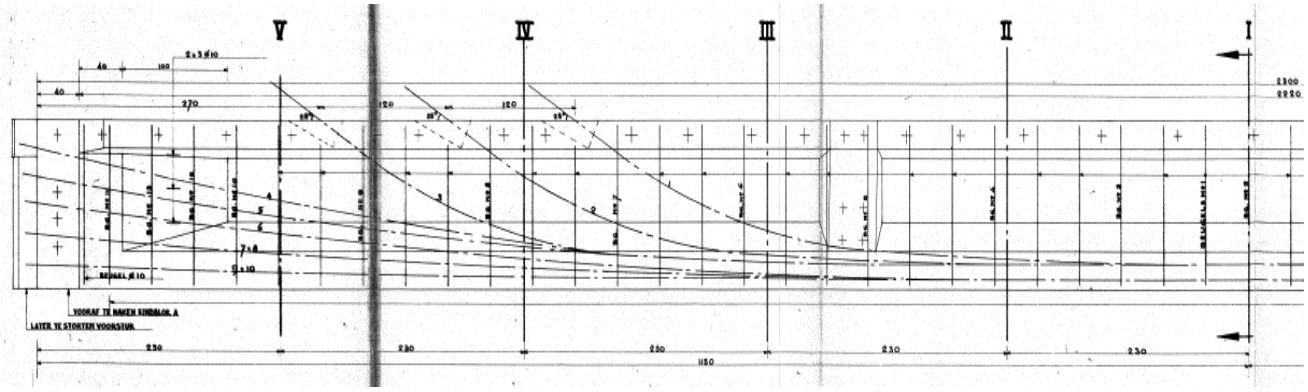

Figure 4.3: Girder Detail

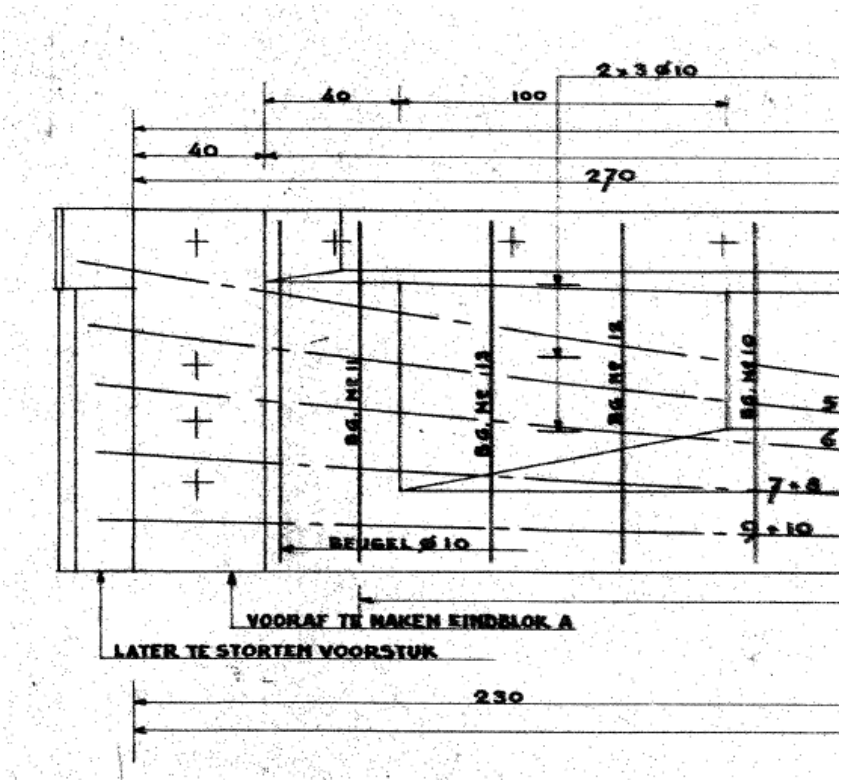

Figure 4.4: End Block and Transition Zone

4.2 Material Description

Cores drilled from the Helperzoom viaduct are used to determine the concrete properties. The average compressive strength is estimated to be 76.3 MPa and the characteristic strength is 62.7 MPa. Average tensile strength of 5.4 MPa is estimated using the splitting tests. The characteristic tensile strength is 4.0 MPa. Twelve samples of prestressing steel were tested in the laboratory. The average ultimate strength of 1824 MPa is obtained at a failure strain of 0.0535 and average stress of 1433 MPa is obtained corresponding to 0.01 strain. Reinforcement is made up of ribbed FeB400 steel. Table 4.1 shows a summary of the material properties. A detailed account of the material study can be found in the measurement report [49].

Table 4.1: Material Description for Helperzoom

Property	Value
Concrete	
Average Compressive Strength	76.3 MPa
Average Tensile Strength	5.4 MPa
Prestressing Steel	
Ultimate Strength	1824 MPa
Ultimate Strain	0.0535
Average Stress at 0.01 strain	1433 MPa
Reinforcement	FeB400

The current prestressing level is determined using sectional analysis. The prestressing level determined for the four beams is shown in Table 4.2. For a detailed investigative report refer analysis report [50].

Table 4.2: Prestressing Level using Sectional Analysis

Beam Number	Prestressing Level (MPa)
HPZ01	695
HPZ02	725
HPZ03	700
HPZ04	780

4.3 Test Set-up

As shown in Table 4.3, the four beams tested are of varying length with the shortest being 10.51 m long. Based on this the span length of 9.6 m is determined for the experiment. The resulting geometry of the beam and the position of the support is shown in Figure 4.5. Side view of the test setup is shown in Figure 4.6 and an overview of the setup is shown in Figure 4.7. The load jack and supports are also shown in Figure 4.7.

The detailed loading setup is shown in Figure 4.8 (a). Under the loading jack, a system of felt and Teflon is used. The dimension of the loading plate is 300 mm x 300 mm. Detail of support condition is shown in Figure 4.8 (b). The dimension of the support plate is 100 mm x 560 mm x 10 mm.

Table 4.3: Beam Dimension

Beam Number	Length (m)
HPZ01	10.51
HPZ02	11.1
HPZ03	12.28
HPZ04	12.88

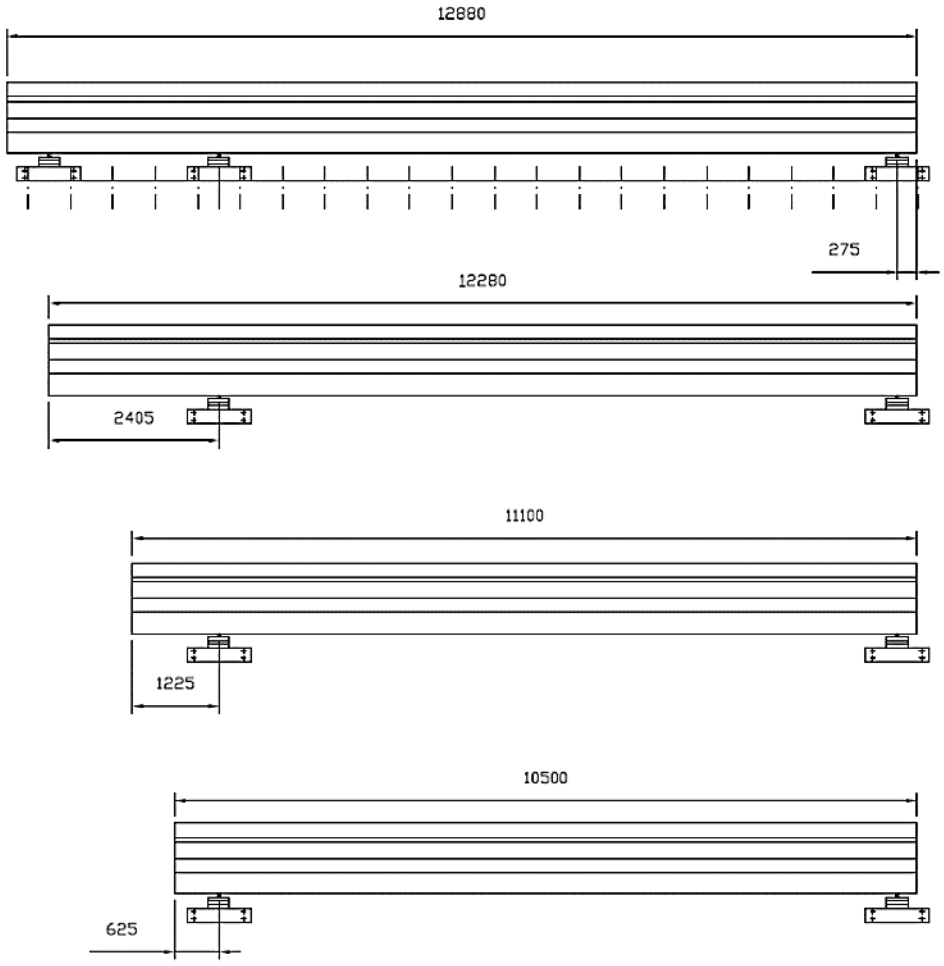

Figure 4.5: Experiment geometry and support position

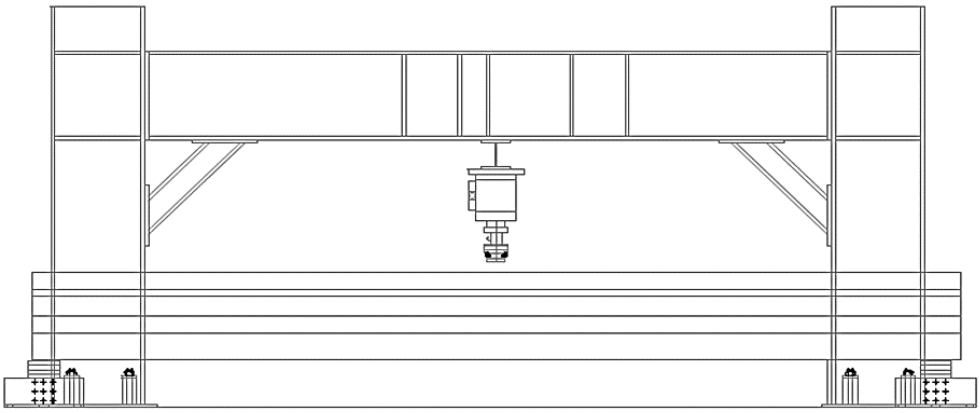

Figure 4.6: Side view of the test setup

Figure 4.7: Test setup overview

(a) Load Detail

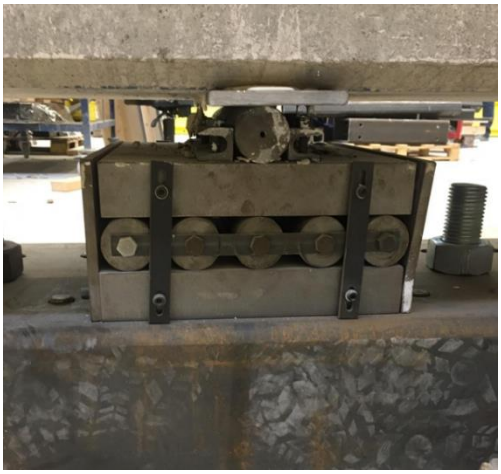

(b) Support Detail

Figure 4.8: Load and Support Detail

4.4 AE Acquisition Setup

The AE system used was a 16-channel (20-channel for HPZ04) MISTRAS system manufactured by Physical Acoustics Corporation (PAC). The AE test setup comprises of AE sensors, processing instrumentation and AE win for SHSM (Sensor Highway II- Smart Monitoring) software. The system is designed for unattended Structural Health Monitoring based application. A threshold of 40 dB was set w.r.t. parameter acquisition and 60 dB w.r.t. signal acquisition. Pre-trigger of 250 µsec is applied.

4.4.1 AE Sensor

Piezoelectric sensors (or transducers) are used to detect the AE stress waves and then convert the stress wave to an electrical signal. Amplifiers are then used to elevate the signal to a functioning level. R6I type resonant type sensors are used in the experiment. The sensors are equipped with an integral preamplifier which provides 40 dB amplitude gain. Figure 4.9 shows a typical R6I resonant type sensor with its sensitivity plot. AE sensor diameter is 29 mm and its height is 40 mm with working temperature range of -45° C to 85° C. The operating frequency range is 40-100 kHz and the resonant frequency is 50 kHz. In the case of HPZ03 and HPZ04 beams, 2 WDI type broadband sensors (Figure 4.10) are also used with a working frequency range from 100-900 kHz.

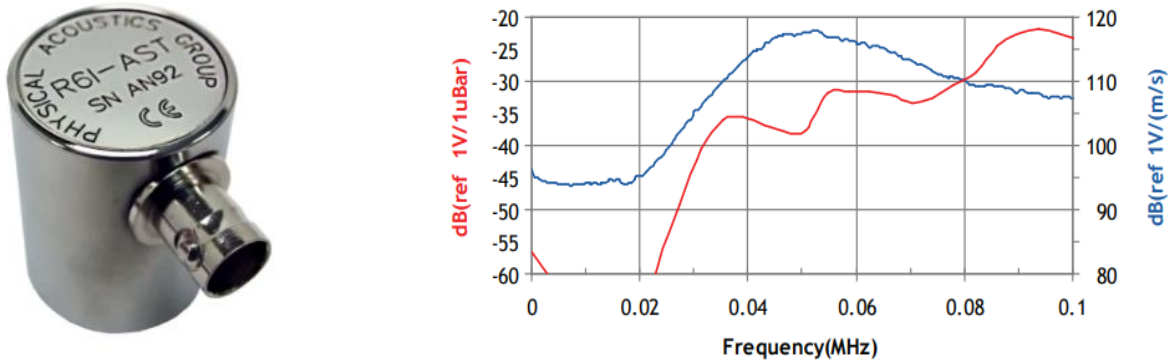

Figure 4.9: R6I- Resonant Sensor with Sensitivity Plot

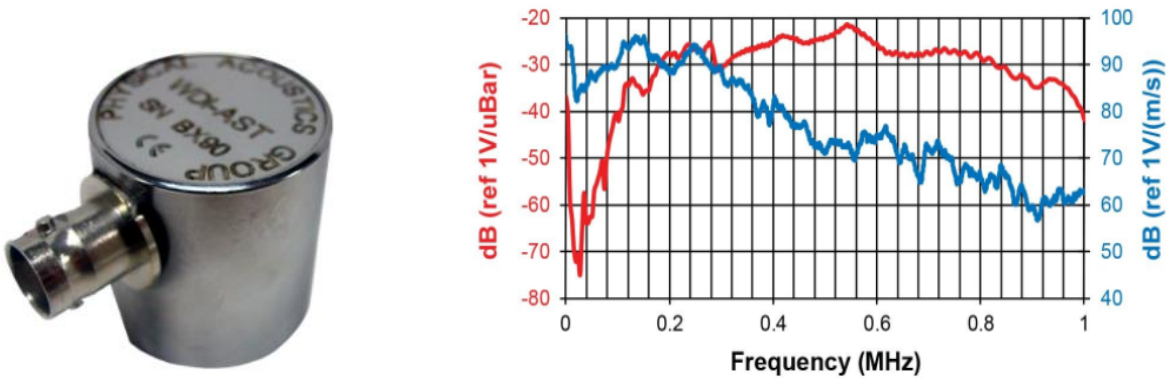

Figure 4.10: WDI- Broadband Sensor with Sensitivity Plot

4.4.2 Sensor Coupling

Adequate acoustic coupling between the sensor and the structure surface is an essential requirement during AE testing. Firstly, the sensor surface is cleaned to get rid of any dust, providing a smooth and clean surface. A thin layer of electrical couplant is then put between the sensor and the beam surface allowing maximum adhesion. Applied couplant layer should be thin so that it can seal the gaps due to surface roughness and remove the air gaps to guarantee good acoustic transmission.

To maintain coupling stability, the sensor must always be stationary. This is ensured by using metal hold-downs. The hold downs are attached to the beam surface using a putty-like adhesive, and the sensors are then held in their place using a screw. A rubber piece is placed between the screw and the sensor to avoid any damage to the sensor. Figure 4.11 shows a sensor mounted on the surface of the beam. Pencil lead break tests are conducted at the start of the experiment to ensure good coupling between the sensor and the surface.

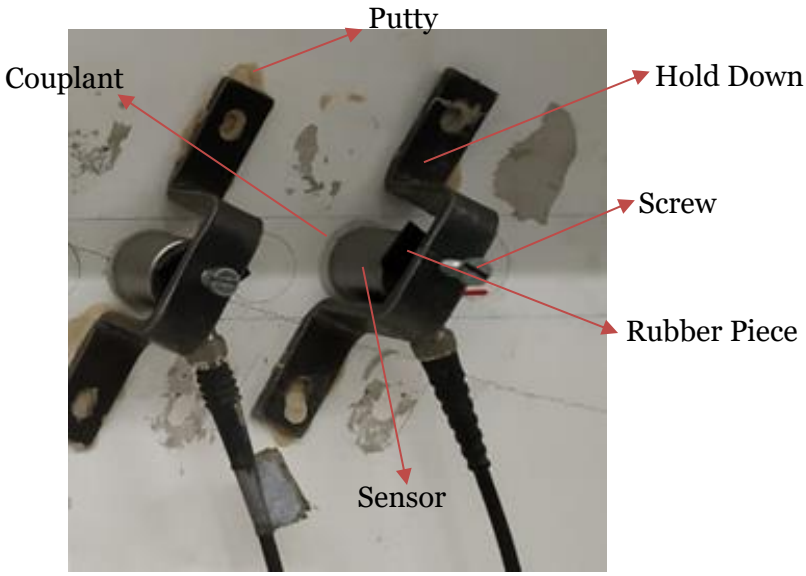

Figure 4.11: Sensor-Beam Surface Coupling

4.4.3 AE Sensor Plan

Sensor plan for all the Helperzoom beams is shown in Figure 4.12-Figure 4.15. A total of 13 AE sensors are used for HPZ01 and HPz02, 15 sensors are used for HPZ03 and 20 sensors are used of HPZ04. The sensors are placed such that the parts of the beam with flexure as well as shear cracks are aptly covered. All the sensors are in one vertical plane, with some placed at the bottom side of the beam and others are placed in the web region.

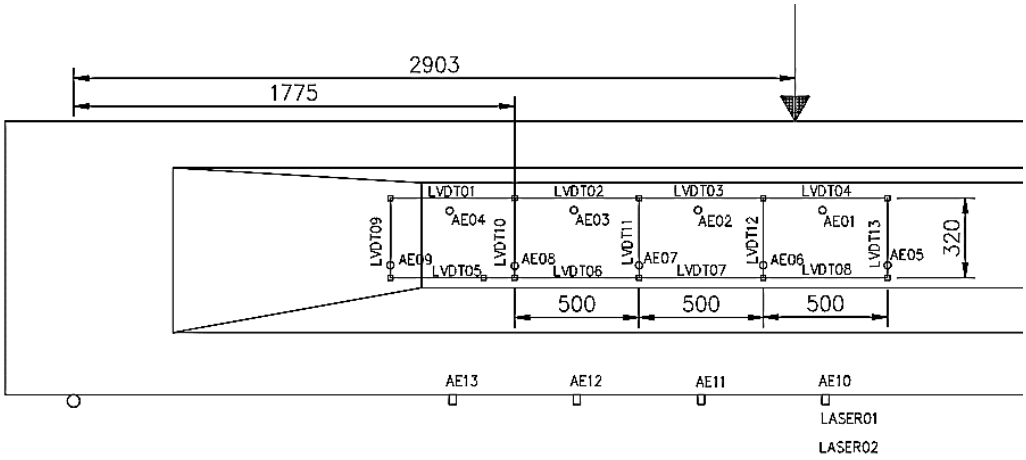

Figure 4.12: Sensor Plan for HPZ01 including LVDT, lasers and AE sensors

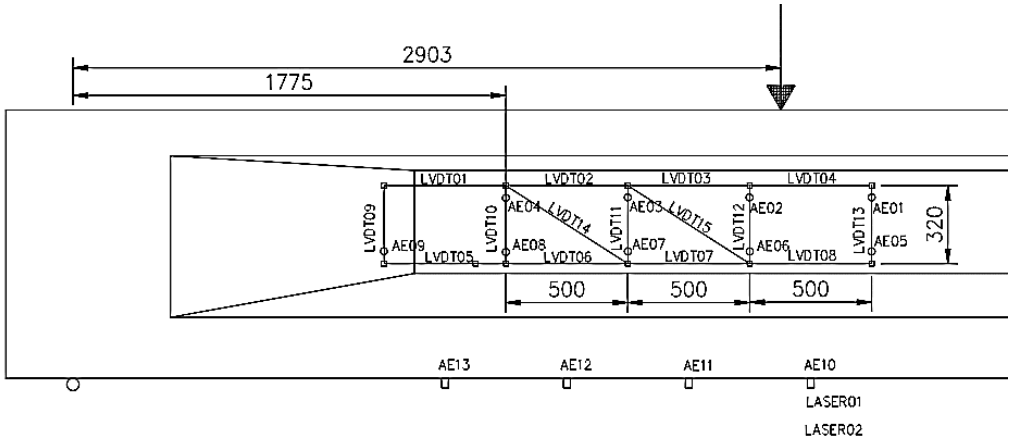

Figure 4.13: Sensor Plan for HPZ02 including LVDT, lasers and AE sensors

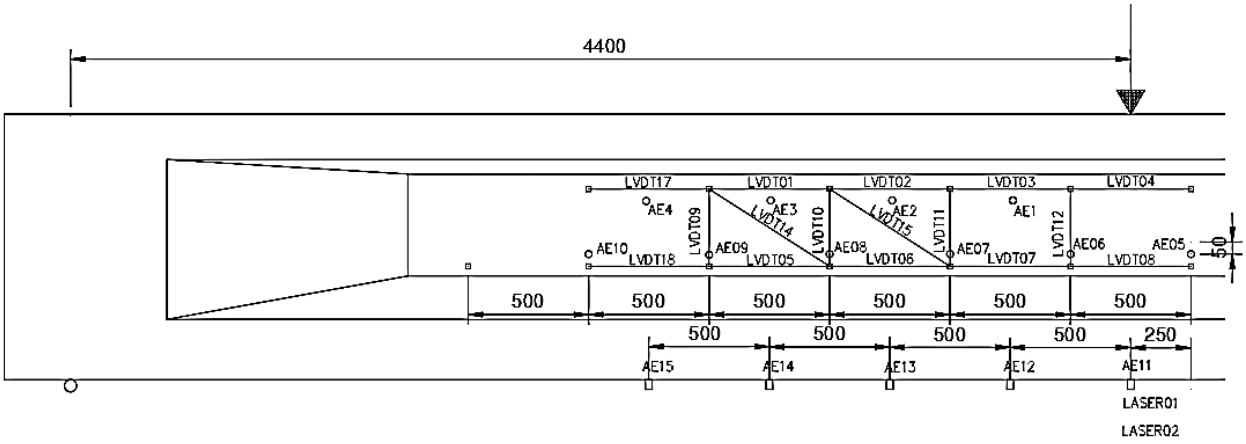

Figure 4.14: Sensor Plan for HPZ03 including LVDT, lasers and AE sensors

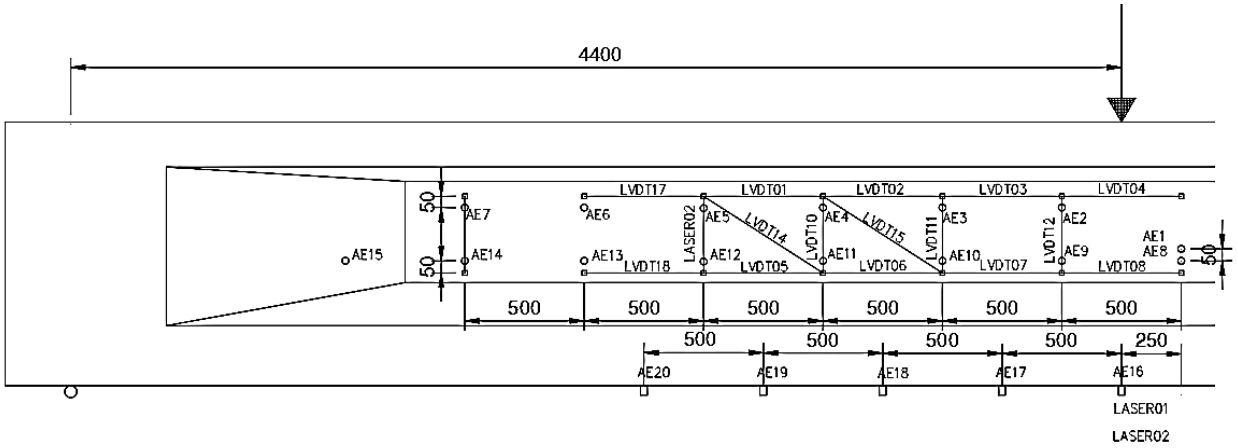

Figure 4.15: Sensor Plan for HPZ04 including LVDT, lasers and AE sensors

4.5 Displacement Measurements

In addition to AE sensors, LVDTs and lasers were also installed to measure displacements. Thirteen LVDTs were used in HPZ01 and HPZ02, while 18 LVDTs were used for HPZ03 and HPZ04. The LVDTs are used to measure the horizontal and vertical displacements in the web of the girder. The position of the LVDTs for all the four beams is shown in Figure 4.12-Figure 4.15. Two laser distance finders are also used to find the deflection under the load.

In addition to LVDT measurement, Digital Image Correlation (DIC) was also implemented. The backside of the beam was painted with black and white paint using a paint roller. The DIC measurements results used in this thesis are directly taken from the measurement report for Helperzoom girder testing [49]. Two high-resolution cameras were used to take the photographs from the backside of the beam along with two studio flashes. Applied layout consisting of LVDTs and AE sensor locations for HPZ01 is shown in Figure 4.16.

Figure 4.16: Applied Sensor Layout for HPZ01

4.6 Loading Scheme

The loading scheme adopted for testing of the Helperzoom beams can be divided into 4 phases. In the first phase, the beam is loaded to a small load-level to ensure that all the systems are in place and working. In the second phase, the beam is loaded until the first flexure crack is obtained, and in phase three, the beam is loaded until the first shear crack is obtained. In the final phase, the beam is loaded until failure. At the end of the first three phases, the beam is unloaded and then reloaded to have three complete cycles. Figure 4.17 and Figure 4.18 show the load-history of HPZz01 and HPZ02, where all the four phases of loading can be identified.

Figure 4.19 shows the load history diagram for HPZ03 and Figure 4.20 shows the load history diagram for HPZ04 along with some of the marked intervals. Interval 1 and 2 in Figure 4.19 indicate the occurrence of the first flexure crack and interval 5 indicates the occurrence of the first shear crack in HPZ03. In Figure 4.20 interval 1 and 2 indicate the occurrence of first flexure crack and interval 3 and 4 indicate the occurrence of the first shear crack in HPZ04.

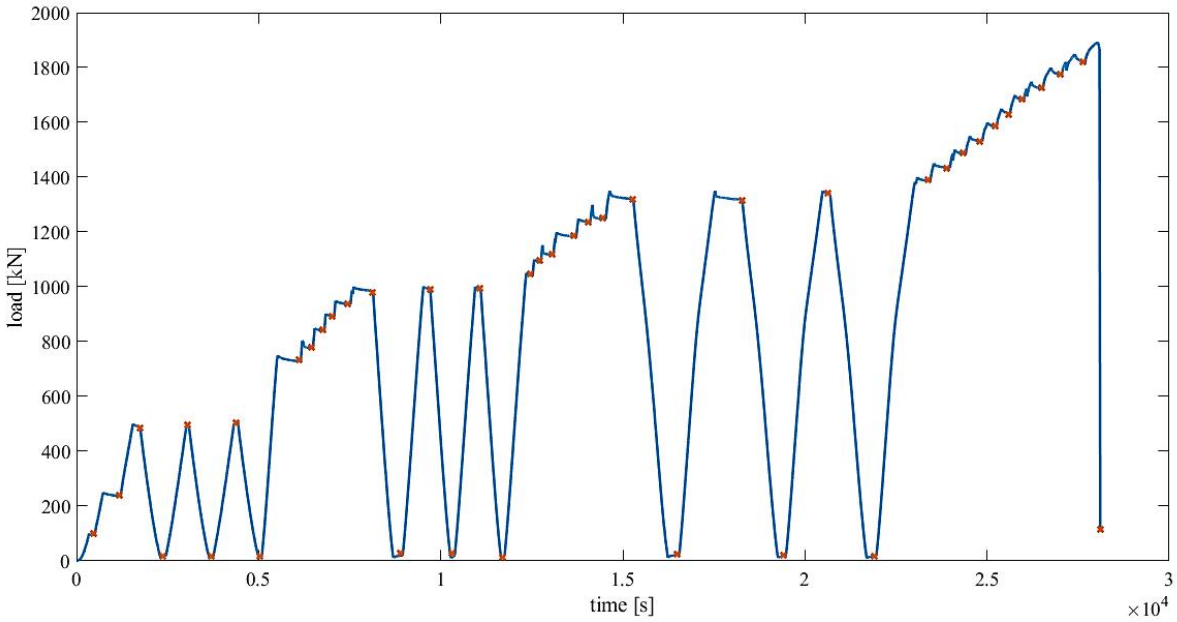

Figure 4.17: Load History of HPZ01

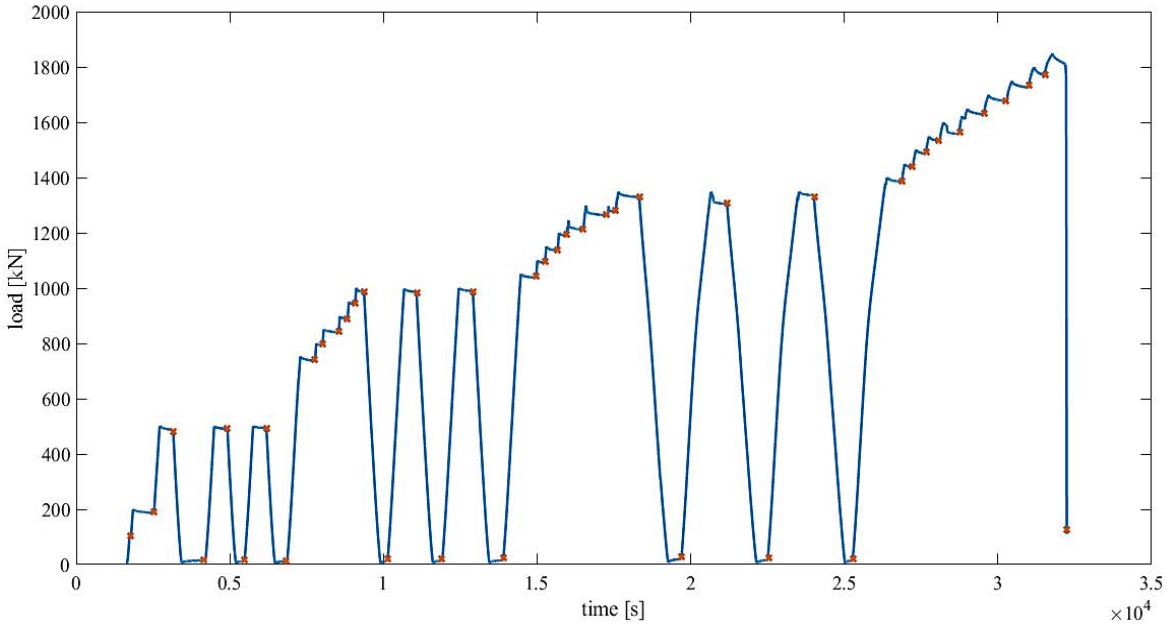

Figure 4.18: Load History of HPZ02 with Selected Intervals

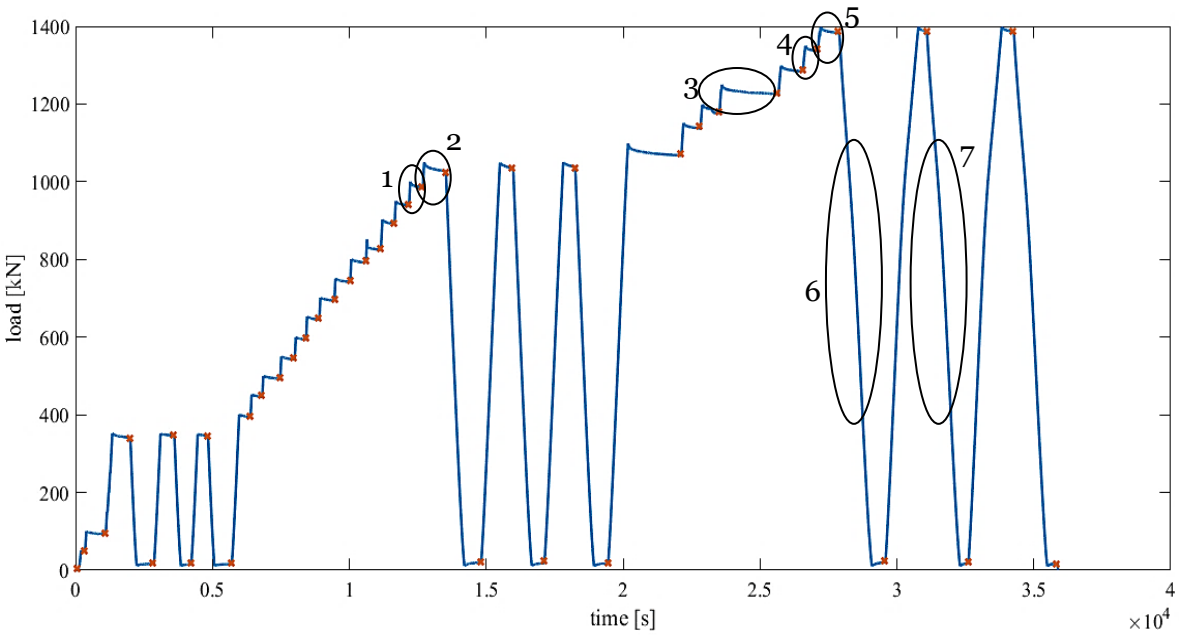

Figure 4.19: Load History of HPZ03 with Selected Intervals

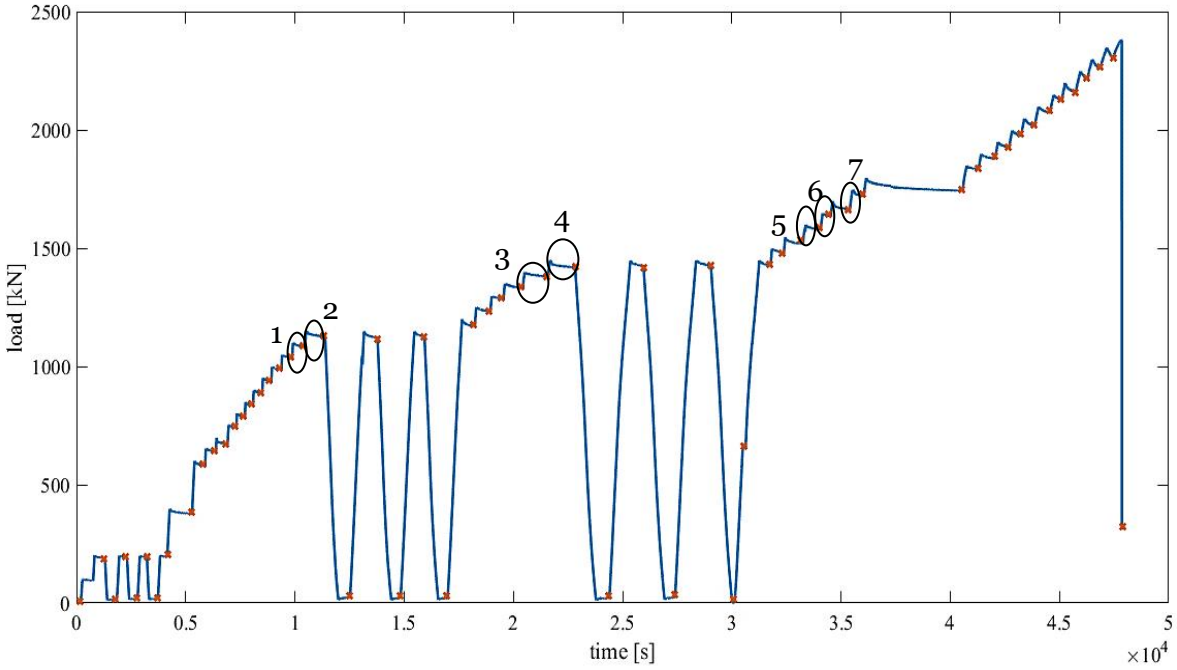

Figure 4.20: Load History of HPZ04 with Selected Intervals

5 Results from Helperzoom Girders

5.1 Test Results

5.1.1 Load-Displacement Relationship

Figure 5.1 shows the load-displacement response of all the four beams, following the loading scheme given in Section 4.6. An overview of the observations made during the experiment is shown in Table 5.1. The table shows the point of occurrence of the first flexure crack, first shear crack and the failure. These observations can be verified using the load-displacement plots in Figure 5.1, where the change in slope is evident around the point where the cracks are reported.

HPZ01 and HPZ02 are similar tests in regard to distance of loading jack from the support. The behaviour between the two experiments is similar, with a comparable maximum load and a similar failure mechanism. The first flexure crack occurs at 965 kN for HPZ01 and 1000 kN for HPZ02, whereas the first shear crack occurs at 1350 kN for HPZ01 and 1300 kN for HPZ02. The failure load for HPZ02 is slightly smaller than that for HPZ01.

Similarly, HPZ03 and HPZ04 are similar tests. Both the beams show similar behaviour, with the load at which the flexural crack occurs being is a bit higher for HPZ04. The load at which the shear crack occurs, and the failure load is higher as well for HPZ04. The reason for this discrepancy can be the difference in the prestressing levels for both the beams or the variability in the value of concrete tensile strength.

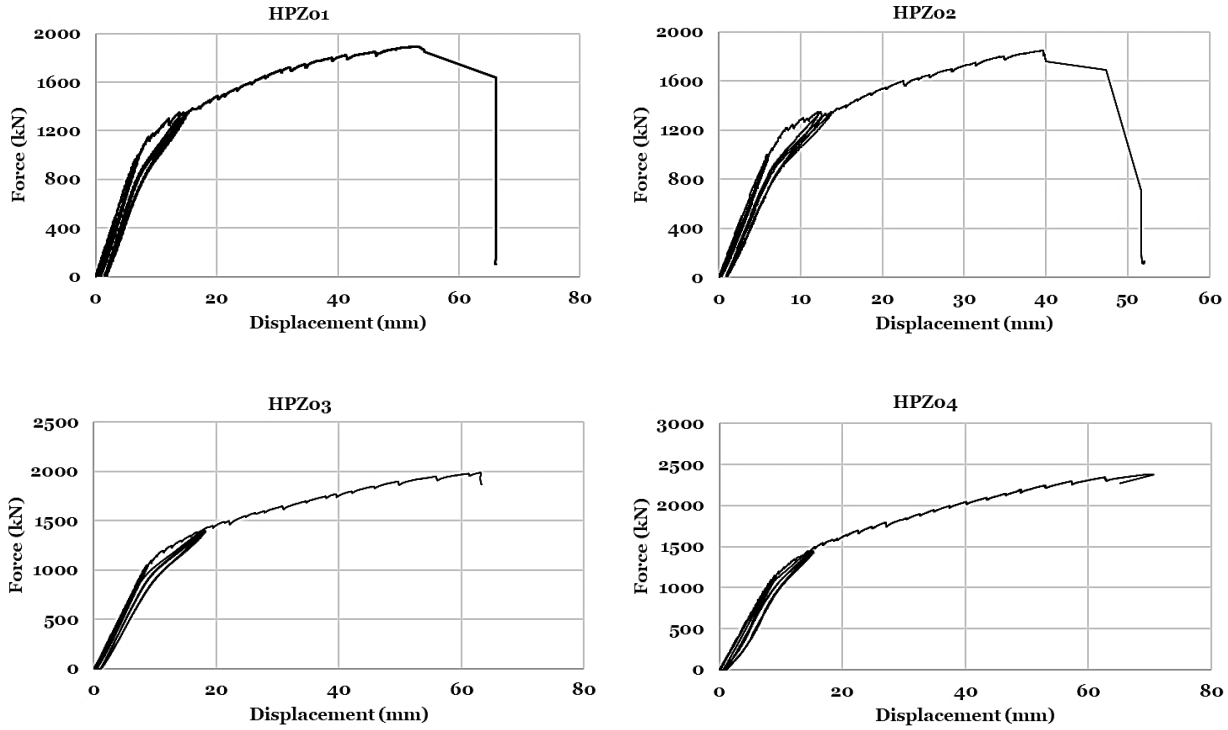

Figure 5.1: Load-Displacement Relationships for the Helperzoom Beams

Table 5.1: Test Observation for Helperzoom Beams

	Flexure Crack (kN)	Shear Crack (kN)	Failure (kN)
HPZ01	965	1350	1890
HPZ02	1000	1300	1850
HPZ03	1050	1400	1990
HPZ04	1100	1450	2380

5.1.2 Failure Mode

Figure 5.2 shows the state of Helperzoom beams at failure along with their associated failure modes. The pictures are taken from the backside of the beam where the DIC measurements were made. HPZ01 and HPZ02 beams fail in shear-compression/flexural shear, while HPZ03 and HPZ04 fail in shear-compression/ concrete crushing in the compression strut.

HPZ01 (Shear Compression/Flexure Shear)

HPZ02 (Shear Compression/Flexure Shear)

HPZ03 (Shear Compression/ Concrete Crushing)

HPZ04 (Shear Compression / Concrete Crushing)

Figure 5.2: Beams at Failure along with Failure Modes

5.2 AE Results

5.2.1 Cumulative AE Energy

The cumulative AE energy released during the complete loading cycle is shown in Figure 5.3 and Figure 5.4 along with DIC measurements at some critical points. The reported cumulative AE energy includes the sum of AE energies obtained at all the sensor locations.

In Figure 5.3, for HPZ03, the DIC measurements are shown for instances where the first flexure crack and first shear cracks are detected. For the instance when the first shear crack is detected a sudden spike in cumulative AE energy is visible. Similar spikes are visible for the case of HPZ04 (Figure 5.4) when the first shear crack occurs and near failure. The released AE energy thus proves to be effective in determining the point of occurrence of the cracks.

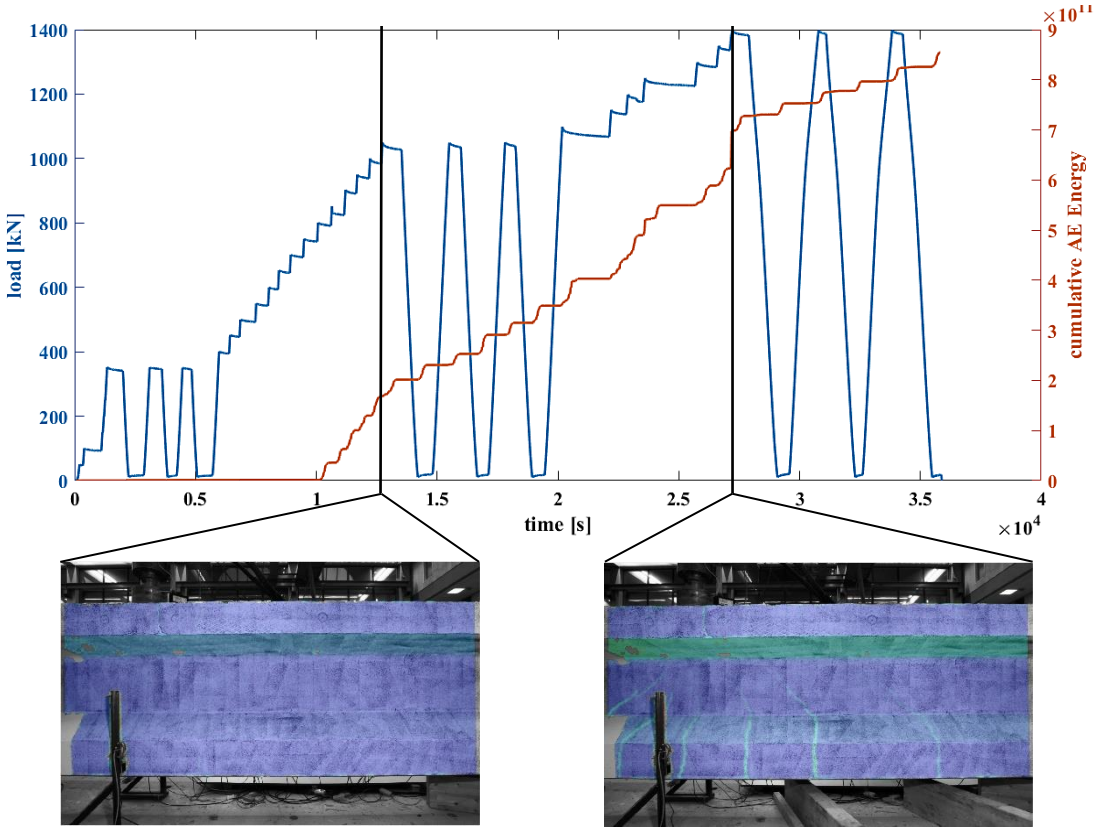

Figure 5.3: Cumulative AE Energy released throughout loading history for HPZ03

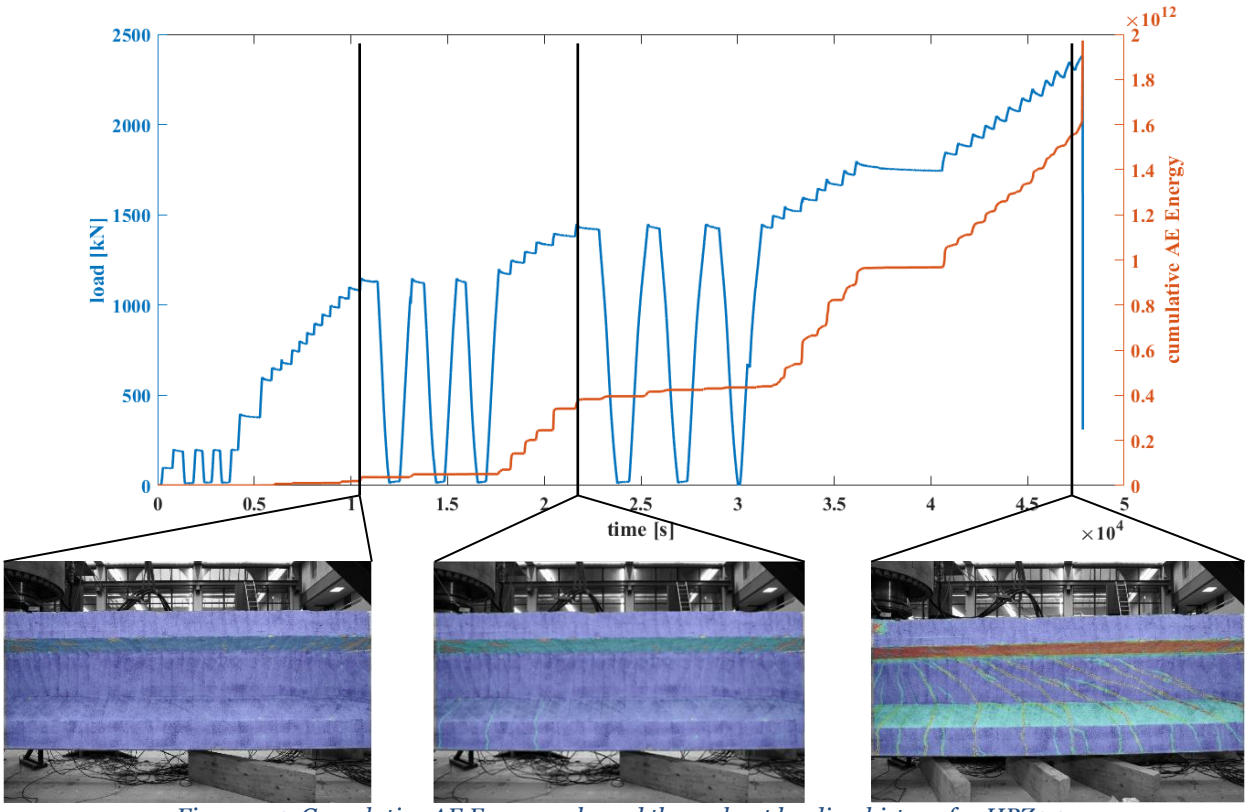

Figure 5.4: Cumulative AE Energy released throughout loading history for HPZ04

5.2.2 AE Signal Clustering

As per the methodology proposed in Section 2.4.2, the AE signals obtained during load-interval 1350-1400 kN of HPZ03 are divided into two clusters. The value for maximum cophenetic distance (d_o) is taken as 0.75. The magnitude of d_o is set to have at least 2 major clusters at the end of clustering. Figure 5.5 and Figure 5.6 shows how the AE signals obtained from two distinct clusters differ in their shapes. Figure 5.5 shows two signals from Cluster 1 and Figure 5.6 shows two signals from cluster 2 along with their respective Fourier spectrums. AE signals from Cluster 1 are relatively homogenous in their frequency content with a major peak around 100 kHz. In addition to this, these signals lack frequency component of less than 80 kHz. On the other hand, AE signals from cluster 2 have a wider frequency spectrum with a significant part of the spectrum lying below 80 kHz. Cluster 1 has a frequency spectrum dominating towards the higher end of the spectrum and cluster 2 has a frequency spectrum which dominates towards the lower end. Thus, the proposed AE signal-based clustering algorithm can differentiate between the signals from different sources. The source that these clusters belong to is discussed in Chapter 6.

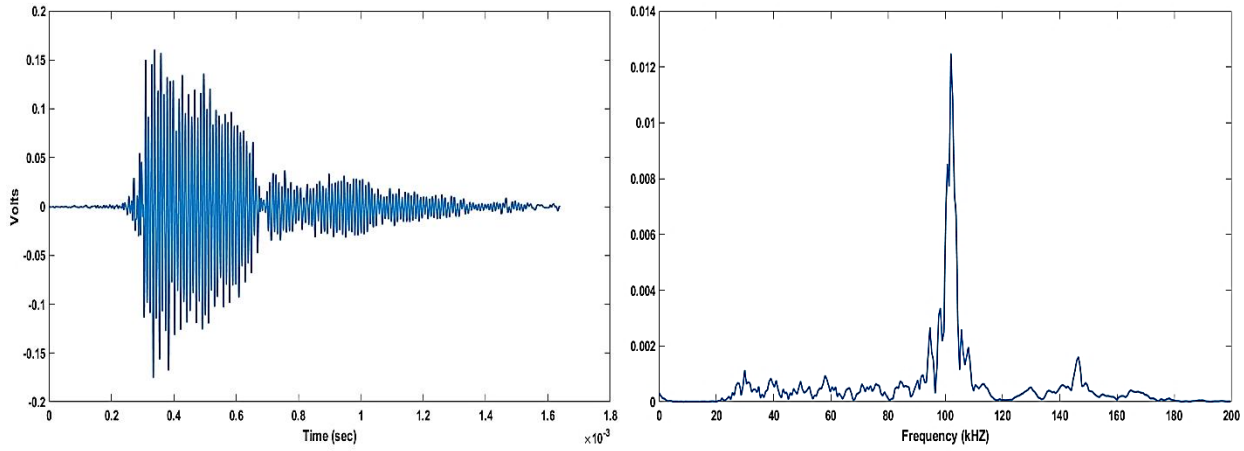

Signal 1

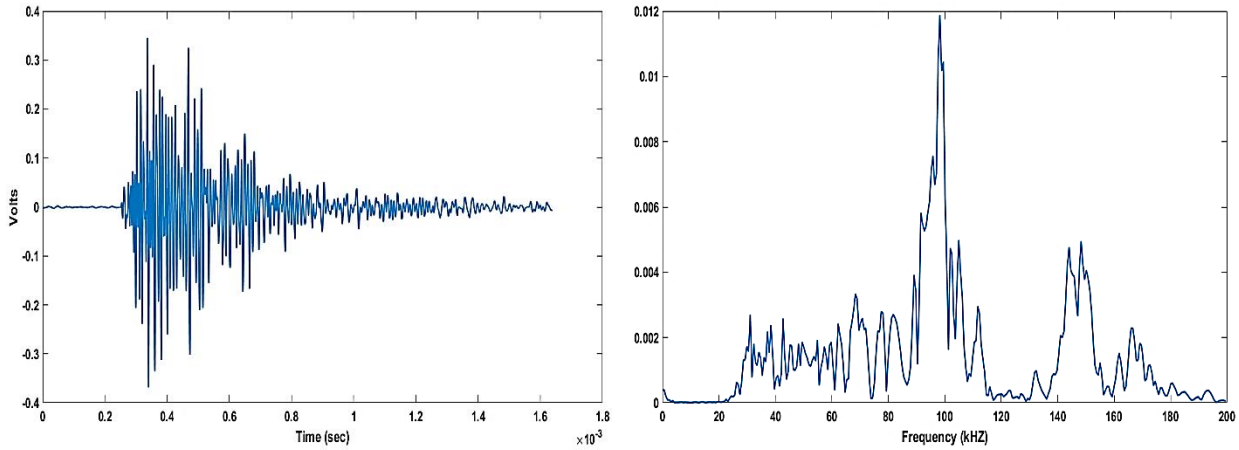

Signal 2

Figure 5.5: Cluster 1 Signal in Time and Frequency Domain

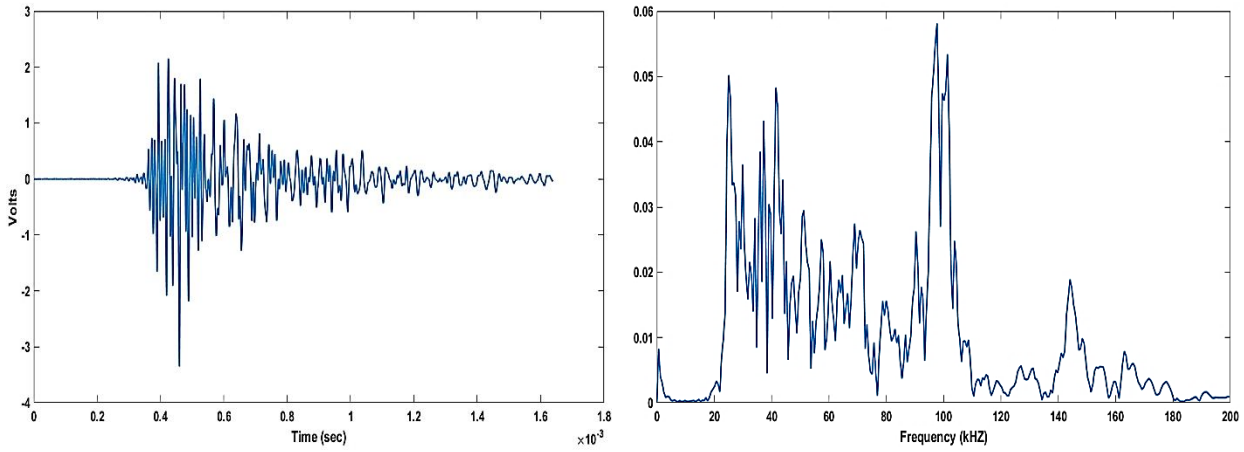

Signal 1

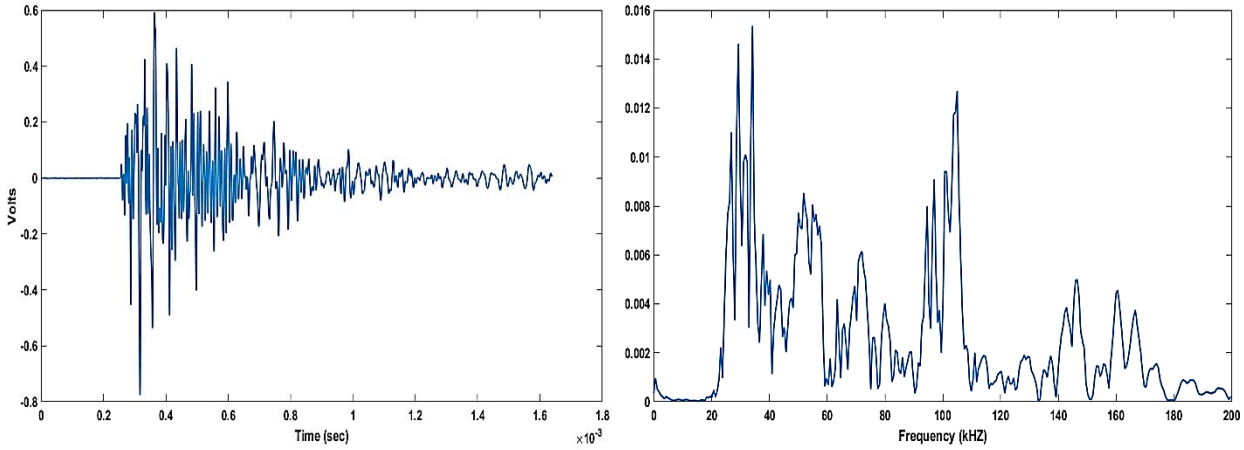

Signal 2

Figure 5.6: Cluster 2 Signal in Time and Frequency Domain

5.2.3 AE Source Localization

Figure 5.7 shows the source localization results for HPZ03 during the intervals selected in Figure 4.19. The AE events corresponding to Cluster 1 are shown using blue markers and AE events corresponding to Cluster 2 are shown using red markers. In this thesis, cluster 1 always refers to the cluster with higher mean average frequency and cluster 2 refers to the cluster with lower mean average frequency.

Interval 1 (1000 kN) and interval 2 (1050 kN) in Figure 5.7 represent the intervals corresponding to the occurrence of the flexure crack. It is noted that the first crack occurs between sensor 11 and sensor 12, as AE events are concentrated between these two sensors, which is as per the experimental observation. From interval 3 to interval 5 as the load increases, the AE events associated with cluster 1 (blue markers) follow the crack tip. On the other hand, cluster 2 based AE events (red markers) are seen along the complete crack length. A similar observation can be made about Interval 6 (unloading interval) and Interval 7 (reloading interval).

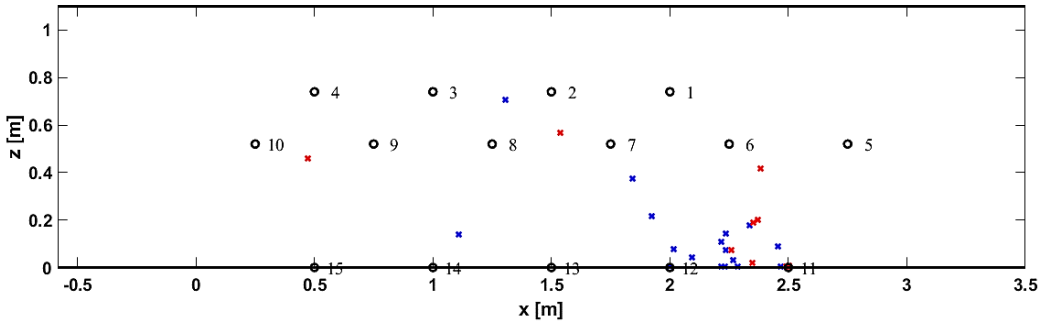

Interval 1

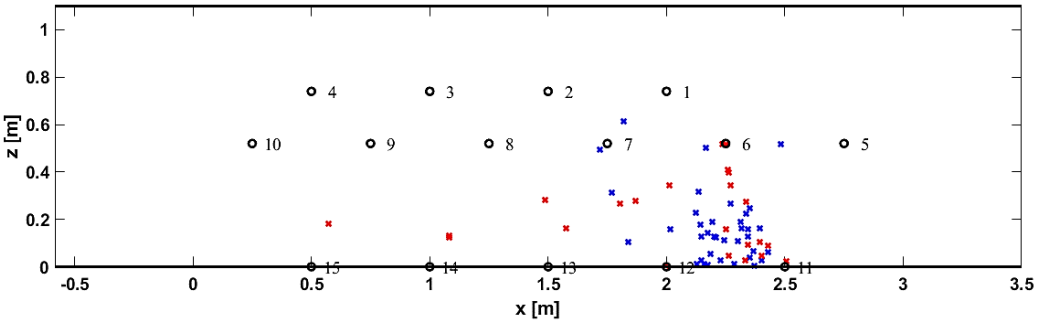

Interval 2

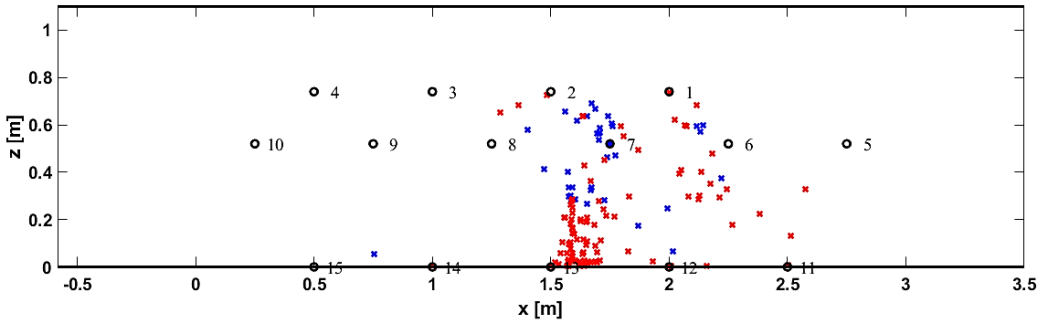

Interval 3

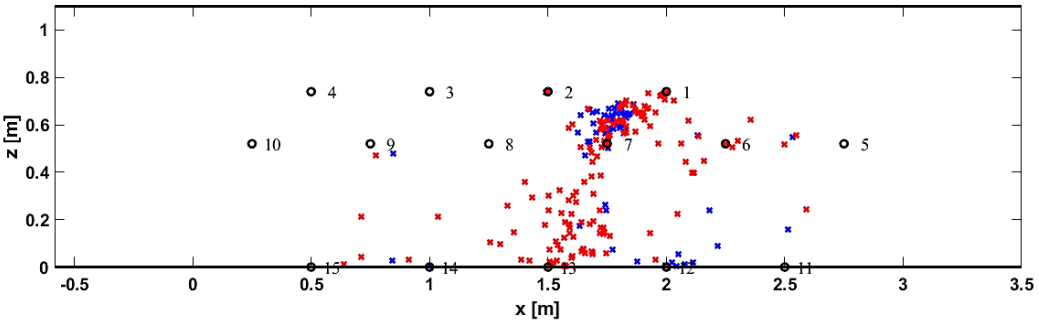

Interval 4

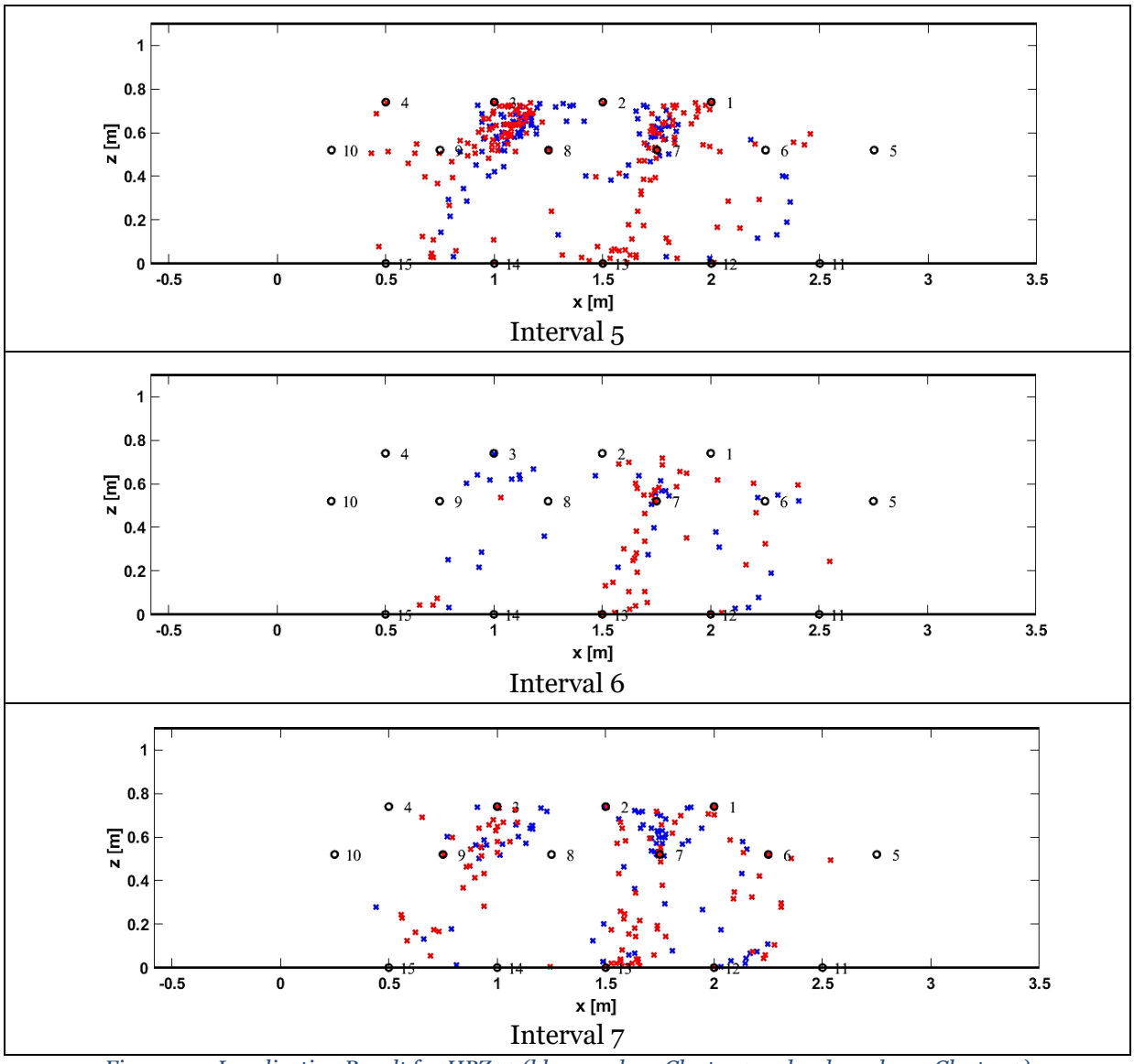

Figure 5.7: Localization Result for HPZ03 (blue marker- Cluster 1 and red markers- Cluster 2)

6 Evaluation of AE Source Classification Methods

Chapter 2.4 gave a brief overview of the algorithms used for AE classification in literature. In this chapter, the classification methods in this thesis are discussed in regard to parameter-based classification and signal-based classification. The proposed methodologies are then used to classify the AE data obtained from Helperzoom beam to separate the AE activities due to crack opening and AE activities due to friction.

6.1 Classification Methodology

6.1.1 Parameter-based Classification

In this thesis, the bivariate and the multivariate classification methods are investigated (chapter 2.4.1). The bivariate classification is performed as per the JCMS recommendation using the k-means and Gaussian mixture modelling algorithms. Two bivariate RA-AF based methods are used in this thesis and are implemented using predefined MATLAB functions. First is the Gaussian Mixture Modeling (GMM) [19], where the probability of each AE event belonging to a cluster is determined. In GMM, firstly the number of clusters to be identified is determined then a probability density function based on mean, covariance and mixing probability is defined. An initial estimate is made of these parameters for each cluster and the probability of each data-point belonging to a cluster is determined using the probability density function. Then the parameter values are revised based on the obtained probabilities. This process is repeated until convergence.

Second is the k-means clustering algorithm [51]. In k-means clustering, firstly an initial estimate of cluster centre is made then for each data point the nearest cluster centre (using Euclidean distance) is identified. Then, the cluster centre is modified by calculating the coordinate-wise average of all the data points that are nearest to the previous centre. This process is repeated till the algorithm converges to a local minimum of the within-cluster sum of squares.

Multivariate classification is investigated with the help of principal component method discussed in chapter 2.4.1. Five basic AE parameters are used, namely, peak AE amplitude, pre-peak count, post-peak count, rise time and duration of the signal. The dimension of the dataset is reduced to 2 by defining a PCA space representing the maximum covariance direction.

In addition to the above approaches, source classification is also performed using the partial power spectrum of the AE signal. As discussed earlier (chapter 2.4.1), AE signals from different sources have different frequency content. In the Fourier spectrum of the signal, the distribution of the signal energy over frequency is determined using partial power spectrum. In this thesis, 4 segments for partial power are defined as shown in Table 6.1 and the contribution of a signal to each segment is evaluated as a percentage. AE signals which have a contribution of more than 50% from segment I and segment II are clustered into one group and the others are clustered into another group. This is done to have 2 clusters at the end of classification.

Table 6.1: Partial Power Segments

Segment	From (kHz)	To (kHz)
I	0	19.5
II	19.5	68
III	68	117
IV	117	250

6.1.2 Signal-Based Classification

Van Steen [20] proposed the waveform-based clustering algorithm for AE signal in the time domain, the methodology for which was presented in chapter 2.4.1. In this thesis clustering in the frequency domain is also performed. The AE spectrum in the frequency domain is obtained by performing the Fourier Transformation of the time signal. As the energy is concentrated only in a small part of the Fourier domain, frequency spectrum from 0 to 200 kHz is only considered for clustering. Half range Fourier spectrum of one of the recorded signals is shown in Figure 6.1. Windowing the frequency facilitates in identifying the differences between the two AE signals using cross-correlation. The methodology for clustering in the frequency domain is the same as in the time domain.

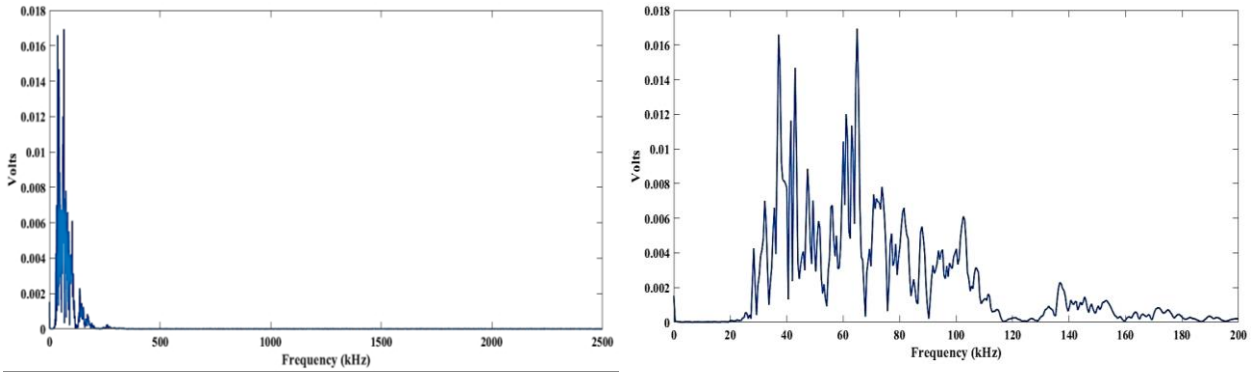

(a) Half Fourier Spectrum (b) Windowed Spectrum (0-200 kHz)

Figure 6.1: Fourier spectrum of AE signal

In this thesis, the maximum cophenetic distance (d_o) required for clustering in the frequency domain is set to 0.6 and for clustering in the time domain, it is set to 0.75. The value of 'd_o' is set to have at least 2 major clusters at the end of clustering. A higher value of 'd_o' can result in all the signals being clustered into one cluster. For each AE event, several AE signals are detected but only one signal per event is used. To associate the detected AE signals to an AE event, source localization is performed and the signal from the nearest sensor is used. The signal detected by the sensor closest to the source is selected as the representative signal for that source to minimize the attenuation-based effects. Before clustering, AE signals were filtered with a minimum signal to noise ratio of 10. The noise was taken as the maximum value of the signal in the first 260 micro-seconds of the signal.

6.2 Signal-Based Approach for Crack Classification

This section compares the signal-based clustering in time and frequency domain. Table 6.2 shows two clusters in which the AE signals from interval 4 for HPZ03 are divided when the clustering is performed using the time signal and frequency spectrum. When using the frequency spectrum for clustering, two major clusters are observed with 74 and 156 signals each. Whereas, when using the AE time signal two clusters with 116 and 104 signals each are obtained. To draw up the similarity in the clustering results, common AE signals in each cluster are identified and reported. Cluster 1 obtained from clustering in the time domain and frequency domain have 70 common signals and Cluster 2 has 100 common signals. This results in 74% similarity in the clustering results obtained in time and frequency domain. As the number of clusters obtained in the end can be more than 2, for comparison the two clusters with the highest number of the AE signals are considered in Table 6.2.

Although clustering results are similar, the time spent to cluster in the time domain is about 6 hours while clustering in frequency domain takes around 1.5 hours. Clustering in time domain takes more time because while calculating the cross-correlation coefficient several time lags are applied to one of the signals in search of the value of time lag for which maximum cross-correlation is observed. Whereas in the frequency domain the cross-correlation function is to be evaluated only once. The signal classification obtained from clustering in time and frequency domain is almost similar. Thus, based on the time duration required, clustering in the frequency domain is a better alternative as it saves considerable computation time.

Table 6.2: Clustering similarity in time and frequency domain for interval 4, HPZ03

	Cluster 1	Cluster 2
Frequency Domain	74	156
Time Domain	116	104
Common Points	70	100
Common Percent	73.9	

As shown in the localization plots from Section 5.2.3, the AE signals can be clustered into two major clusters but it is not clear as to what source these clusters belong. To identify the source of an AE event, predefined labels are needed. In this case, two such labels are identified, namely, crack opening (or tension) and friction. At tensile cracking, the crack sides move away from each other, causing a transient volumetric change in the material. Therefore, majority of the energy is released in the shape of longitudinal waves. At friction, the sides of cracks slide across each other, giving shape deformation which releases most of the energy in form of S-waves.

For HPZ03, the first flexure crack was obtained towards the end of the second loading cycle (interval 1). The AE activities in this interval are expected to be tension dominant; thus, interval 1 is selected as a label for crack opening. Interval 6 is the unloading interval and it is expected to contain cracks which can act as a label for friction. This is because in this interval no new cracks are formed, and the major AE activities generate due to friction between closing crack surfaces.

Using AE signal-based clustering in the frequency domain, Interval 1 for HPZ03 can be classified into two clusters; cluster 1 contains 18 signals and cluster 2 contains 11 signals. The major cluster, i.e. Cluster 1 of interval 1, is selected as a known label for signals from tensile cracking. Similarly, interval 6 from HPZ03 can be classified into 2 clusters of 36 and 51 signals each and the major cluster from interval 6(with 51 signals) is selected as a label for friction. Another way to identify or verify the nature of the cluster is by comparing the position of each cluster events through the localization plots presented in Chapter 5.2.3. The AE cluster concentrated near the crack tip can be labelled as the one associated with tension.

Table 6.3 shows the clustering results obtained for intervals marked in Section 4.6. It is observed that the clusters which are closer to the tensile cracking label are far from friction label. Thus, the process of using the known label as discussed earlier proves efficient in labelling other clusters. Figure 5.7 shows the localization result for the selected intervals of HPZ03. The blue markers represent the AE event associated with Cluster 1 and red markers are associated with Cluster 2.

Interval 1 (1000 kN) and interval 2 (1050 kN) in Figure 5.7 represent the occurrence of the first flexure crack which causes AE activities corresponding to pure tension. Thus, the number of AE events associated with tension is higher than those associated with friction for interval 2 (Table 6.3). For the later intervals, as the cracks propagate further and incline into the web, the number of AE events associated with friction increase. AE events associated with tension are majorly localized around the crack tip while those associated with friction occur both near the crack tip and along the length of the crack. The friction-based activities thereby increase when inclined cracks occur in the beam due to increased shear displacement at crack surfaces. A similar conclusion can be derived from Figure 6.2, where the percentage of AE events related to tension is plotted over the intervals.

Table 6.3: Clustering Result for HPZ03

Interval	Cluster	No. of signals	Cophenetic Distance	
			Tension	Friction
Interval 2	Cluster 1	37	0.4203	0.6892
	Cluster 2	23	0.6105	0.4541
Interval 3	Cluster 1	46	0.4755	0.582
	Cluster 2	106	0.5672	0.4904
Interval 4	Cluster 1	74	0.4441	0.6955
	Cluster 2	156	0.6087	0.4797
Interval 5	Cluster 1	119	0.4679	0.6939
	Cluster 2	177	0.5751	0.4997
Interval 7	Cluster 1	89	0.4768	0.6214
	Cluster 2	104	0.6909	0.4481

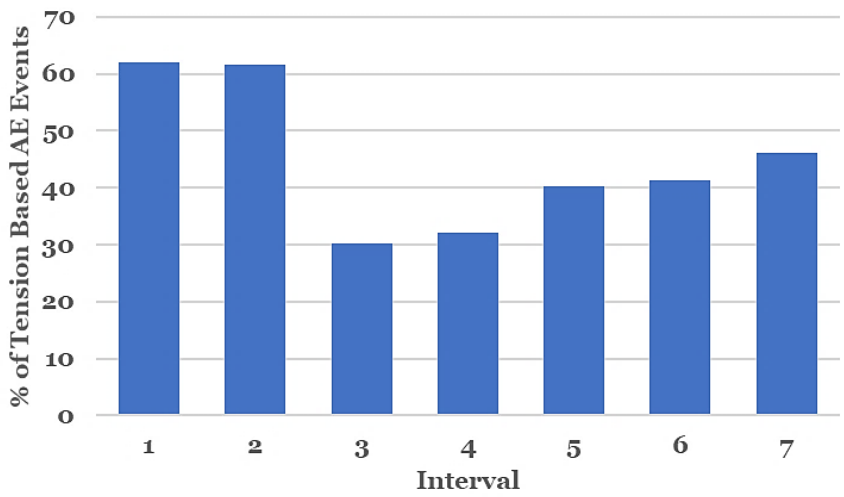

Figure 6.2: Percent of Tension Based AE Events for HPZ03

6.3 Parameter-Based Approach for AE Classification

In this section, a comparison is made between the existing parameter-based clustering methodologies and the AE signal-based methodology.

6.3.1 RA-AF Analysis

Following the JCMS recommendation, the dataset is clustered into two groups and the results are compared with signal-based clustering. The clustering methods used here are, namely, K-means clustering [24] and Gaussian Mixture Modelling (GMM) [19]. The clustering result obtained for interval 4 (1350 kN) for HPZ03 using K-means, GMM and waveform clustering is presented in Figure 6.3. The same plot for interval 7 (1700 kN) of HPZ04 is shown in Figure 6.4.

In the case of HPZ03, dominant shear cracks were not recorded around interval 4, thus GMM is not able to identify clusters of two kinds. Most of the AE signals are put into the same cluster (Figure 6.3, GMM). For K-means a hardline clustering is obtained. Signals with higher AF values are clustered into one group and those with lower AF values are clustered into the other. Whereas in the case of signal-based clustering, two distinct clusters are obtained but they are not separated by a clear boundary. Cluster 1 represents the AE signals which are associated with a crack opening label and Cluster 2 represents the AE signals related with friction label (Table 6.3). For HPZ04 Interval 7 (Figure 6.4), a clear cluster for shear crack is obtained using GMM. K-means also gives a similar plot in this case. For waveform-based clustering bigger Cluster 2 is obtained, which relates to shear crack and friction effects. In addition to this for the selected interval from HPZ04 AE events with relatively higher RA value are released as evident from the x-axis limit in Figure 6.3 and Figure 6.4. This is due to major shear activity that occurred in the beam during interval 7 for HPZ04. Figure 6.5 shows the localization result for this interval, where large inclined cracks can be seen which are not present in localization plot for HPZ03 (Figure 5.7).

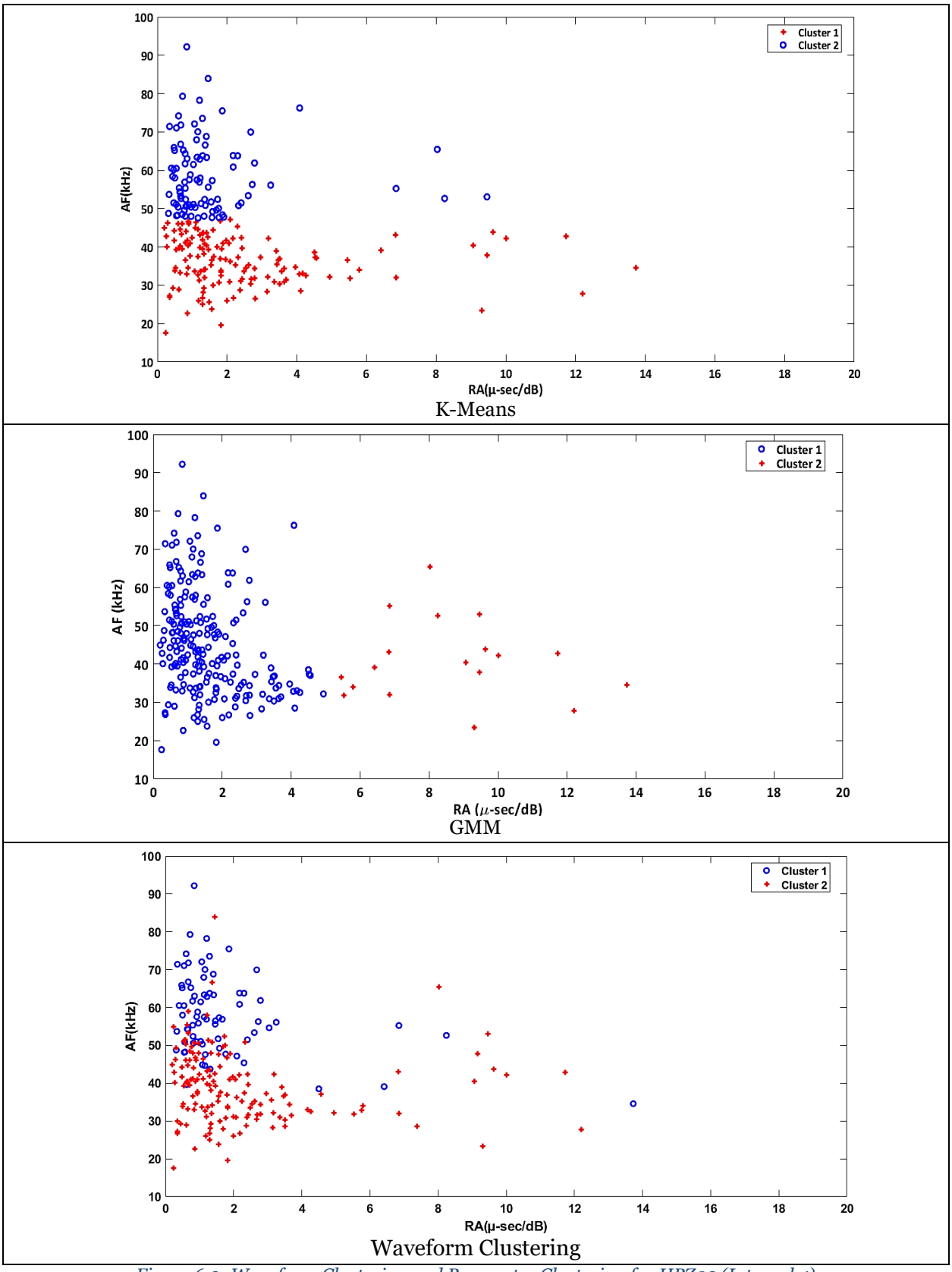

Figure 6.3: Waveform Clustering and Parameter Clustering for HPZ03 (Interval 4)

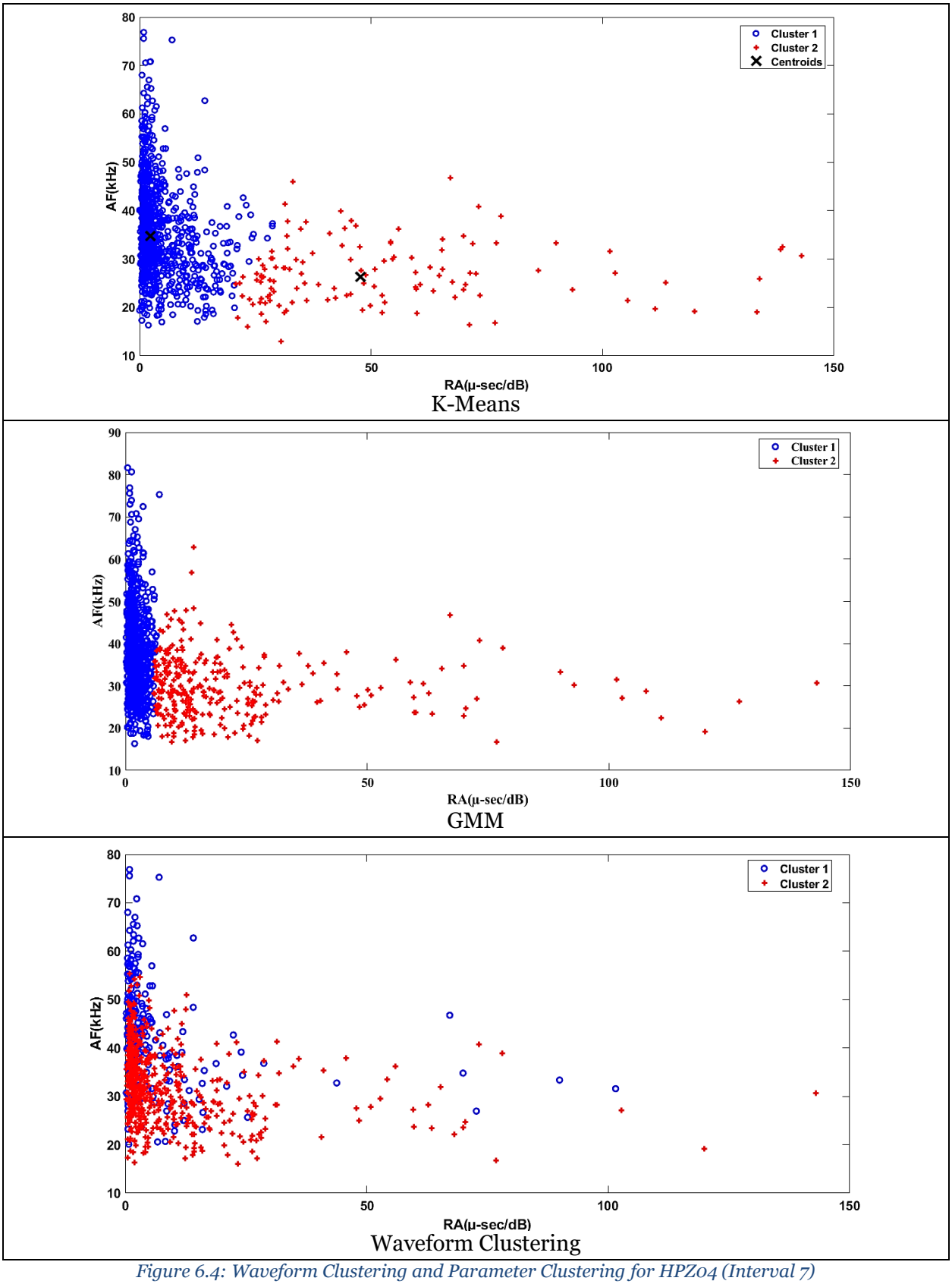

Figure 6.4: Waveform Clustering and Parameter Clustering for HPZ04 (Interval 7)

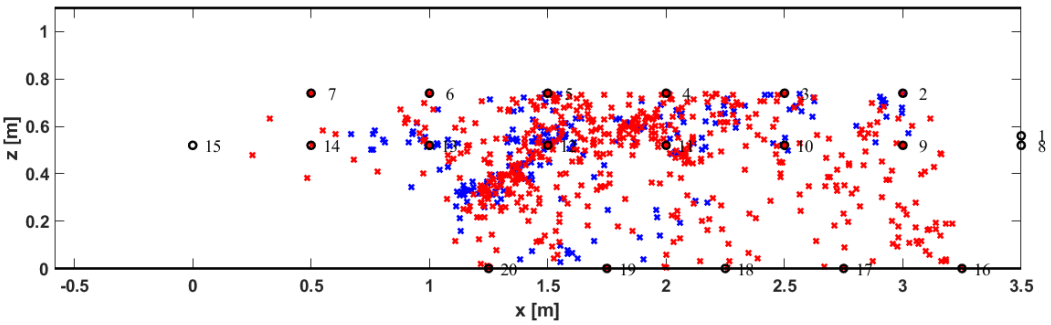

Figure 6.5: Localization Result for Interval 7, HPZ04

For a parameter-based clustering method like GMM, the occurrence of shear crack can be identified as per the JCMS recommendation. Initiation of shear crack has significant importance in defining the structural integrity of RC members. Thus, a parameter-based clustering method like GMM can play a big role in identifying structural health. Based on results obtained, the occurrence of the shear crack using parameter-based clustering is not clear unless strong shear activities occur. Waveform approach, on the other hand, provides a possibility of AE clustering, which is more sensitive than the parameter-based approach. Using the signal-based clustering, it is possible to cluster AE events into tensile cracking and friction-based events. Events associated with tensile cracking occur throughout the experiment, whenever a new crack surface is developed. On the other hand, friction-based effects are initially caused due to friction at the aggregate surface and later they increase as the relative shear displacement at crack surface increases.

6.3.2 Principal Component Analysis (PCA)

Table 6.4 shows the eigenvalues and corresponding contribution to the variance of the 5 eigenvectors obtained from singular value decomposition (SVD) for Interval 7 of HPZ04. The first and the second eigenvector contribute to 84% of the total variance, thus the principal components only in these two directions are considered. The data points are then divided into 2 clusters using k-means clustering as shown in Figure 6.6.

Table 6.5 and Table 6.6 shows how the signal-based clustering compares to PCA based clustering and GMM. Comparing the signal-based clustering and PCA yields 56.3 % similarity and the comparison between signal clustering and GMM yields 47.3 % similarity. Although PCA performs better than GMM, it is still not able to identify small changes in AE signal as signal-based clustering. This is because although PCA takes more parameters under consideration than GMM, it still cannot capture the complete signal behaviour.

Table 6.4: Contribution of Eigenvector to PCA space (Interval 7, HPZ04)

S.No.	Eigenvalue	% Variance Contribution
1	2217	53.98
2	1227	29.8
3	598	14.5
4	72	1.55
5	34	0.61

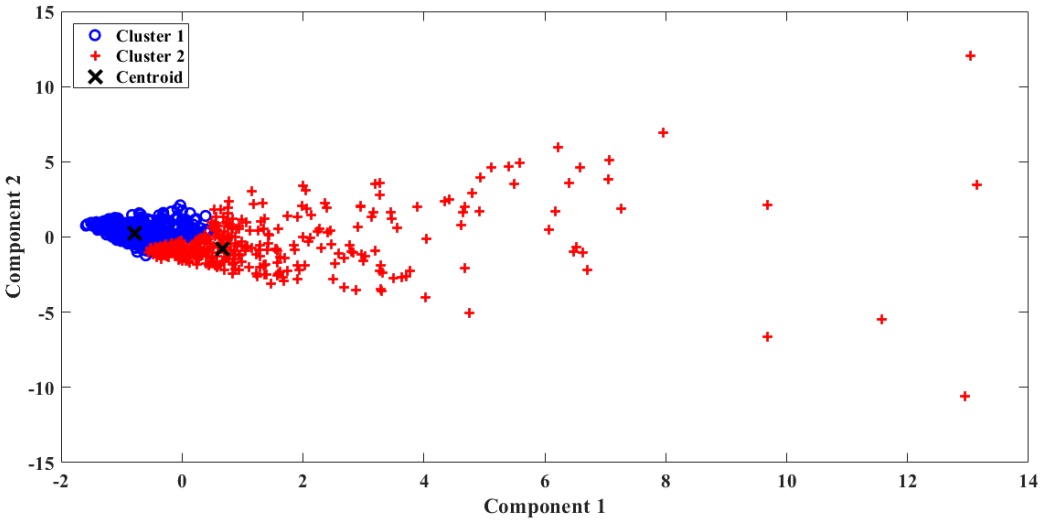

Figure 6.6: Principal Component for Interval 7 of HPZ04

Table 6.5: Comparison between signal clustering and PCA (Interval 7, HPZ04)

Step	Interval 7	
	Cluster 1	Cluster 2
Wave Clustering	233	593
PCA	314	517
Common Points	92	373
Total Percent	56.3 %	

Table 6.6: Comparison between wave clustering and GMM (Interval 7, HPZ04)

Step	Interval 7	
	Cluster 1	Cluster 2
Wave Clustering	233	593
GMM	569	262
Common Points	182	209
Total Percent	47.3 %	

6.3.3 Partial Power Spectrum

Table 6.7 shows that AE clustering using partial power spectrum has a similarity of 77.4% with signal-based clustering. Hits with partial power of more than 50 %, between segment III and segment IV, are assigned cluster 1 and rest are assigned as cluster 2. Figure 6.7 shows the localization result using the clusters obtained from partial power clustering. Comparing with localization result from Figure 5.7 (Interval 4) it is noted that the difference in results occurs around the crack tip. In case of a signal-based cluster, some activities around the crack tip got clustered as a friction-based activity which got labelled as crack opening in partial power clustering.

Partial power-based AE clustering helps in classifying activities based on Fourier spectrum efficiently. It takes considerably less time to execute than the signal-based clustering and is simple in its approach. Signal-based clustering on an average takes more than an hour to execute while partial power method takes a couple of minutes. The only point of concern is deciding the range of respective partial power spectrum, which will require insight into the type of AE source emitted and the type of AE acquisition system.

Table 6.7: Comparison between wave clustering and Partial power clustering

Step	Interval 4	
	Cluster 1	Cluster 2
Wave Clustering	74	156
Partial Power	112	121
Common Points	70	108
Total Percent	77.4 %	

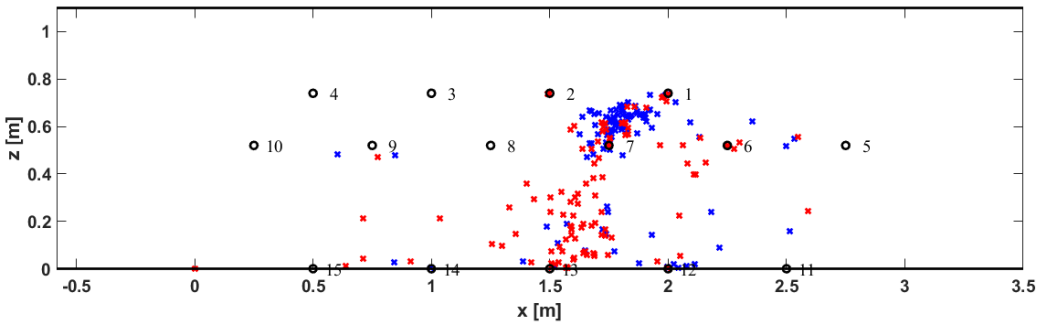

Figure 6.7: Localization- Partial Power Spectrum (Interval 4, HPZ03)

6.4 Concluding Remarks

A methodology for AE signal-based classification in the frequency domain was proposed. Results obtained from signal-based classification were then compared with parameter-based classification methods. Based on the results obtained following conclusions can be made:

i. AE signal-based classification in frequency domain yields similar result as classification in the time domain but it takes lesser time. For a certain interval, classification in time domain takes 6 hrs while classification in frequency domain takes 1.5 hrs.
ii. AE signal-based classification method can draw out relatively smaller differences in the AE source. It yields better-quality results when compared to parameter-based classification methods like RA-AF analysis or principal component analysis.
iii. Using partial power spectrum method for AE classification yields similar result as the AE signal-based classification and it takes considerably lesser time, a couple of minutes compared to hours. Although, care must be taken while deciding the range of the segments in the frequency spectrum.

7 AE Attenuation

AE waves in concrete, similar to their seismic counterpart [52], propagate in form of two basic elastic waves, namely, body waves and surface waves. These waves, before being detected by the AE sensors, propagate through concrete and lose energy in the due process. This loss in energy of the AE signal between the source and the receiver is referred to as AE attenuation. AE attenuation is generally expressed in terms of amplitude loss. Thus, in this study first the AE attenuation is studied in terms of amplitude loss and then it is used to determine AE attenuation in terms of energy. A direct relationship between amplitude and the square root of energy is used to estimate attenuation in terms of energy.

7.1 Measurement of wave transfer properties in concrete medium

7.1.1 Test setup

In the uncracked state, the main sources of AE attenuation are geometrical attenuation and material attenuation. Measurement using point source and point receiver are used to estimate the attenuation in the uncracked stage. Figure 7.1 shows the experiment setup. Seven sensors are placed in one line with the centre to centre spacing of 80 mm and auto-sensor test (AST) is performed. Auto Sensor Test (AST) is a built-in feature within the AE acquisition system. The AST feature allows any sensor to emit a simulated acoustic emission wave that other sensors can detect, thus giving the feedback on the state of material between the sensors. This is accomplished by allowing each sensor to act as a source, while others act as a receiver. The pulse emitted by the source sensor is then received by other sensors and it is processed as a typical AE event. This process is repeated until every sensor in the experimental setup has acted as a source, while other sensors act as a receiver.

Starting from sensor 1 each sensor emits pulse while others receive, and this is continued till sensor 7 emits the pulse and the other sensors receive it. The sensor next to the source sensor is taken as the reference sensor. When sensor 1 is the transmitter, the signal from sensor 2 is taken as the reference signal and when sensor 7 is the transmitter, the signal from sensor 6 is taken as reference.

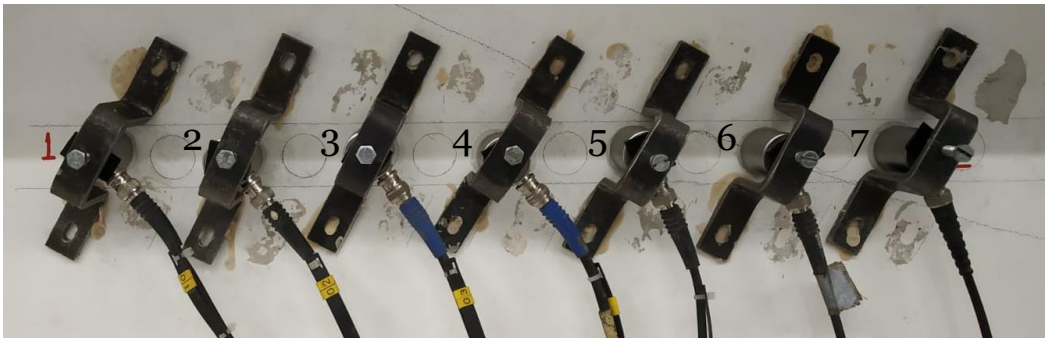

Figure 7.1: Baseline Measurement

The trend for total attenuation can be obtained by simply using the AE energy at sensor locations and plotting it against the propagation distance. For material attenuation, firstly the loss due to

geometric spreading needs to be removed from the recorded signal. This is achieved by multiplying each AE signal by the square root of the propagation distance with respect to the source. In this test, the wave speed can also be estimated from the travel time-distance curve, which is an important parameter for source localization.

7.1.2 Results

Figure 7.2 shows the scenario in which sensor 1 acts as the source and all other sensors receive. Average peak amplitude decreases on moving from sensor 1 to sensor 7 due to propagation-based losses and the arrival time increases. In Figure 7.3, the arrival time is plotted against the distance from the source. The resulting curve is a straight line, the slope of which can be used to calculate the surface wave speed. The arrival times are manually picked, and surface wave speed of 4670 m/s is reported.

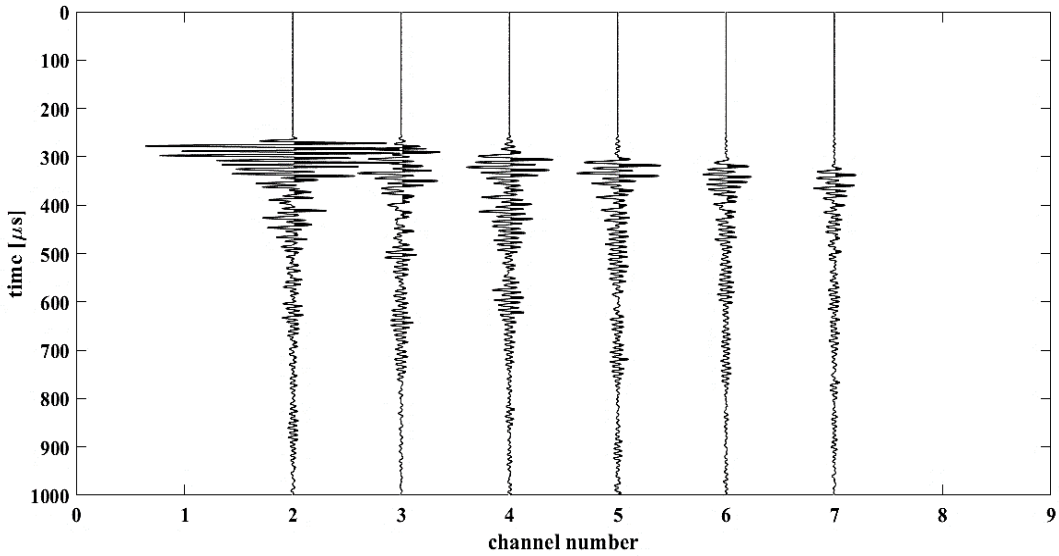

Figure 7.2: Waveforms at different sensor locations

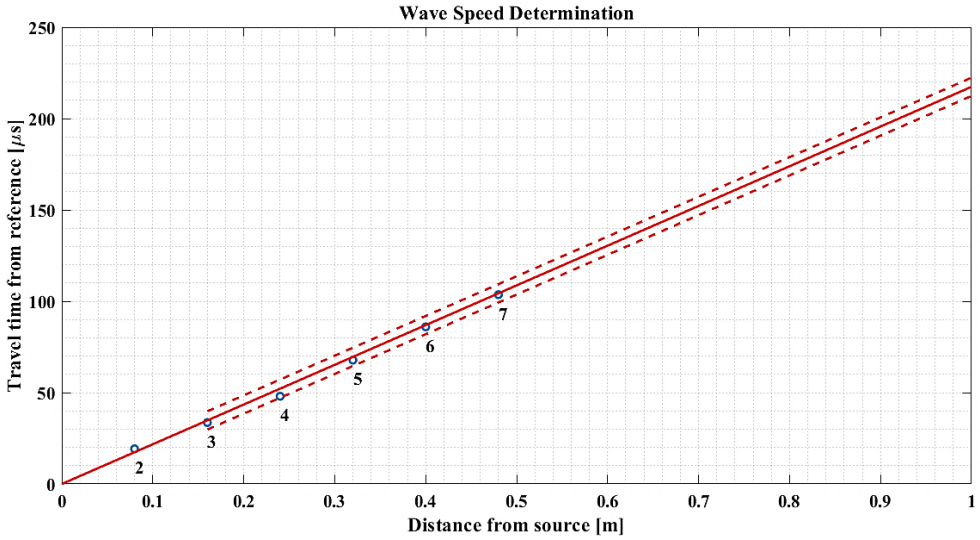

Figure 7.3: Wave Speed Determination (v= 4670 m/s)

Figure 7.4 shows the total attenuation plot for the baseline measurement. Two sets of measurements are shown here in the same plot. The first set represents the case when sensor 1 acts as the source (red markers) and in the second set sensor 7 acts as the source (blue marker). The y-axis value for both the cases is 1 at x=0.08 as it is the position of the reference sensor. A curve is fitted between the two sets of measurement to get an expression for total attenuation. The basic form of this expression is kept similar to equation 4, which is defined for a Rayleigh wave, and the constants are determined using curve fitting. The energy at sensor 3 for set 1 is considerably lower than the fitted curve, which can be a result of poor sensor coupling. The magnitude of error shows how sensitive the attenuation measurements are to the coupling between the sensor and the specimen. The material attenuation factor (α) is estimated to be 2.473 m^{-1}.

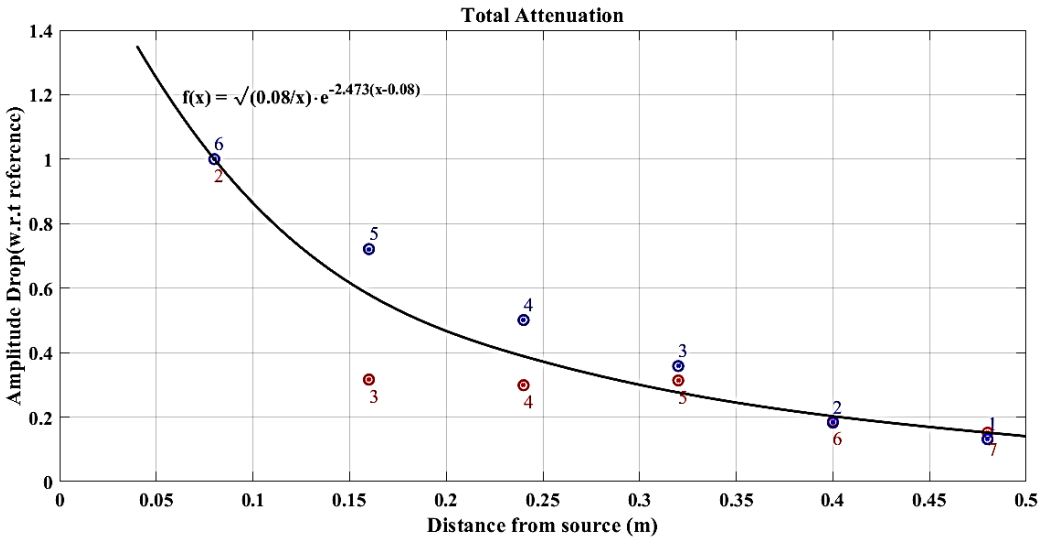

Figure 7.4: Amplitude Attenuation (total) in uncracked state

Using the curve fitting results from Figure 7.4, the amplitude drop due to propagation is obtained (Eqn 22), where x is the distance from the reference sensor.

$$\frac{A}{A_{ref}} = \sqrt{\frac{0.08}{x}} \cdot e^{-2.473(x-0.08)} \tag{22}$$

From this result the attenuation factor due to propagation for energy can be obtained using the following relation:

$$\frac{E}{E_{ref}} = \left(\frac{A}{A_{ref}} \right)^2 \tag{23}$$

7.2 Attenuation through cracks

7.2.1 Test setup

In the later stages of an experiment, when several cracks have already shown up, AE signals released due to formation of a new crack might have to travel through an existing crack before reaching the nearest sensor. In such case only a part the signal might get to pass through the crack, resulting in reduced energy estimation at the sensor location. Thus, the energy calculated at the sensor location needs to be corrected for this loss. Figure 7.5 shows the sensor geometry for HPZ03. It shows how the sensors are placed relative to each other. At the end of each loading step (in Figure 7.6), Auto-Sensor Test is performed. A reference state, as marked in Figure 32, is chosen which represents the AST measurements in the uncracked state. Then the AST results at other load levels are compared with AST at reference state to estimate the attenuation through a crack.

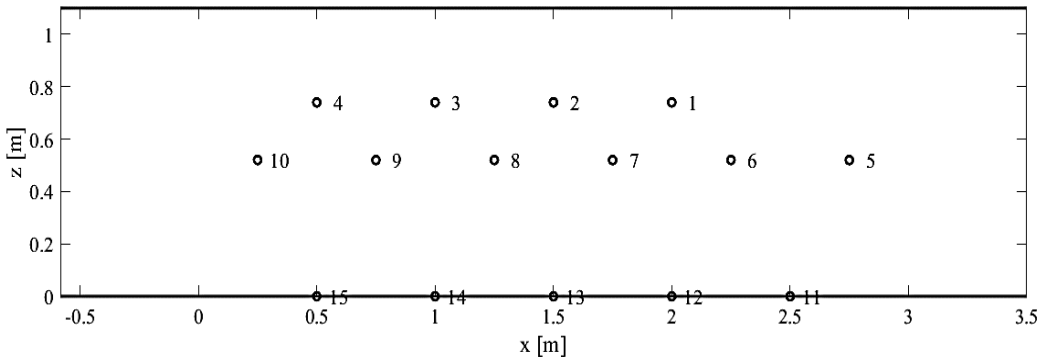

Figure 7.5: Sensor Geometry for HPZ03

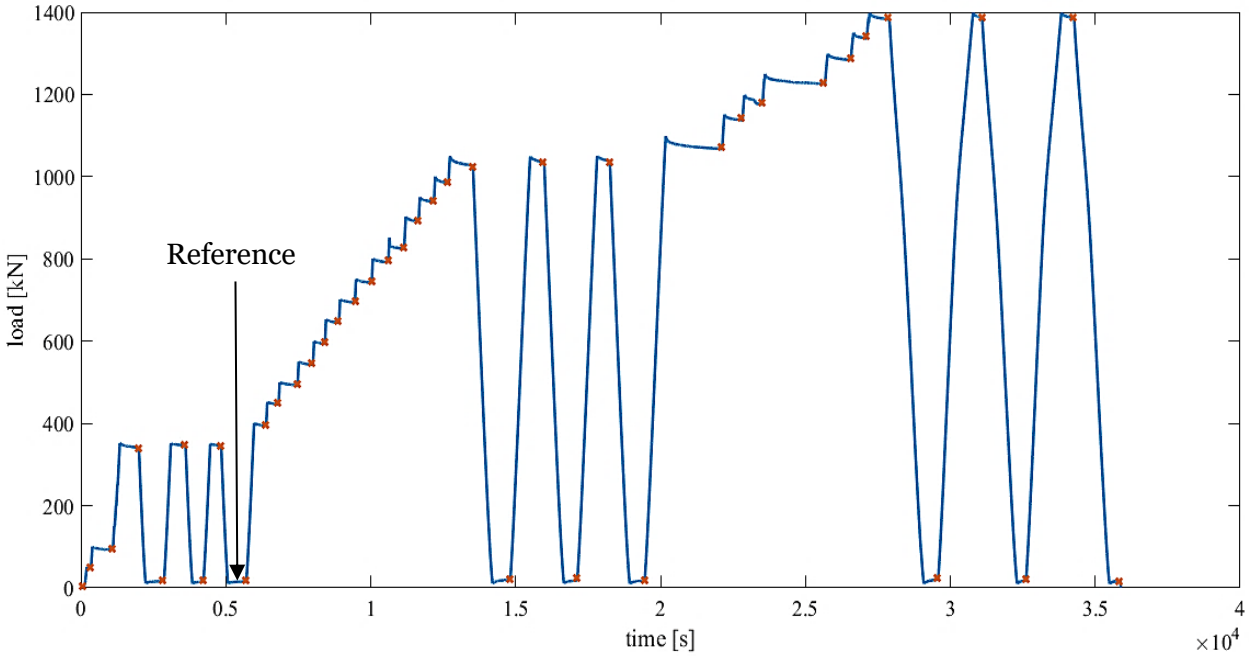

Figure 7.6: Loading Cycle HPZ03 with AST reference state

To estimate the energy attenuation through a crack, Crack attenuation factor (C.A.F) is introduced. C.A.F. is defined as:

$$C.A.F. = \frac{Energy_{reference} - Energy_{current\ \ load-level}}{Energy_{reference}} \tag{24}$$

For HPZ03, assuming the load level of 1050 kN, for any given pair of sensors from Figure 7.5 (taking sensor 11 and sensor 12 here), the C.A.F. is determined in the following manner. Firstly, taking the case when sensor 11 acts as a source and sensor 12 acts as a receiver during the AST. The energy of the AE signal received by sensor 12 is labelled as $Energy_{current\ load--level}$. Similarly, the energy of the AE signal received by sensor 12 for AST performed at the reference load-level (Figure 7.6) is labelled as $Energy_{reference}$. Now using the calculated values of energies, C.A.F. is determined. A positive value of C.A.F. means that energy has attenuated due to the presence of a new crack or due to change in strain w.r.t. reference state between sensor 11 and sensor 12. Similarly, the calculations can be made for the case when sensor 12 acts as a source and sensor 11 acts as a receiver. Both of these values are supposed to be the same, but they have minor differences. This point onwards all the values of C.A.F. for any sensor pair are the average of the two cases.

7.2.2 Results

C.A.F. for some of the sensor pairs for HPZ03 from 900kN to 1050kN is shown in Table 7.1. From the AE source localization result, it is known that the first flexure crack occurs at the load level 1000 kN between sensors 11 and 12. From Table 12 it is clear that C.A.F. increases as we move from 900 kN to 1050 kN, this happens as the strain between the two sensors increases and finally, a crack appears. On unloading both the factors become negative as the crack closes due to presence of prestressing. On reloading, for sensor pair 11-12, the factor increases from 0.9536 to 0.9679. This is because on reloading the crack propagates further thus the crack width at bottom increases causing further attenuation. For sensor pair 14-15 not much attenuation is observed as the sensor lies in the region which is far away from point of loading. The attenuation between this pair is the result of increasing strain at the bottom of the beam due to bending. For sensor pair 13-8 and 13-12, a high value of attenuation factor is observed which is not expected as per the experimental observations. A large value of C.A.F. is noted even for the unloading interval. From Figure 7.7, which represents the unloading interval, it is noted that all the attenuation lines connected to sensor 13 have a high value of attenuation, of nearly equal to 1. Red lines indicate a reduction in energy level and green lines indicate the increase between the sensors. A possible reason for this anomaly can be reduced coupling between the sensor and the beam surface during the experiment. This reasoning is further strengthened by the fact that after the second cycle of reloading sensor 13 receives no signal from sensor 7 or sensor 8. Therefore, results related to AE13 were not used. Although some other sensors also show high attenuation values, they continue to receive the signal even in later stages of loading.

Table 7.1: Crack Attenuation Factor(C.A.F.) for HPZ03

	Sensor Pairs			
Load-Level (kN)	**(13,8)**	**(13,12)**	**(11,12)**	**(14,15)**
900	0.8344	0.8421	0.6354	0.0538
950	0.8946	0.9127	0.817	0.0259
1000	0.9238	0.9482	0.9096	0.0645
1050	0.9449	0.9506	0.9536	0.1664
Unloading	0.9607	0.9625	-0.2598	-0.0256
Reloading	0.9936	0.9871	0.9679	0.2269

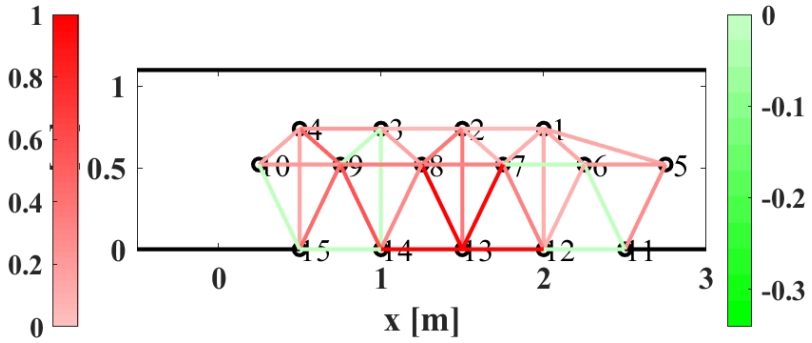

Figure 7.7: Attenuation Plot during unloading for HPZ03, including sensor 13

Table 7.2 shows the variation in C.A.F. value between different load levels. It is defined as:

$$\Delta C.A.F. = (C.A.F.)_{i+1} - (C.A.F.)_i$$

For sensor pair 11-12, the value of $\Delta C.A.F.$ increases two-folds at 900 kN. The value changes from 0.1231 to 0.2825. $\Delta C.A.F.$, predicts the occurrence of this crack 50 kN in advance compared to the source localization results. The growth in C.A.F. value with increasing load, between sensors 5 and 6, is shown in Figure 7.8 and the displacement between the two sensors is shown using the LVDT measurement. Sensor 5 and 6 are located at the bottom of the web (refer to Figure 7.5). It is noted that the attenuation factor and the lvdt displacement start to increase at around the same load level. The result shows the sensitivity of the C.A.F. and thus AST measurement to changes in strain within concrete.

For graphical representation, the attenuation results are shown in Figure 7.9, excluding AE13. The red lines indicate a decrease in energy value between the sensors and green lines represent an increase in energy. The line connecting sensor 11 to sensor 12 changes its colour from light red to dark red as the load increases due to the presence of a crack. On unloading the colour changes again from red to green, as the crack closes due to prestressing.

Table 7.2: Variation in C.A.F. for HPZ03

	Sensor Pairs			
Load-Level (kN)	**(13,8)**	**(13,12)**	**(11,12)**	**(14,15)**
850	0.0791	0.1073	0.1231	0.0621
900	0.1184	0.0286	0.2825	0.0423
950	0.0602	0.0706	0.1816	0.0514
1000	0.0292	0.0355	0.0926	0.0062
1050	0.0211	0.0024	0.044	0.027
Unloading	0.0158	0.0119	-1.2134	0.0395

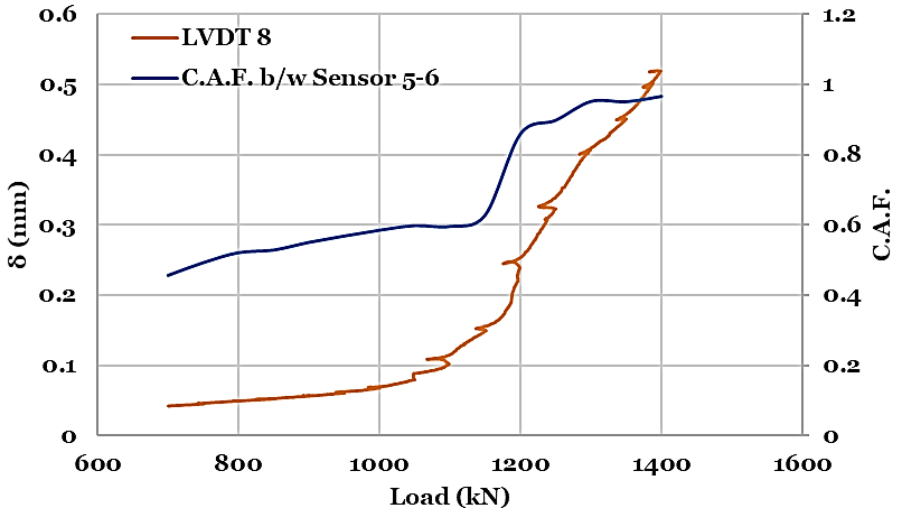

Figure 7.8: Variation in C.A.F. and LVDT with Load

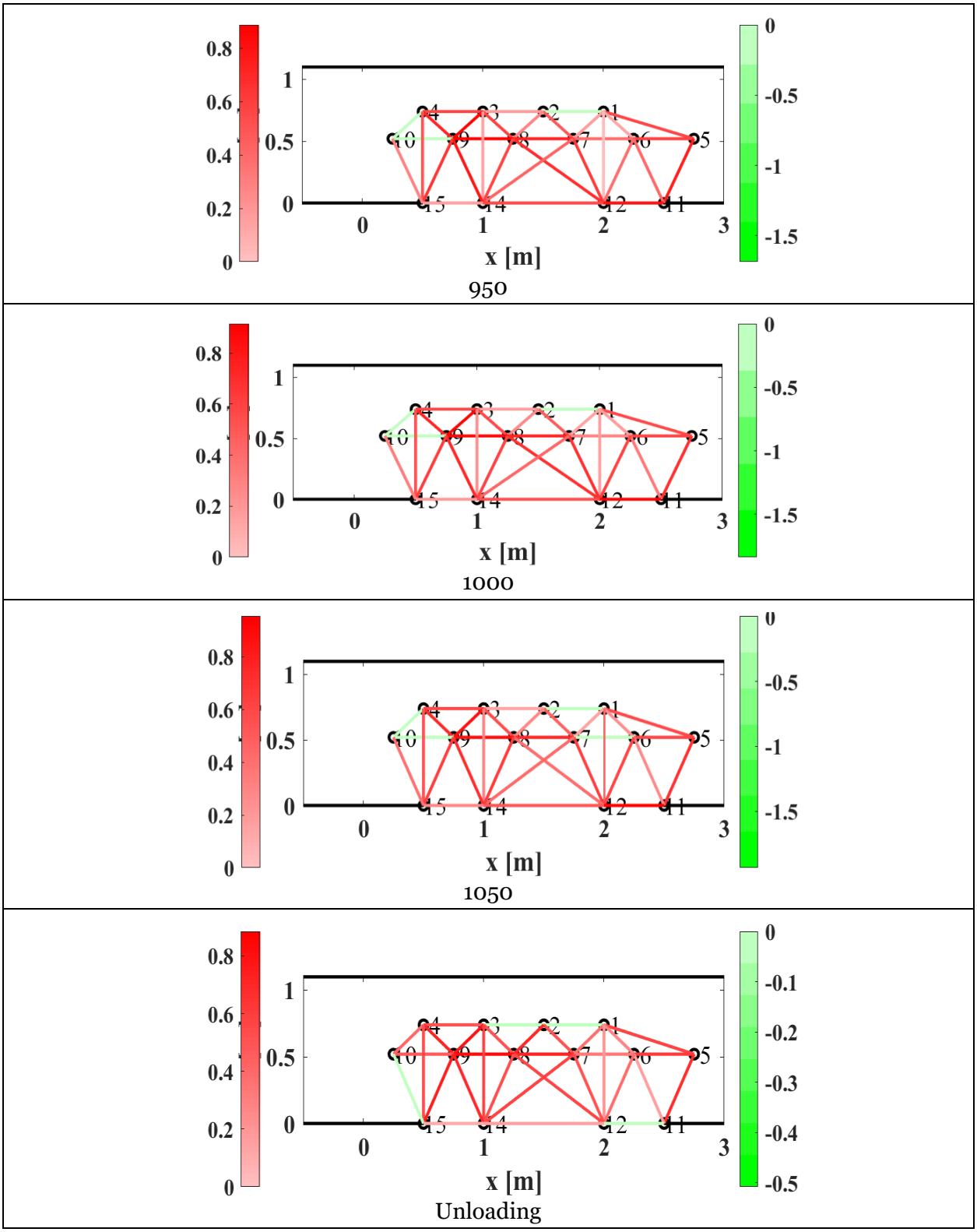

Figure 7.9: Total Attenuation in Energy for HPZ03, excluding sensor 13

7.3 Estimation of AE Energy Released at the Crack Location

Once an elastic wave is released due to an AE activity inside the concrete, the wave travels some distance before it reaches the sensor location. The energy at the sensor location is calculated by integrating the square of the voltage transients over time using Eqn (1). Now, to estimate the energy at the crack location the loss in energy due to propagation and crack is to be compensated.

The attenuation in energy due to crack propagation and due to presence of the crack is discussed in the previous sections and the following two factors were introduced, one the propagation attenuation factor (PAF), calculated using Eqn 23, and other the crack attenuation factor (CAF). Using these two factors the energy released at the crack location can be estimated. The energy at the AE event location can be estimated using the following relation:

$$Energy\ at\ Crack\ Location = Energy\ at\ Sensor\ Location / Net\ Attenuation\ Factor$$

where $Net\ Attenuation\ Factor = PAF \cdot (1 - CAF)$

In this thesis, the attenuation factors due to propagation only are considered to estimate the energy released at the crack location. This is because the crack attenuation factors estimated through AST measurements are inconsistent in nature.

7.4 Concluding Remarks

Attenuation measurements were performed in cracked as well as the uncracked state. Attenuation factors are proposed for both the cases which can be used to correct the energy released at crack location. Following conclusions can be made regarding the estimation of attenuation:

i. For attenuation in the uncracked state, the expression obtained from curve fitting of total attenuation can be used to correct the energy of propagation loss. A material attenuation factor of 2.473 m^{-1} is obtained.
ii. Auto-Sensor Tests (ASTs) prove useful in estimating the attenuation through a crack. The AST results, as observed from the CAF values, are more sensitive to strain changes in concrete than source localization results. For HPZ03, the cracking load was predicted 50 kN in advance.

8 Numerical Model

8.1 Model Description

Non-linear finite element analysis (NLFEA) is commonly used in engineering practice for examining the structural health of existing structures. The non-linear analysis helps in determining ultimate load capacity as well as checking requirements for serviceability state. In this thesis, non-linear finite element models for the girders obtained from the Helperzoom viaduct are modelled to examine the local crack energy release. For non-linear finite element analysis in this report, Diana 10.3 release 2019 is used.

Model behaviour is defined based on recommendations from RTD 1016-1:2017 [53]. A separate non-linear model was produced for each Helperzoom beam based on the load position and the current prestressing level as described in Chapter 4.

8.1.1 Model Geometry

AE monitoring for Helperzoom is conducted in a 2D plane, thus the numerical models are created in a two-dimensional setting using plane stress elements. This will help reduce the computational time and will provide an apt comparison between the AE results and the numerical results. The main span of the beam in the numerical model is 9600 mm and total length is half the Helperzoom girder length. Although the four Helperzoom beams are of different lengths as shown in Chapter 4, the non-linear models have the same length with the main span length same as the experiment.

A representative Helperzoom beam model is shown in Figure 8.1. Longitudinal reinforcements and stirrups are shown as blue lines and the prestressing tendons are shown using red lines. The model contains a horizontal restraint which is only applied while applying the prestressing. The support plates have a dimension of 560 mm x 100 mm and the loading plate has a dimension of 300 mm x 300 mm. Loading plate is placed either at a distance of 2903 mm or at a distance of 4400 mm from the support based on load position. Plates used for external prestressing are 100 mm long and have a thickness equal to the thickness of the beam. The applied vertical load is shown by a red arrow and the external prestressing applied to control the shear crack on one side of the beam is shown by green arrows.

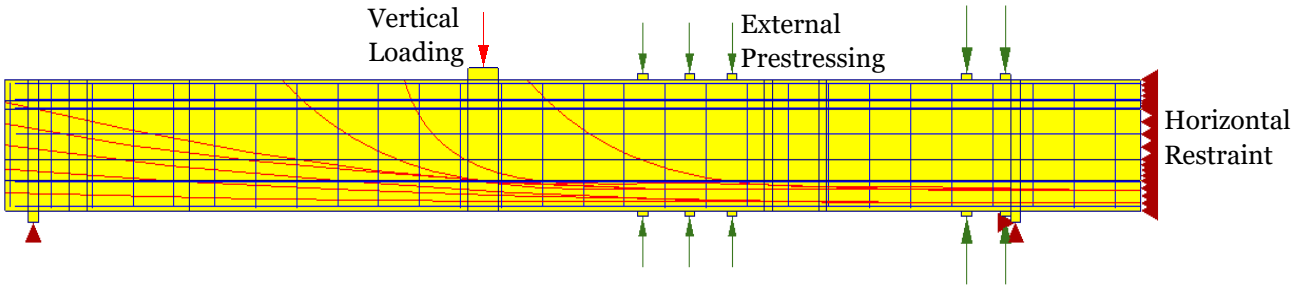

Figure 8.1: 2D non-linear model of Helperzoom for Numerical Analysis

The standard beam cross-section is T-shaped with some alterations along the length of the beam. These variations include the presence of an end block of 800 mm at one end and a transition zone of 1000 mm between the end block and the standard cross-section. In addition to this, parts of cross-beam are also attached to the main girder at a distance of 7450 mm from the support.

Although the model is created in a 2D environment, beam cross-section is defined using a spatial function which allows the thickness to vary across the depth. Figure 8.2 shows the thickness function of the standard cross-section as it is defined in Diana. A factor of 1.0 represents a thickness of 1000 mm.

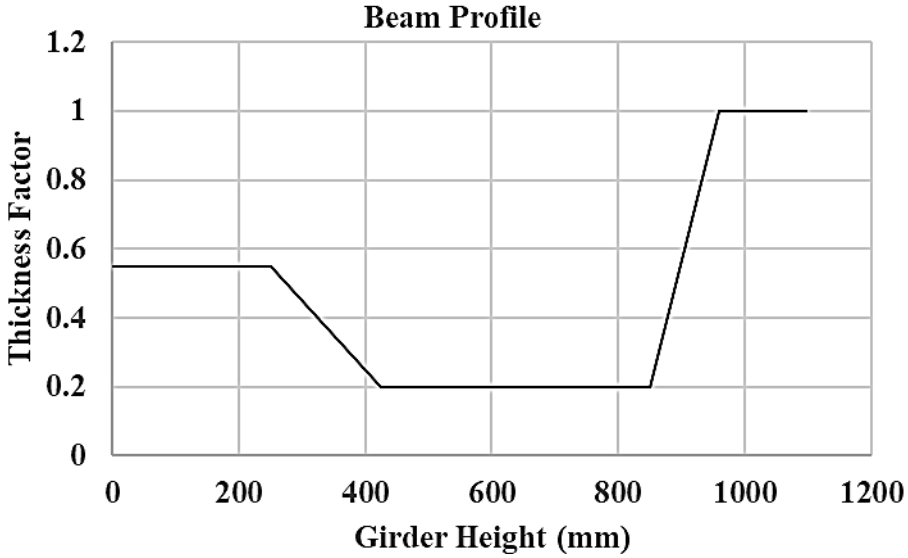

Figure 8.2: Standard Cross-Section Function

8.1.2 Material Description

Definition of material behaviour is an important aspect of non-linear modelling. In addition to this, concrete heterogeneity adds further complexity to the material definition. In this thesis, the behaviour of concrete in tension and compression is described by different constitutive relations, defined as per the RTD guidelines [53]. A total strain-based crack model is used to model the concrete non-linearity. The non-linear behaviour of prestressing tendon and reinforcement is modelled to include plasticity. Mean values for material properties are used because the comparison is made with the experimental results.

Concrete

The smeared cracking approach is used to model concrete behaviour in tension. As per the smeared approach for crack modelling, the crack is assumed to be smeared over the element following the relation between stress and crack strain. This relationship is governed by concrete tensile fracture energy and crack bandwidth. In this thesis, Hordijk tension softening curve as proposed in [54] is used. The concrete has a mean tensile strength of 5.4 MPa. The stress-strain relation used in Diana is shown in Figure 8.3 with an assumed crack bandwidth of 100 mm. The modelled curve can be different as crack bandwidth in this thesis is calculated using the Rots model.

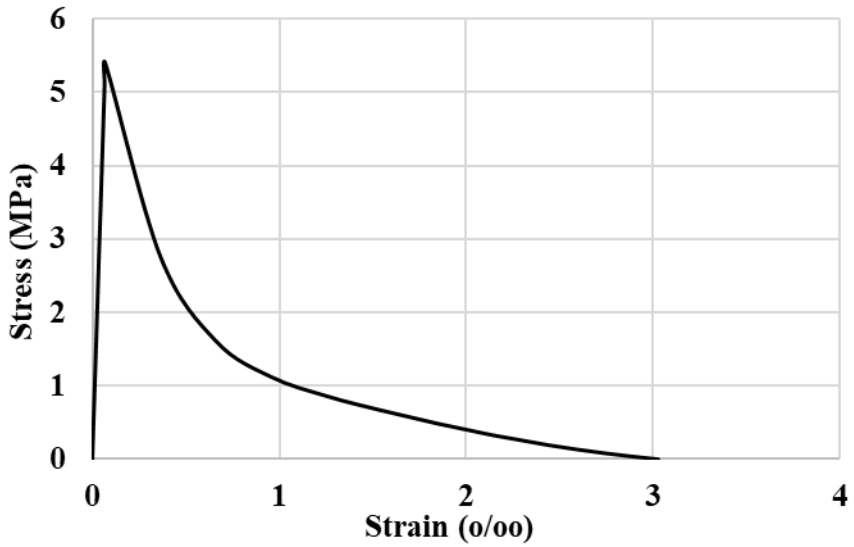

Figure 8.3: Hordijk Tension Softening Curve

Similarly, to model concrete behaviour in compression, parabolic compression model is used. The parabolic model for compression provides a realistic behaviour in compression as suggested in the RTD guidelines [53]. Mean compressive strength of 76.3 MPa is used for girder concrete. The stress-strain relation defining compression behaviour is shown in Figure 8.4. Detailed concrete material properties and associated inputs are provided in Table 8.1

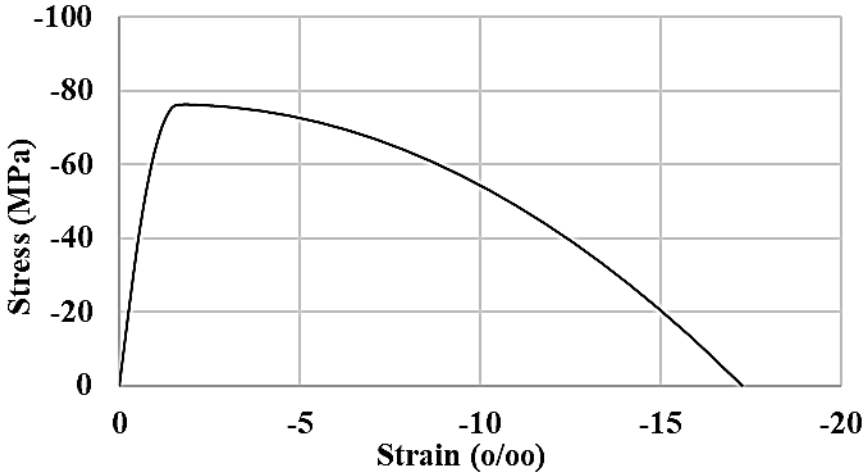

Figure 8.4: Parabolic Compression Curve

Table 8.1: Concrete Properties in Diana

Property	Value
Material Class	Concrete and Masonry
Material Model	Total Strain Crack Model
Young's Modulus	39548 MPa
Poisson Ratio, ν	0.15
Mass Density	2500 kg/m^3
Crack Orientation	Rotating
Tensile Curve	Hordijk
Tensile Strength, f_{ct}	5.4 MPa
Mode-I tensile fracture energy, G_f	0.159 N/mm
Crack Bandwidth	Rots
Compressive Curve	Parabolic
Compressive Strength, f_c	76.3 MPa
Compressive Fracture Energy	39.75 N/mm
Reduction Model	Vecchio and Collins
Lower Bound Reduction Curve	0.4
Confinement Model	Selby and Vecchio

Prestressing Steel and Reinforcement

The prestressing tendons and steel reinforcements are modelled to show isotropic strain hardening. All the reinforcements are modelled as embedded reinforcements, which means that the rebars are fully bonded to the mother elements. The elastic modulus for prestressing steel is 185000 MPa and for reinforcement, it is 200000 MPa. The modelled behaviour of both materials is shown in Figure 8.5. The prestressing steel has a yielding strength of 1433 MPa and fracture strength of 1870 MPa and the reinforcement has a yielding strength of 440 MPa and fracture strength of 530 MPa. Summary of choices made for modelling reinforcement and prestressing steel is shown in Table 8.2. The details regarding material properties can be obtained from the measurement report for Helperzoom beams.

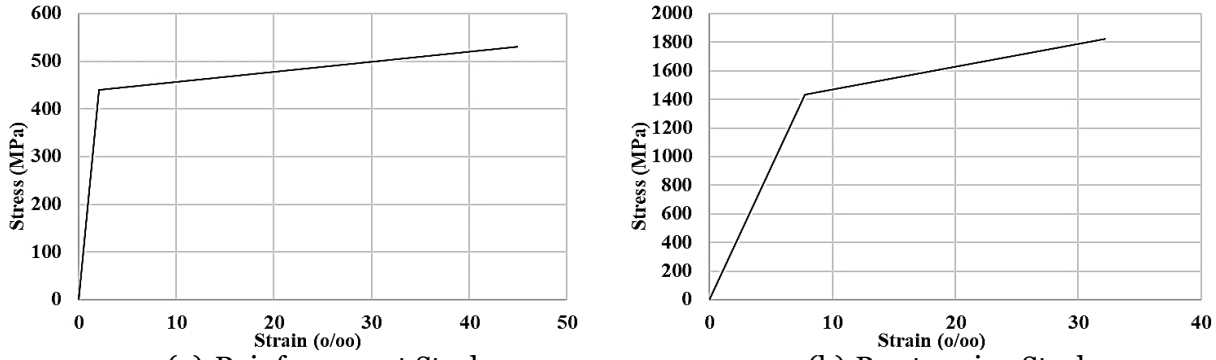

(a) Reinforcement Steel (b) Prestressing Steel

Figure 8.5: Reinforcement and Prestressing Steel Material Model

Table 8.2: Reinforcement and Prestressing Material Model

Property	Prestressing Steel	Reinforcement Steel
Youngs Modulus	185 GPa	200 GPa
Plasticity Model	Von Mises Plasticity	
Plastic Hardening	Plastic Strain Yield Stress	
Hardening Hypothesis	Strain Hardening	
Hardening Type	Isotropic Hardening	
Bond Type	Embedded	
Yield Strength	1433 MPa	440 MPa
Ultimate Strength	1870 MPa	530 MPa

8.1.3 Loads

Prestressing Load

The Helperzoom girder is prestressed using 10 tendons, modelled as embedded reinforcements. The tendons are loaded using reinforcement bar prestress option in DIANA which allows in applying a uniform prestress in rebar throughout the length. The prestressing load is applied based on the value estimated in the analysis report for Helperzoom using sectional analysis [50]. Table 8.3 shows the estimated prestress levels for all the four beams.

Table 8.3: Calculated Prestressing Level

Beam Nr.	Prestressing Level (MPa)
HPZ01	695
HPZ02	725
HPZ03	700
HPZ04	780

Transverse Prestressing

AE acquisition setup is installed over a part of the beam, thus for better insight into failure, the final shear tension cracks must occur in this part. To ensure this transverse prestressing is applied on the part of the beam where the shear tension crack must be avoided or controlled. The applied external prestressing depends on a case-to-case basis. For HPz01 150 kN prestressing, two at each position is applied at 2070, 2190, 2300, 2930 and 3100 mm from the end. For Hpz02 100kN prestressing, two at each position is applied at 730, 1510, 1880, 2180 and 3530 mm from the end. The applied external prestressing with its location for HPZ03 and HPZ04 is shown in Table 8.4 and Table 8.5 respectively.

Table 8.4: External Prestressing for HPZ03

Prestressing Load (kN)	Distance from end (mm)
200	2490
200	2880
150	5175
150	6050
150	5590

Table 8.5: External Prestressing for HPZ04

Prestressing Load (kN)	Distance from end (mm)
50	730
50	1280
50	1810
50	2470
150	4510

Applied Load

The load is applied at a distance of 2900 mm (HPZ01, HPZ02) and 4400 mm (HPZ03, HPZ04) from the left support. A force-controlled loading method is adopted which follows the experimental loading scheme discussed in Chapter 4.6. The point of application of load is shown in Figure 8.6. In addition to this, deadweight is also applied to the finite element model.

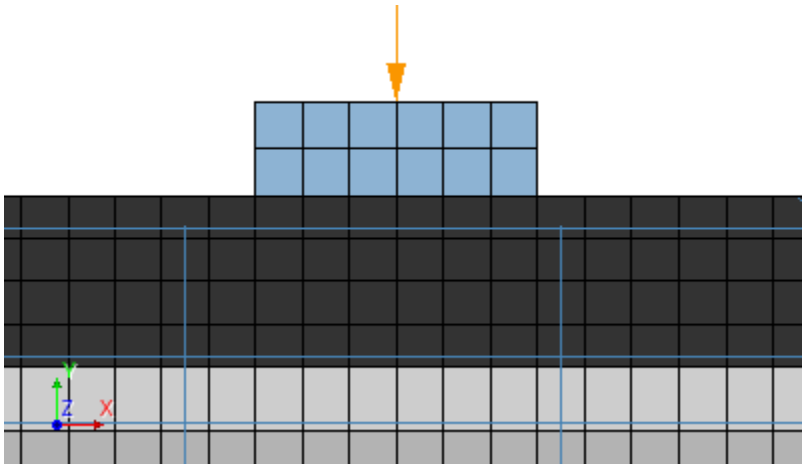

Figure 8.6: Applied Vertical Load

8.1.4 Support and Restraints

Linearly elastic support plates of elastic modulus 210000 MPa are used at the support and loading points as shown in Figure 8.1. At the left support plate, the restraint is provided in the vertical direction and at the right support plate, the restraint is provided in the horizontal as well as vertical direction. The right support remains inactive when prestressing is applied. In addition to this horizontal restraint is also provided at the right end of the beam. This horizontal restraint remains active only during the prestressing and becomes inactive thereafter.

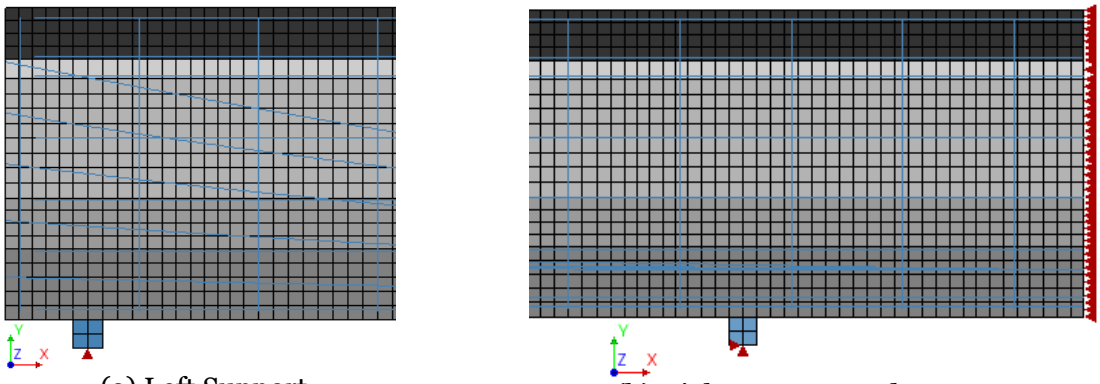

(a) Left Support (b) Right Support and Symmetry

Figure 8.7: Support Condition

8.1.5 Meshing

Diana provides a wide range of structural elements to choose for structural analysis. Regular plane stress CQ16M elements are used to generate the beam mesh. The element used is shown in Figure 3.1. CQ16M is an eight-node quadrilateral isoparametric plane stress element which uses quadratic interpolation and Gauss integration. It has 2 degrees of freedom per node. By default, a 2x2 integration scheme is used to yield optimal stress points.

8.1.6 Analysis Method

The Helperzoom beam is prestressed and a vertical load is applied during the experiment, therefore phased analysis is used. In the first phase, the prestressing and deadweight of the beam are applied simultaneously using 5 load steps and the right vertical support is switched off. Once the prestressing is applied, the right support is switched on and the horizontal restraint at the end is switched off. Then the load is applied on the beam following the experimental loading profile. An extra load step is introduced after the prestressing and before applying the vertical load. In this step the transverse external prestressing on the far side of the beam is applied. The support conditions during external prestressing are the same as that during the vertical loading. An energy norm with a tolerance of 0.001 is used in all the analysis. Regular Newton-Raphson iterative method with a maximum of 250 iterations is used to obtain the solution.

8.2 Verification of the Numerical Model

Figure 8.8 shows the load-displacement plots for all the four Helperzoom beams. HPZ01 and HPZ02 behave similarly till the point of first crack, thereafter the behaviour starts to change due to difference in prestressing levels. Similarly, HPZ03 and HPZ04 show a similar behaviour before the first flexure crack and then a change can be seen thereafter. The initial stiffness of the numerical model is a bit higher than the stiffness from the experiment.

Table 8.6 shows the load level at which the first flexure crack is observed in the numerical model and the experiment. For HPZ03 and HPZ04 the first crack in the numerical model is reported at 1050 kN and 1150 kN respectively. This is the same load level at which the crack was reported to occur experimentally. For HPZ01 and HPZ02 the crack in the numerical model is reported with a delay of around 50kN. A possible explanation for the lower cracking load observed in the test can be the variability in the tensile strength. The results show that the numerical model captures the occurrence of the flexure crack well.

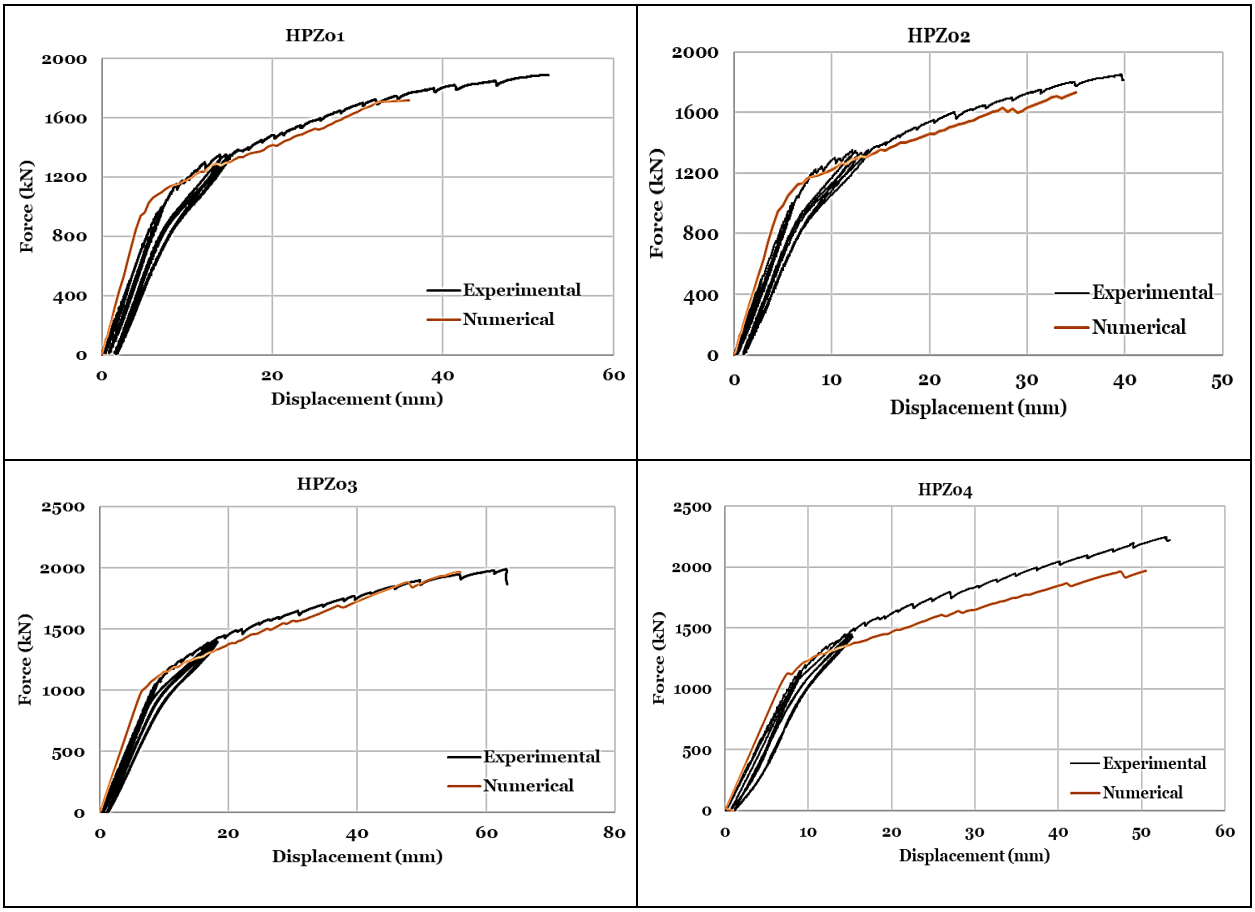

Figure 8.8: Load Displacement Plots for Helperzoom Beams

Table 8.6: Load Level at First Flexure Crack

Beam Nr.	Flexure Crack	
	Numerical Model	Experiment
HPZ01	1000 kN	965 kN
HPZ02	1050 kN	1000 kN
HPZ03	1050 kN	1050 kN
HPZ04	1150 kN	1150 kN

The result from the numerical model is used to compare to the cracking pattern in the experiment. The cracking pattern at failure is shown in Figure 8.9 for HPZ02 prestressing and in Figure 8.10 for HPZ04. These cracking patterns correspond well to what is observed in the experiment, see Figure 8.11.

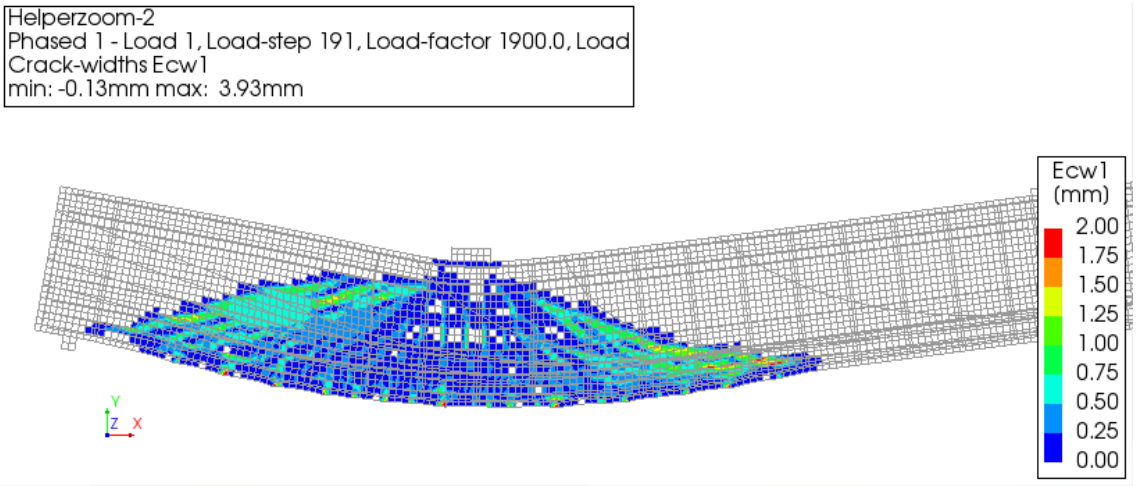

Figure 8.9: Crack Pattern at Failure for HPZ02

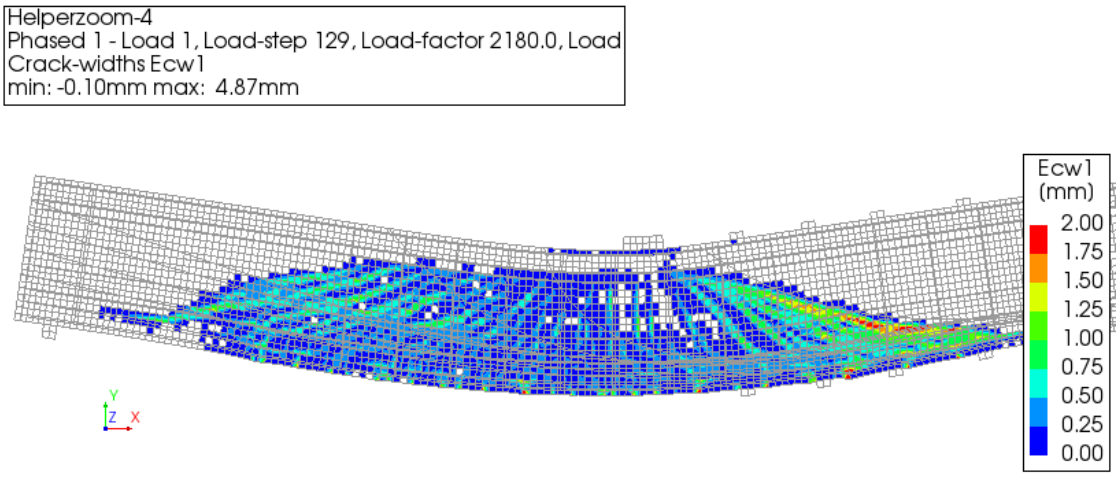

Figure 8.10: Crack Pattern at Failure for HPZ04

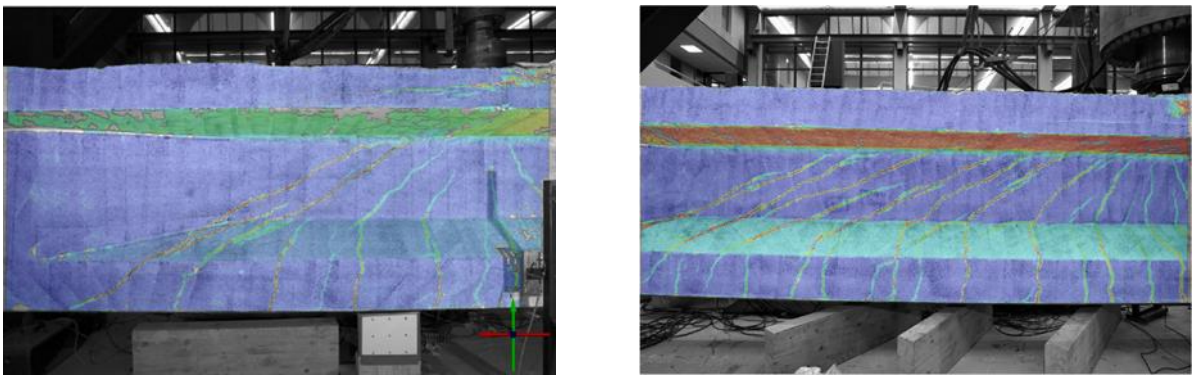

HPZ02 HPZ04

Figure 8.11: Experimental Crack Pattern at Failure

8.3 Local Energy Release in Numerical Model

The energy released locally in the numerical model is compared with the DIC measurements made during the experiment. Energy released locally in the numerical models is calculated using the methodology discussed in Chapter 3. Also, the energy is only calculated in the zone in which AE sensors are placed to have a comparison later between in the two.

The first crack in the HPZ03 beam model occurs at 1050 kN, which is same as the load level when the first flexure crack was observed during the experiment. Figure 8.12 shows the calculated local energy release for beam HPZ03 at 1050 kN along with the DIC measurement at the same load level. The energy release is plotted in a form of grayscale with each grid representing elements from the numerical model. AE sensors numbered 1-15 are also included in the plot area. The x-axis shows the distance from the end of the beam and y-axis denotes the beam height. The first crack occurs near sensor 11, which is around the same location as from DIC measurements. At 1400 kN, for HPZ03, 4 cracks, CR1 to CR4, are marked in the DIC measurement shown in Figure 8.13. The same four cracks are identified using the local energy plot also marked CR1 to CR4. A similar result is obtained for HPZ04, as shown in Figure 8.14, at 1450 kN. Three cracks are marked, numbered CR1 to Cr3, in the DIC result as well as numerical energy plot.

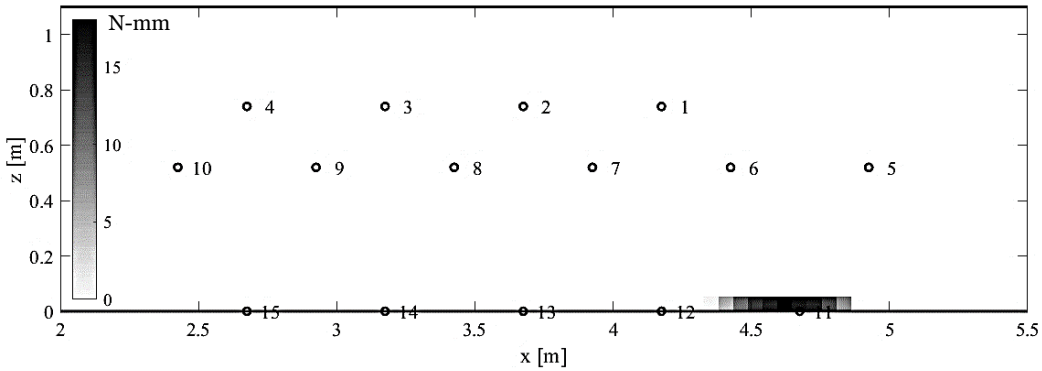

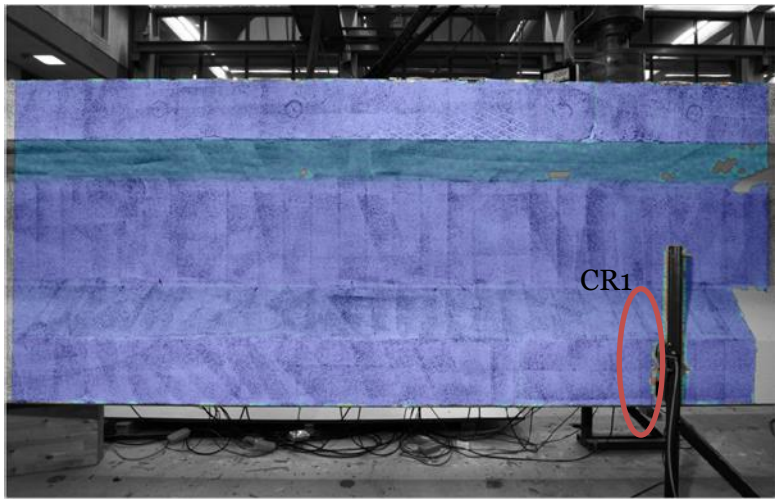

Figure 8.12: Local Energy Released for HPZ03 (1050 kN)

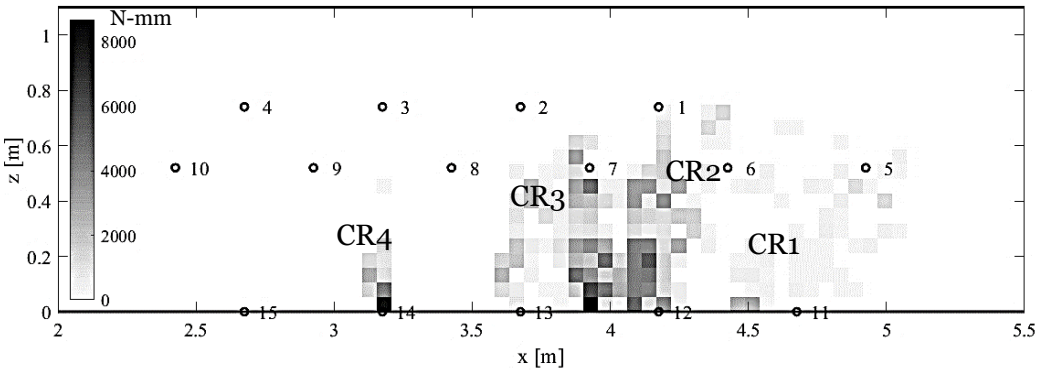

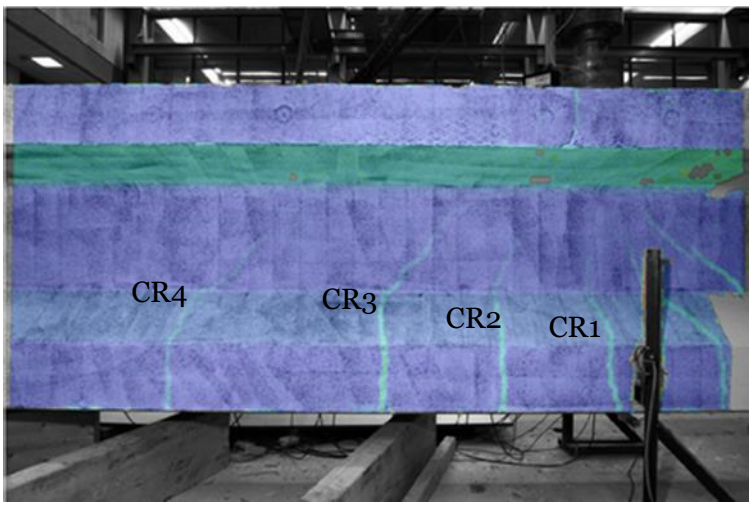

Figure 8.13: : Local Energy Released for HPZ03 (1400 kN)

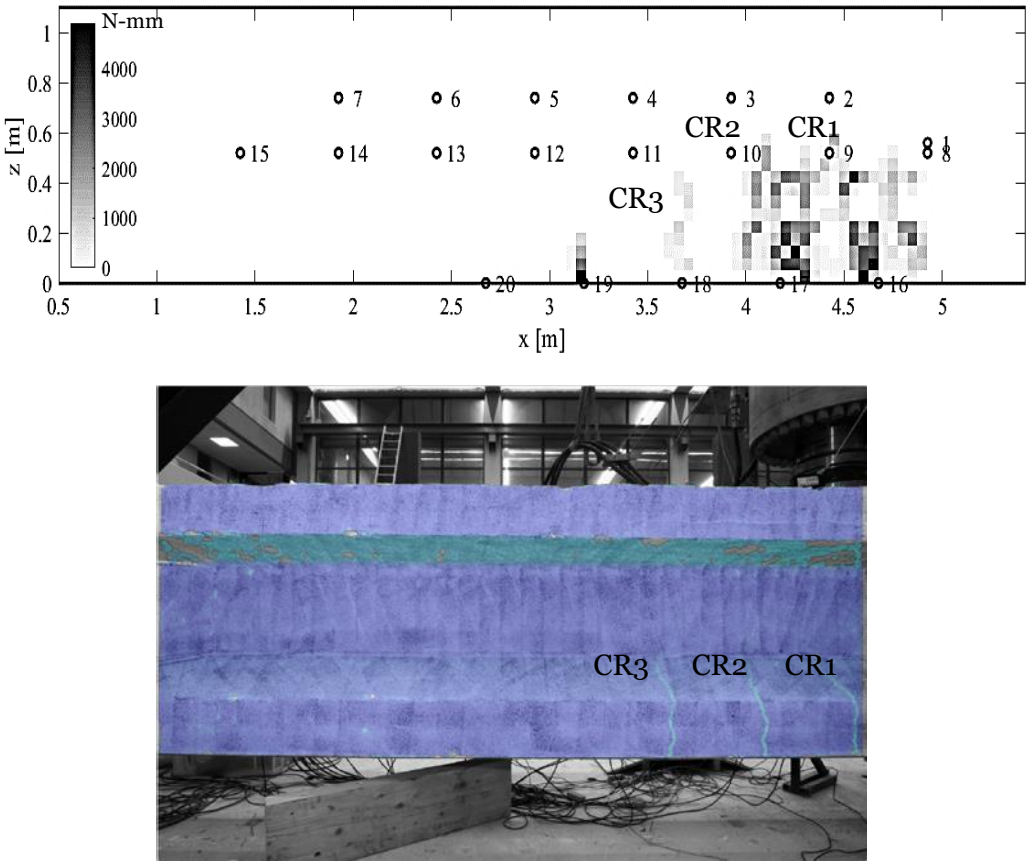

Figure 8.14: Local Energy Released for HPZ04 (1450 kN)

9 Comparison between AE and Numerical Energy

In this section, the computed local energy release from the numerical model is compared to the released AE energy. To perform this comparison the beam area under consideration is divided into certain zones. Figure 9.1 shows the zone division for beam HPZ03. The x-axis values are the distance from the beam end and y-axis values show the beam elevation. Over the height, the beam is divided into three levels with the centre of each level at 0.13 m, 0.39 m and 0.63 m. The first level at 0.13 m denotes the flange, the second level denotes part-flange and part-web, and the third level denotes web only. Along the length, the beam has 5 levels centred at 2.675 m, 3.175 m, 3.675 m, 4.175 m and 4.675 m. Similarly, the selected zones for beams HPZ02 and HPZ04 is shown in Figure 9.2 and Figure 9.3 respectively. Black arrows indicate the center of the loading jack.

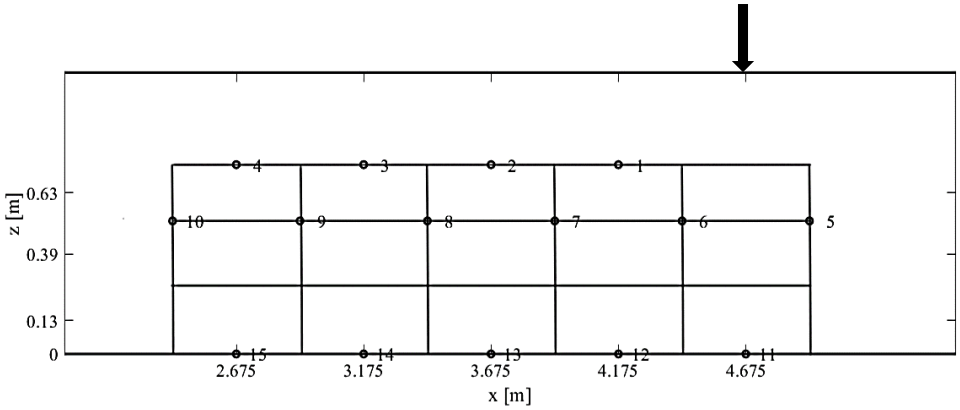

Figure 9.1: Zone Division for HPZ03

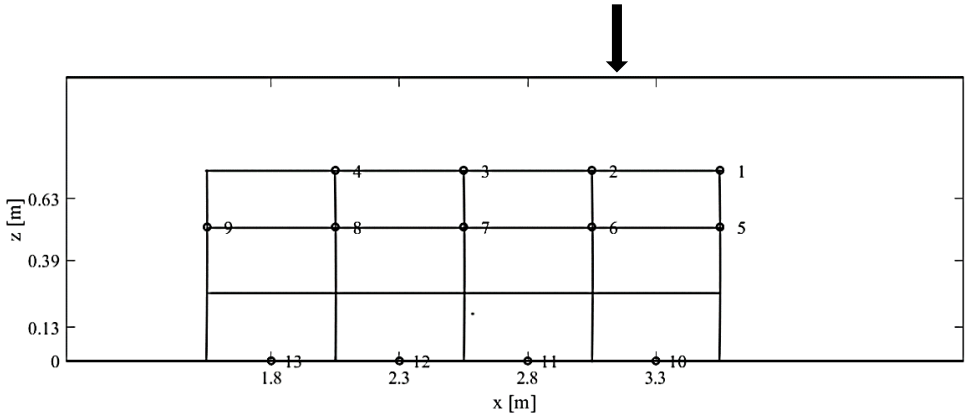

Figure 9.2: Zone Division for HPZ02

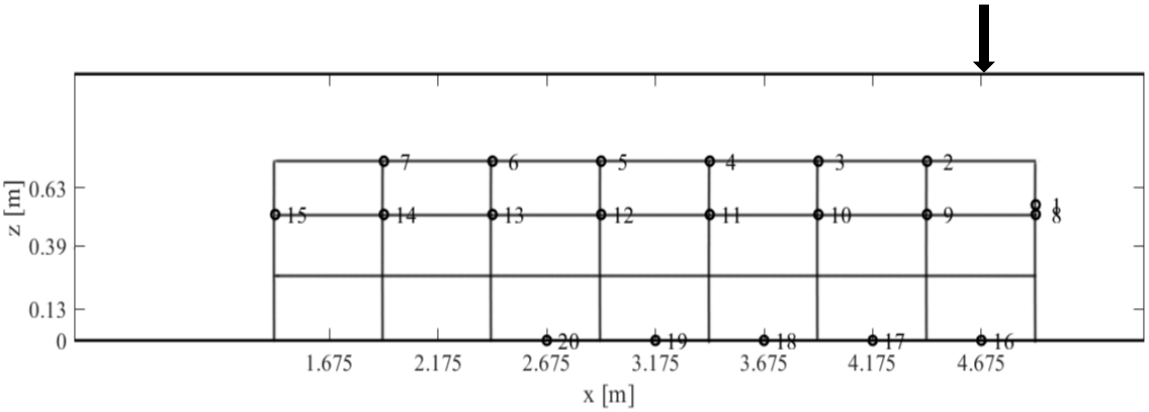

Figure 9.3: Zone Division for HPZ04

9.1 Energy Release along the Flexure Crack

Energy release along the crack length is tracked by selecting a flexure crack and following the path of the crack. As the cracks in the numerical model are smeared over an area, instead of following one crack, a flexure zone is identified, and the total energy released in the flexure zone is compared. The flexure zones identified for all the four beams are shown in Figure 9.4, marked as green regions.

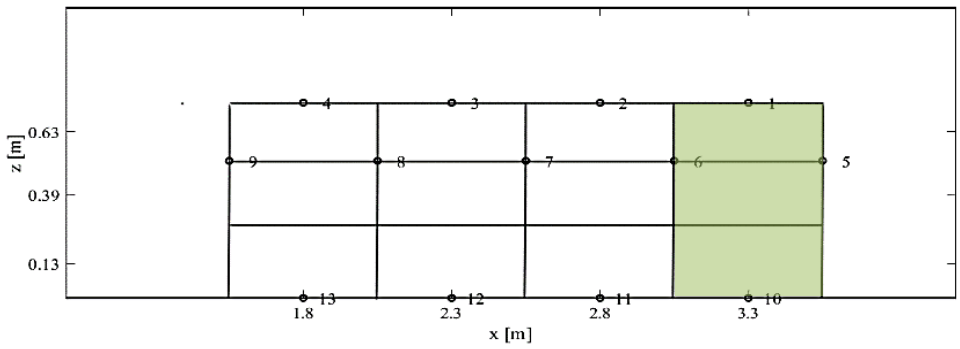

HPZ01

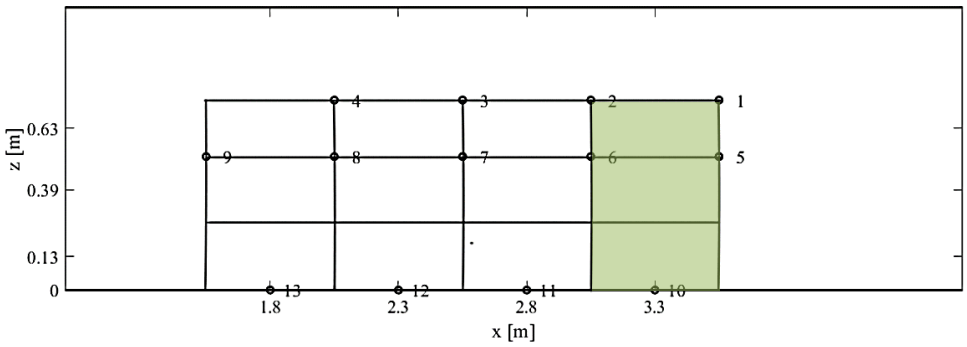

HPZ02

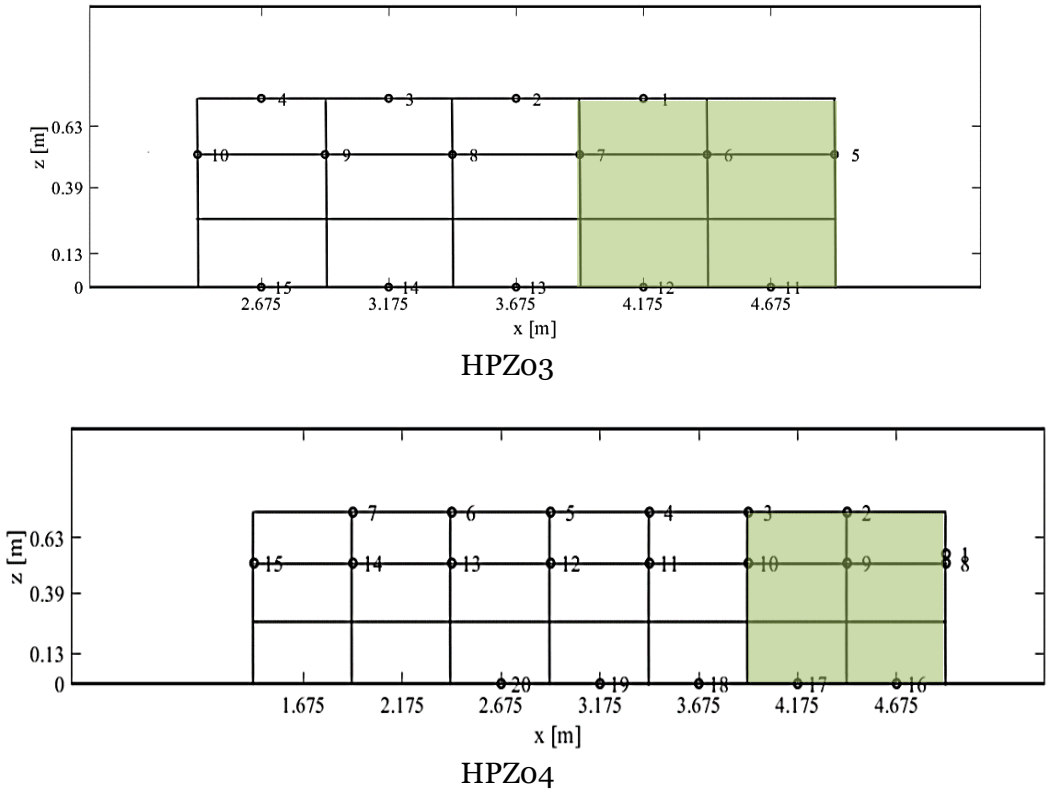

Figure 9.4: Identified Flexure Zones in the Four Beams

Total AE energy and numerical energy accumulated in the flexure zones for HPZ04 is shown in Figure 9.6. With increasing load, in the initial stages of loading, the rate of accumulated energy increases till a certain load level. This rate increase is the result of newer cracks being formed in the flexure zone. At 1200 kN only one flexure crack is present in the beam but at 1400 kN three such cracks can be identified. After 1400 kN the rate of energy accumulated remains constant and a steep increase in value is reported until 1450 kN. After this point, the rate of energy accumulation decreases as the crack tip does not propagate further into the beam as the top flange is under compression. Accumulated AE energy follows a similar trend with the change in load level.

A similar trend in cumulative AE energy and numerical energy is also observed for the flexure zones from HPZ02 and HPZ03, shown in Figure 9.6 and Figure 9.7 respectively. The total energy accumulated first increases gradually, then a steep rise in energy level is recorded followed by saturation in accumulated energy.

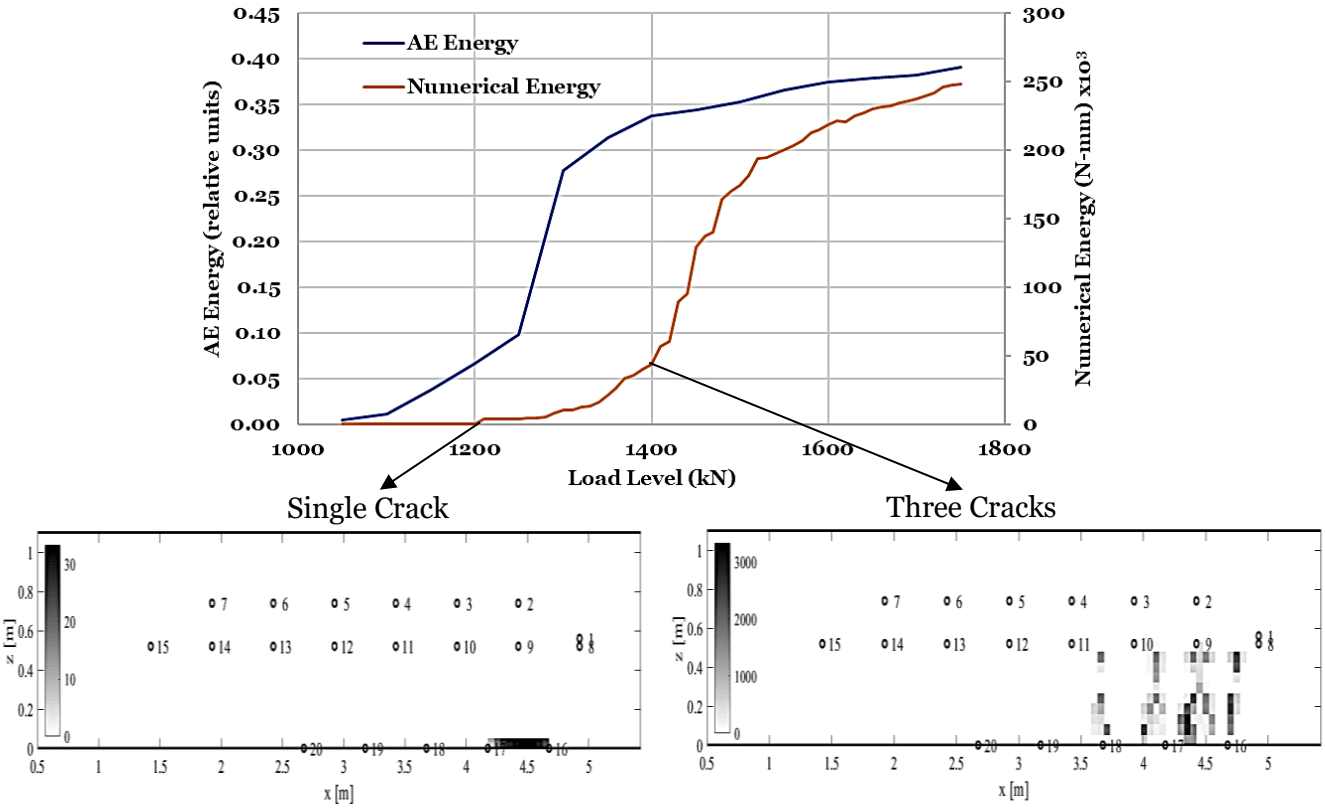

Figure 9.5: Cumulative AE Energy vs Numerical Energy in the flexure zone for HPZ04

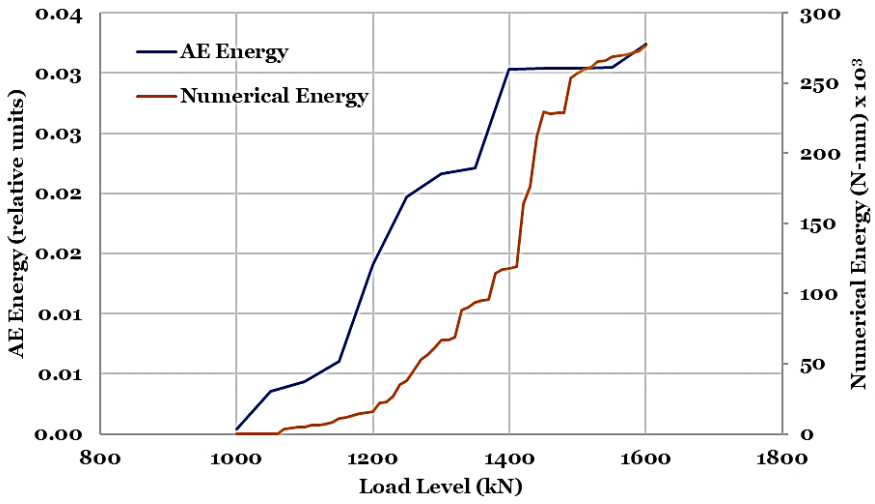

Figure 9.6: Cumulative AE Energy vs Numerical Energy in the flexure zone for HPZ02

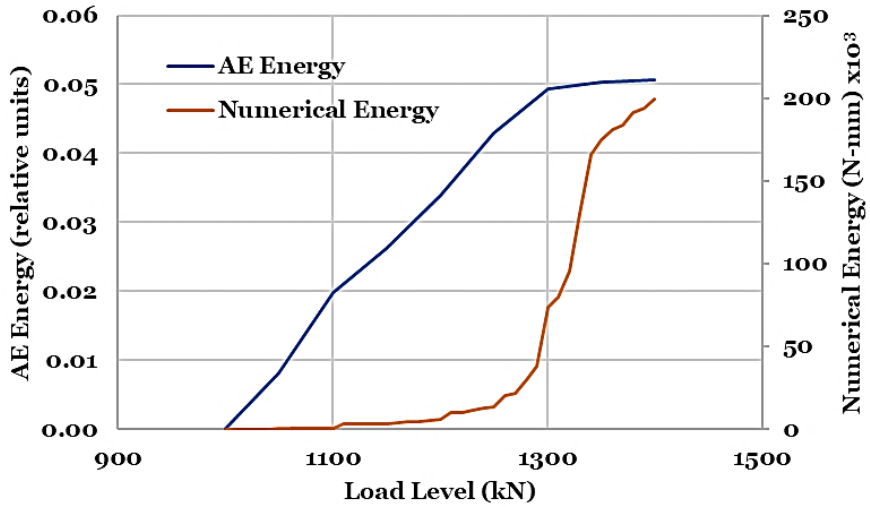

Figure 9.7: Cumulative AE Energy vs Numerical Energy in the flexure zone for HPZ03

The point of occurrence of first flexure crack using AE energy precedes the point of occurrence of first flexure crack using numerical energy. For HPZ04 (Figure 9.5), as per AE energy, the first crack occurs at 1050 kN and the same crack as per the numerical results occurs at 1200 kN. Thus, there is a difference of 150 kN between the values. For HPZ02 and HPZ03 the difference in load level in the point of occurrence of the first crack is 50 kN and 100 kN respectively. On an average AE energy predicts the crack 10% of the cracking load in advance. The reason that AE energy predicts the occurrence of the crack can be the higher variability in tensile strength of the concrete. Another possible reason can be that before a crack occurs in the concrete, in the area around the crack tip several microcracks occur, thus releasing energy in the form of stress waves. This microcracking behaviour is not captured by the concrete material property defined in the numerical model through the Hordijk curve.

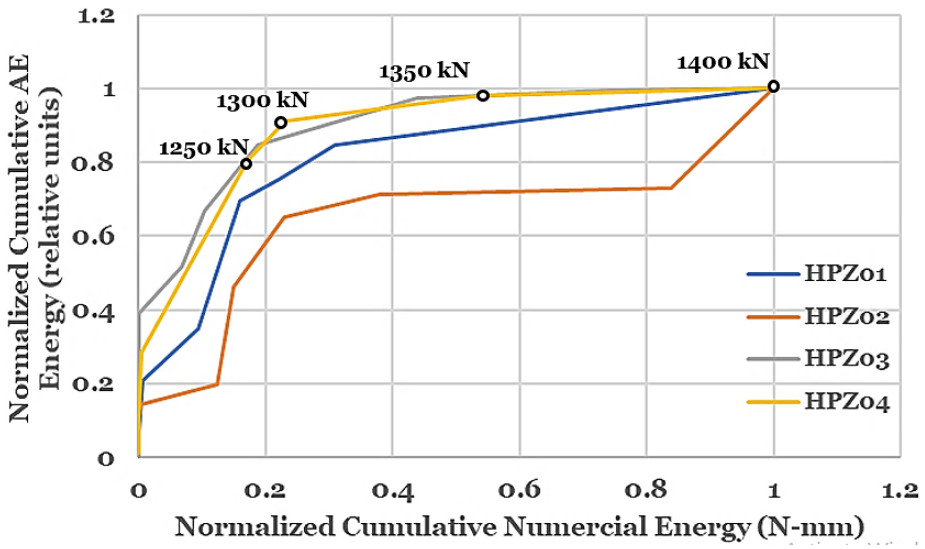

Figure 9.8: Relationship between Cumulative AE Energy and Numerical Energy

Relationship between the cumulative AE energy and cumulative numerical energy is shown in Figure 9.8 for all the four beams. The values are normalized with respect to the maximum for each beam. The plot considers only the energy released in the flexure zone until the load level when the

first shear crack was observed experimentally. The load levels are shown for beam HPZ04 to give an idea about how the energies accumulate through the load-levels. Initially, when the first flexure crack occurs, a spike in AE energy is seen. A possible explanation for this is that AE energy can predict the occurrence of a crack in advance. As the load is further increased the numerical energy also starts to accumulate. After around 40% of the maximum numerical energy, no significant increase in AE energy was observed. The observed relationship between AE energy and numerical energy was found to be non-linear. The nonlinear relationship is the result of the difference in the behaviour of AE activity and the numerical model. In the numerical model, following the Hordijk curve (Figure 8.3), the energy starts to accumulate when the strain reaches the tensile strength. In Figure 8.3, the strain at onset of crack is 0.07 ‰, but the softening branch goes till 3 ‰. Thus, a major percentage of energy is accumulated long after the crack has initiated. Whereas, the AE energy release occurs in majority when the crack is formed, and a relatively lower energy is released during the propagation stage.

9.2 Zonal Comparison

Following the zonal division of the beams at the start of this chapter, the energy release over the loading intervals is tracked. Before plotting the AE energy and the numerical energy together, the correction was applied to the numerical results to match the load at which the flexure crack was observed. So, following the results from Figure 9.7 and Figure 9.5, a correction of 100 kN and 150 kN is applied to HPZ03 and HPZ04. Figure 9.9 and Figure 9.10, shows the bar plot for energy calculated using AE and numerical model for HPZ03 and HPZ04 respectively, plotted side by side. The plots are shown at different load intervals to cover the loads at which the flexure cracks and the loads at which the shear cracks are observed. The x-axis in the bar plot shows the location of the zone centre from the edge of the beam and over the y-axis, the plot consists of three levels representing the zones at those three levels. The energy levels indicated here represent the energy accumulated within that load-interval only.

For HPZ04, from 1150 kN to 1250 kN, the peak energy release is observed at x= 4.675 m and y= 0.13 m (the bottom right part of the bar plot). This is the bottom side of the beam where the first flexure crack was observed from the numerical results as well as DIC results. As the load level increases, the crack propagates further into the web and new cracks are created to the left of this existing crack (shown in Figure 8.14). This can also be seen from the energy plots for both AE energy and numerical energy as the peak bar moves upwards and towards the left as the load increases. A similar pattern is observed in the case on HPZ03 and HPZ02 in Figure 9.10 and Figure 9.11 respectively. Results for HPZ01 are attached in Appendix B.

Overall a good relation is observed between the AE energy and the numerical energy. A relatively better comparison is observed in the first two load intervals for both HPZ03 and HPZ04, although for the third interval the deviations are more visible. The first two intervals represent the intervals in which the flexure cracks are created, and they propagate into the web. The third interval for all the beams marks the occurrence of the shear crack. Numerical energy follows a similar trend as the AE energy when the cracks occur in the flexure zone, but the numerical model is unable to exhibit similar behaviour in the shear zone. HPZ02 shows a similar pattern in Figure 9.11, where the trend between the two energies is similar during the load intervals which involve cracking in the flexure zone but the trend varies when the shear crack occurs.

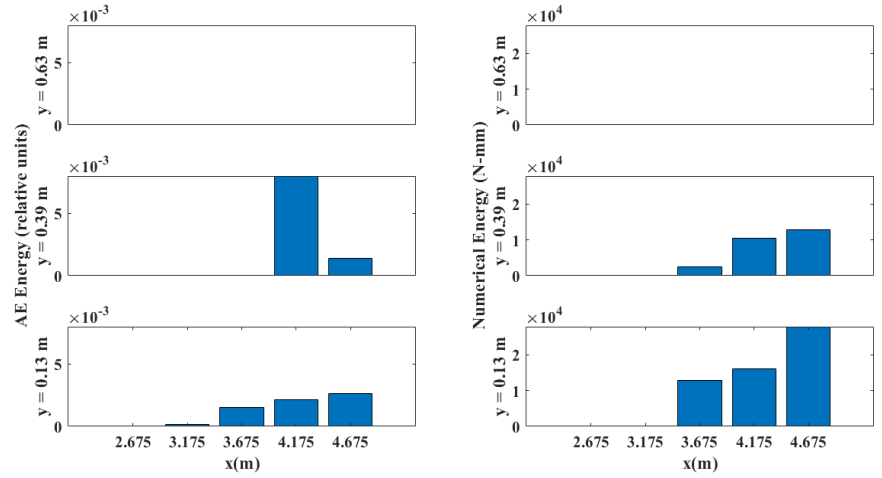

1100-1200 kN

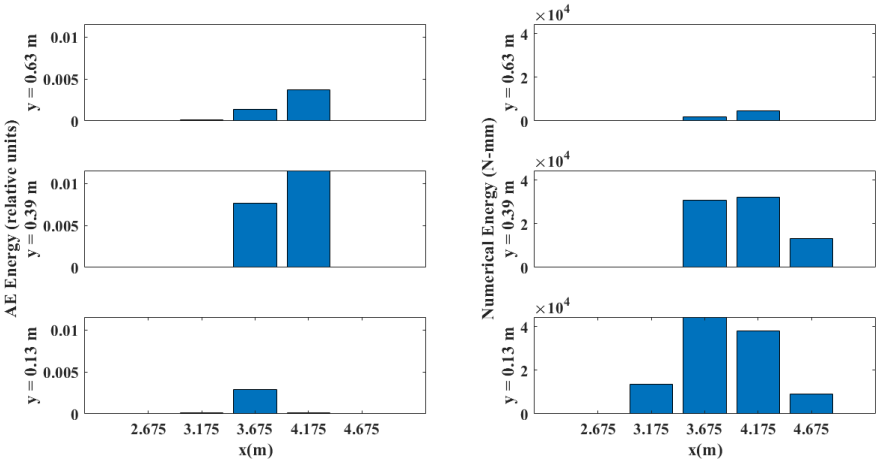

1200-1300 kN

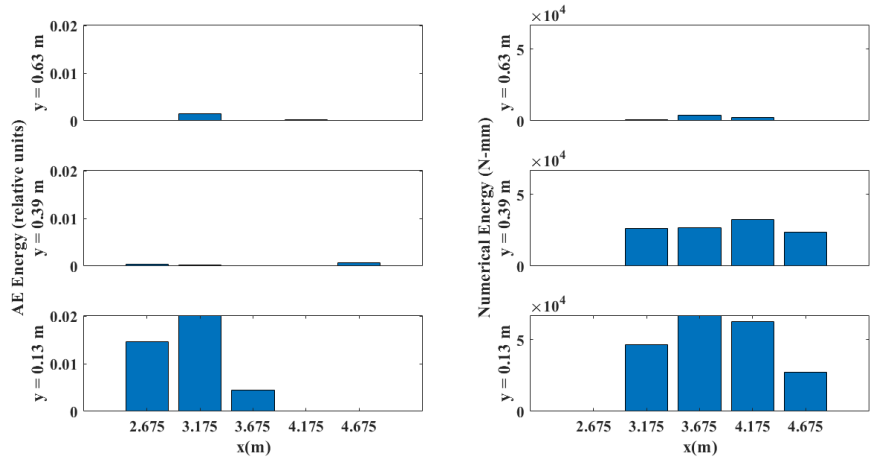

1300-1400 kN

Figure 9.9: Comparison between AE Energy and Numerical Energy for HPZ03

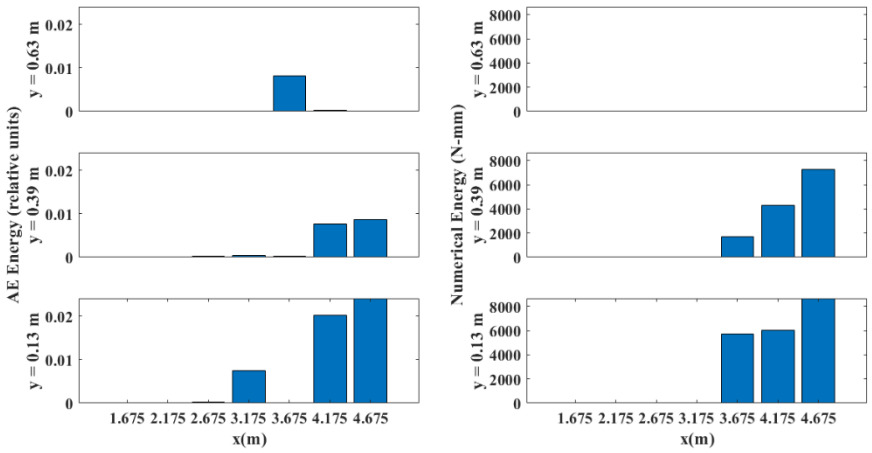

1150-1250 kN

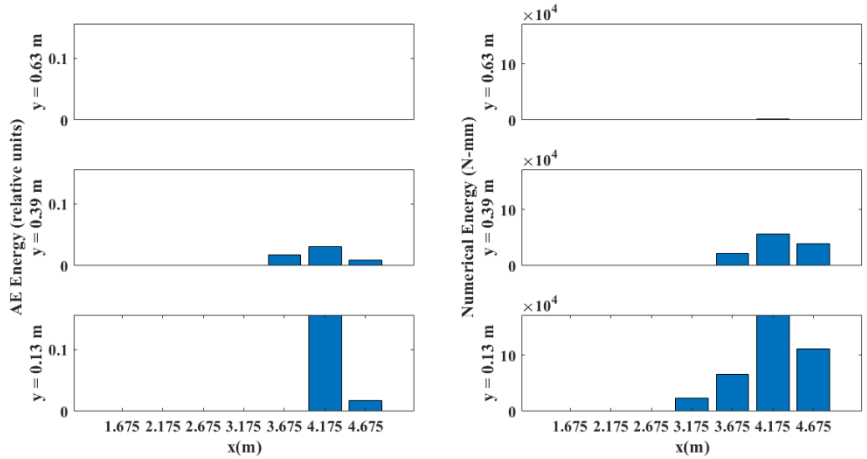

1250-1350 kN

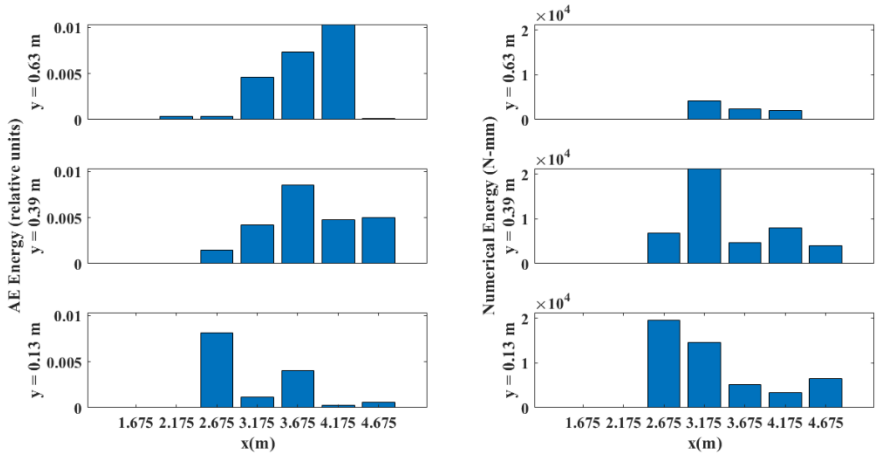

1450-1550 kN

Figure 9.10: Comparison between AE Energy and Numerical Energy for HPZ04

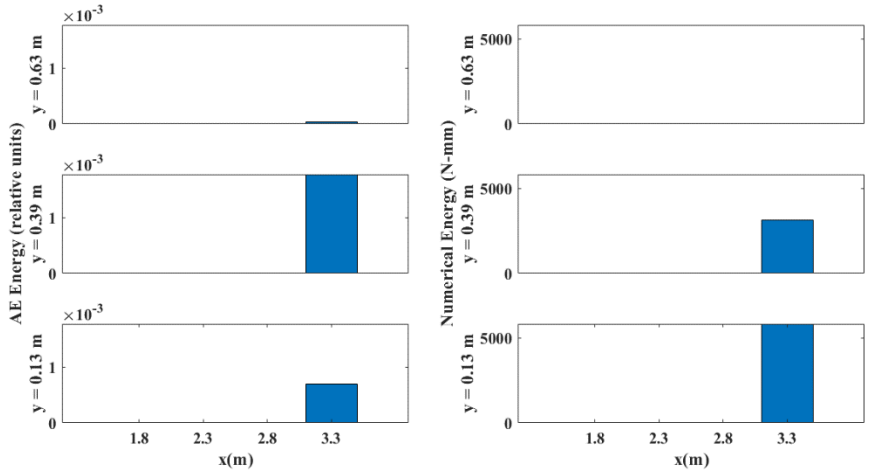

1150-1250 kN

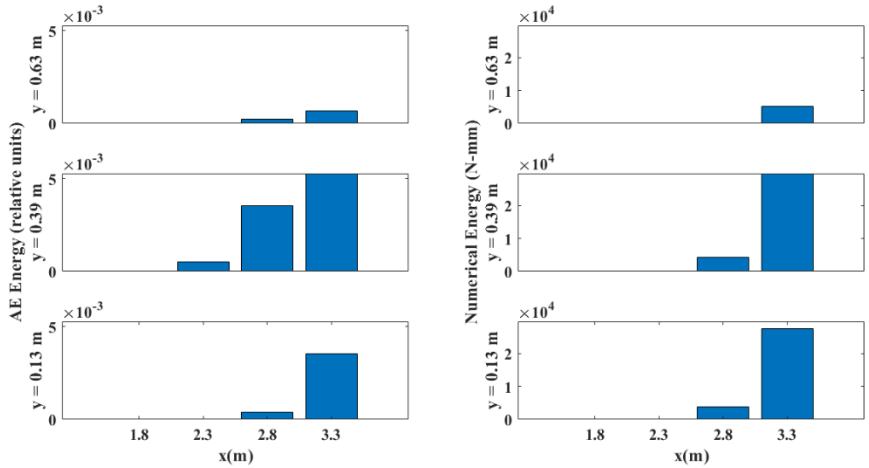

1150-1250 kN

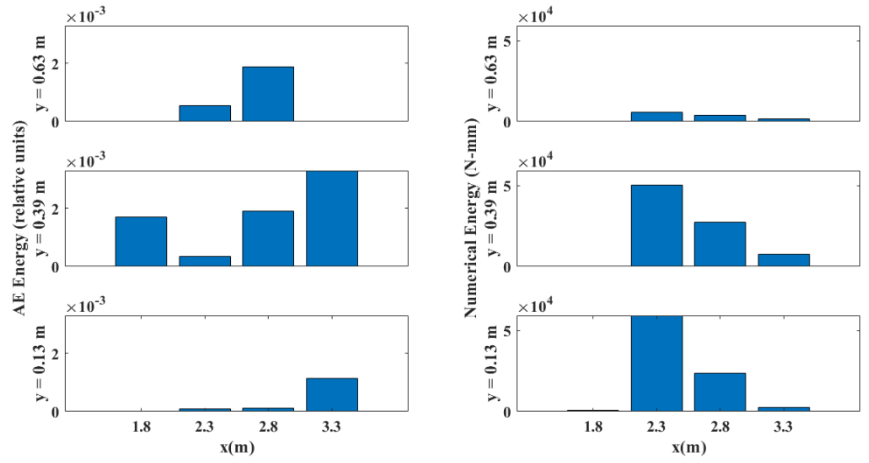

1350-1450 kN

Figure 9.11: Comparison between AE Energy and Numerical Energy for HPZ02

9.3 AE Energy as a Tool for Crack Monitoring

Acoustic Emission (AE) energy has already been used as a damage identification tool on a global scale, as discussed in Chapter 2.2. A similar observation can be made from the cumulative energy plots for HPZ03 and HPZ04 in Figure 5.3 and Figure 5.4. The cumulative AE energy presents a spike in value even before the crack is detected by the DIC measurements. This is because AE sensors are also able to detect microcracks inside the concrete.

In this thesis, the released AE energy is also used to investigate the crack at the local level. A nonlinear relationship is observed between the AE energy and the crack energy estimated using the numerical model. The nonlinear relationship can be the result of the difference in the behaviour of AE activity and the numerical model. AE activity is dominant when the crack is initiated, and in the softening stage, the amount of AE activity gets reduced. Whereas, in the numerical model the energy is continuously released over the softening branch (see Figure 9.12(a)). Further, from the zonal localization plots presented in Chapter 9.2, the occurrence of the flexure crack at the bottom flange and its propagation through the web can be tracked. The plots do not consider the complete non-linearity but are only calibrated to get the first flexure crack at the same time. The peak energy bar starts at the bottom right corner of the plot (Figure 9.9), then the peak moves upwards and to the left as load increases. This is in agreement with the experimental observations. The results also show a good spatial comparison between the total AE energy and numerical energy.

AE energy is also able to predict the occurrence of the flexure crack before the numerical model as shown in Figure 9.5-Figure 9.7. On average, for Helperzoom beams, AE results can predict the occurrence of the crack 10% of the cracking load in advance compared to the numerical result. A possible reason for this can be that in this thesis the Hordijk curve is used to model the concrete behaviour in tension. Thus, the concrete behaves linearly before the stress reaches the tensile stress and then the element cracks, as shown in Figure 9.12(a). Whereas, in reality, the microcracks start to occur in a small failure zone where the crack is expected to occur much before the failure. As per the Model Code [55], the concrete microcracks start to occur at around 90% of the tensile strength.

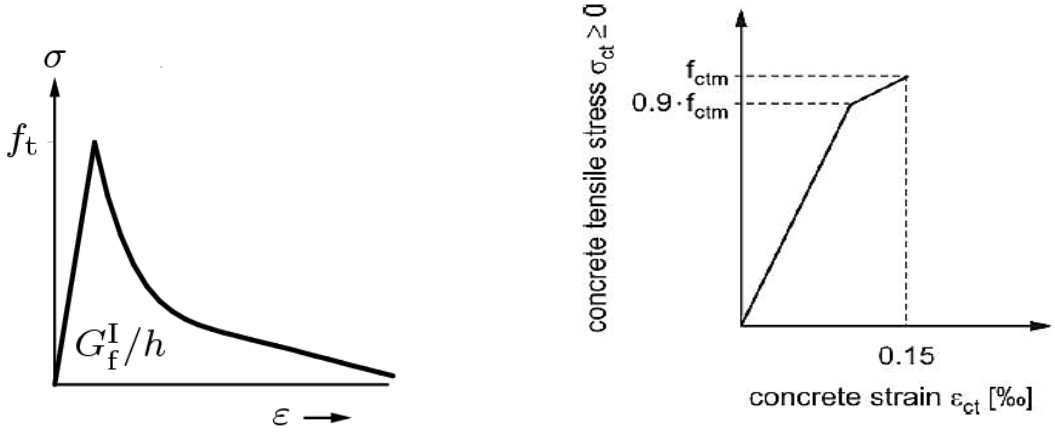

(a) Hordijk Curve [48] (b) Model Code 2010 [55]

Figure 9.12: Stress-Strain Behaviour of Concrete

AE energy estimated considers the AE events due to tension as well as friction. In order to track the energy released due to cracking only a comparison should be made considering the AE activities due to tension only. Figure 9.13 shows the zonal comparison plot including total AE energy, tensile AE energy and the numerical energy for HPZ03 between 1200 kN to 1300 kN. For tensile AE energy, the AE events related to tension are separated using the clustering methodology in Chapter 6. The tensile AE energy does not compare well to the numerical energy. The total AE energy includes AE energy due to tension and friction. On the other hand, there is no such distinction in the energy estimated through the numerical model. This is because, in this thesis, a rotating crack approach is used to model the crack in the concrete, thus the crack is always perpendicular to the direction of the principal stress. Due to this reason, there is no shear stress between the crack and thus a friction component of the energy cannot be separated. Thus, in this thesis comparison is only made between the total AE energy and the numerical energy.

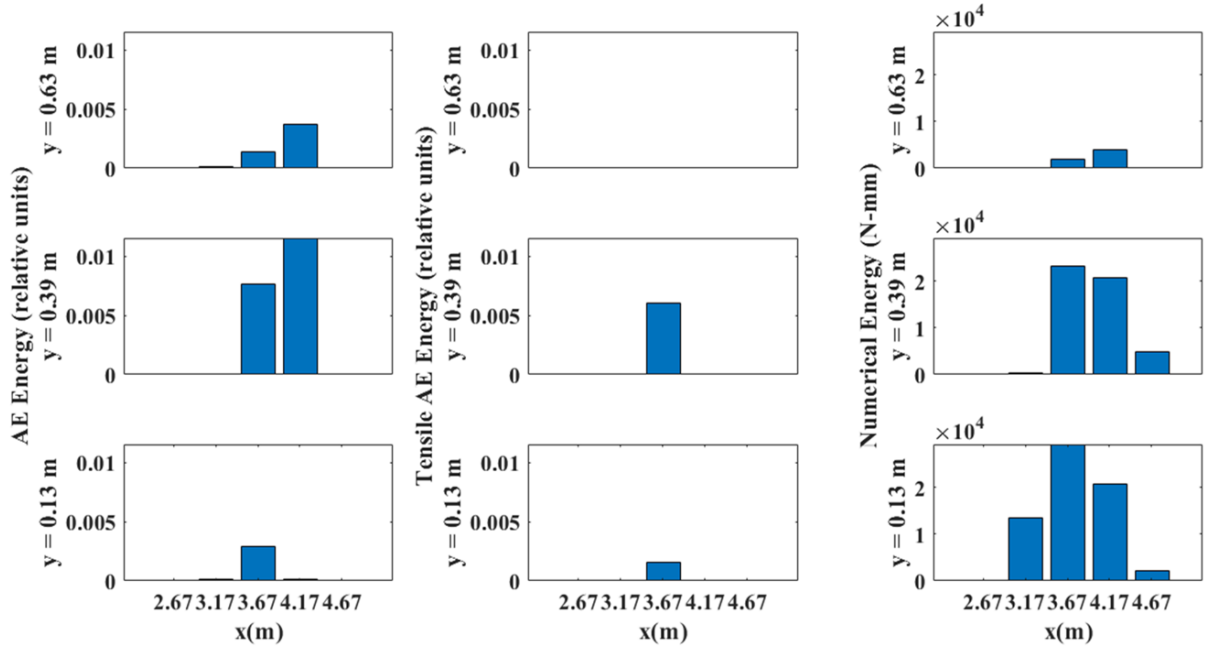

Figure 9.13: Zonal Comparison using Tensile AE Energy for HPZ03 (1200-1300 kN)

10 Conclusion

An investigation of the local energy release using acoustic emission and the finite element model was made in the previous chapters. The key concluding remarks from this study are reviewed in this chapter.

1. Bivariate parameter-based methods, like Gaussian Model, are unable to detect minor differences in the AE signal, with a similarity of less than 50 % to signal-based clustering. The multivariate analysis method like principal component analysis performs better than bivariate methods with a similarity of 56%. The partial power-based method, on the other hand, is efficient with a similarity of over 75% to the signal-based method. Additionally, the partial power-based method takes a couple of minutes to process compared to signal-based which takes more than an hour on average.
2. The material attenuation factor (α) of 2.473 m^{-1} is estimated based on the measurements in the uncracked concrete. Crack attenuation factor (C.A.F.) is defined to measure the attenuation through crack using the AST measurements. The results predict the occurrence of the crack 50 kN in advance, for the case of HPZ03, compared to source localization results, showing that AST measurements are sensitive to strain changes within concrete.
3. The proposed methodology for energy released at the integration point in the numerical model using the rotating crack approach for crack modelling can be used to estimate the local crack energy release. For a notched beam model fracture energy at the local level was estimated with a difference of 5% when compared to fracture energy at specimen level.
4. AE energy on average predicts the occurrence of the crack 10% in advance of the cracking load numerically. A close relationship between AE energy and release of fracture energy is observed for all the four beams. A nonlinear relationship is observed between the AE energy and the numerical fracture energy. The non-linearity is similar for all the four beams, with a spike in AE energy at the start of the crack and after around 40% of the maximum numerical energy no significant increase in AE energy was observed.
5. Following the zonal localization plots, AE can estimate the energy release along the crack. The energy release trend for AE and the numerical model with increasing load is similar when the flexure cracks are generated, but a relatively poor spatial comparison is observed when the comparison is made at a shear crack.
6. When using the rotating crack approach to model cracking behaviour in concrete, total AE energy should be used to compare the energy release trend. This is because while AE energy can still be divided into two parts, one related to tension and other related to friction, no such division is possible for rotating crack model.

11 Recommendation

Mounting on the work presented in this thesis, few recommendations are made for future researchers as an idea to delve further into the local energy release due to cracking in concrete:

1. The clustering methods used in this thesis, show that signal-based clustering methods can pick differences in AE events much better than the parameter-based methods, but the signal-based methods are time-consuming. In this regard, a novel partial power-based method for AE source classification is proposed, which should be investigated further for different frequency intervals. The results from the signal-based classification methods can be used to train and validate the method. This can help attain lower computation cost without compromising the accuracy of the classification method.
2. In this thesis, an approach to estimate the energy release through a crack is discussed. But, the AST measurements made during the experiment were inconsistent across sensors and thus were not used to correct the energy. Additionally, it is also shown that the crack attenuation factor (CAF) is sensitive to the strain changes in concrete (Chapter 7.2.2). In further studies, controlled experiments with respect to the source and receiver coupling and the crack strains should be conducted. Using the experimental results an empirical relation between the strain and attenuation factor can be established.
3. Rotating crack approach is used to model cracking behaviour in this thesis. Thus, there is no distinction in the part of the energy that belongs to tension and friction, a distinction which is possible in case of AE energy. In future, a fixed crack approach to model cracking behaviour in concrete can be used. It will allow dividing the numerical energy into the crack opening and friction components, and also will help capture the shear behaviour better.
4. A Hordijk curve is used to model the tension behaviour in this thesis. The linear pre-cracking behaviour of the crack model is unable to capture the microcracking activities in concrete. As a step further, other constitutive models, like Model Code 2010 in DIANA, can be used to imitate the microcracking behaviour.

References

[1] A. Reitsema, M. Lukovic, and D. Hordijk, “Towards Slender , Innovative Concrete Structures for Replacement of Existing Structures,” in *fib Symposium 2016 Performance-Based Approaches for Concrete Structures, Capetown*, 2016, no. January.

[2] L. Yan and N. Chouw, “Behavior and analytical modeling of natural flax fibre-reinforced polymer tube confined plain concrete and coir fibre-reinforced concrete,” *J. Compos. Mater.*, vol. 47, no. 17, pp. 2133–2148, 2013, doi: 10.1177/0021998312454691.

[3] R. E. Melchers, “ASSESSMENT OF EXISTING STRUCTURES—APPROACHES AND RESEARCH NEEDS,” *J. Struct. Eng.*, vol. 127, no. April, pp. 406–411, 2001.

[4] M. Holický *et al.*, *Innovative Methods for the Assessment of Existing Structures*. Czech Technical University, Prague, 2012.

[5] M. Mitra and S. Gopalakrishnan, “Guided wave based structural health monitoring: A review,” *Smart Mater. Struct.*, vol. 25, no. 5, 2016, doi: 10.1088/0964-1726/25/5/053001.

[6] D. Balageas, “Introduction to structural health monitoring,” 2006.

[7] W. Ostachowicz and J. Guemes, Eds., *New Trends in Structural Health Monitoring*. CISM Courses and Lectures International Centre for Mechanical Sciences.

[8] V. Giurgiutiu, *Structural Health Monitoring with Piezoelectric Wafer Active Sensors*, Second. Elsevier, 2014.

[9] M. Ohtsu, “The history and development of acoustic emission in concrete engineering,” *Mag. Concr. Res.*, vol. 48, no. 177, pp. 321–330, 1996.

[10] K. M. Holford, “Acoustic Emission- Basic Principles and Future Directions,” *Strain*, vol. 36, no. 2, pp. 51–54, 2000.

[11] C. U. Grosse and M. Ohtsu, *Acoustic emission testing: Basics for Research-Applications in Civil Engineering*. Springer Science & Business Media, 2008.

[12] H. Pham and H. Wang, *Springer Series in Reliability Engineering*. 2006.

[13] “Introduction to Acoustic Emission Testing.” https://www.nde-ed.org/EducationResources/CommunityCollege/Other Methods/AE/AE_Intro.php.

[14] A. Behnia, H. K. Chai, and T. Shiotani, “Advanced structural health monitoring of concrete structures with the aid of acoustic emission,” *Constr. Build. Mater.*, vol. 65, pp. 282–302, 2014, doi: 10.1016/j.conbuildmat.2014.04.103.

[15] C. Van Steen, L. Pahlavan, M. Wevers, and E. Verstrynge, “Localisation and characterisation of corrosion damage in reinforced concrete by means of acoustic emission and X-ray computed tomography,” Elsevier Ltd, 2019.

[16] T. Kundu, “Acoustic source localization,” *Ultrasonics*, vol. 54, no. 1, pp. 25–38, 2014, doi: 10.1016/j.ultras.2013.06.009.

[17] J. F. Labuz, H. S. Chang, C. H. Dowding, and S. P. Shah, “Parametric Study of Acoustic Emission Location Using Only Four Sensors,” *Rock Mech. Rock Eng.*, no. 21, pp. 139–148, 1988.

[18] K. Ohno and M. Ohtsu, “Crack classification in concrete based on acoustic emission,” *Constr. Build. Mater.*, vol. 24, no. 12, pp. 2339–2346, 2010, doi: 10.1016/j.conbuildmat.2010.05.004.

[19] A. Farhidzadeh, S. Salamone, and P. Singla, “A probabilistic approach for damage identification and crack mode classification in reinforced concrete structures,” *J. Intell. Mater. Syst. Struct.*, vol. 24, no. 14, pp. 1722–1735, 2013, doi: 10.1177/1045389X13484101.

[20] C. Van Steen, M. Wevers, and E. Verstrynge, “Clustering of acoustic emission signals for fracture monitoring during accelerated corrosion of reinforced concrete prisms,” in *10th International Conference on Fracture Mechanics of Concrete and Concrete Structures*, 2019, doi: 10.21012/fc10.235554.

[21] G. Manson, K. Worden, K. Holford, and R. Pullin, “Visualisation and dimension reduction

of acoustic emission data for damage detection," *J. Intell. Mater. Syst. Struct.*, vol. 12, no. 8, pp. 529–536, 2001, doi: 10.1106/UD4L-UPGC-WG29-A34L.
[22] M. Ohtsu, T. Isoda, and Y. Tomoda, "Acoustic Emission Techniques Standardized for Concrete Structures," *J. Acoust. Emiss.*, vol. 25, pp. 21–32, 2007.
[23] D. G. Aggelis, "Classification of cracking mode in concrete by acoustic emission parameters," *Mech. Res. Commun.*, vol. 38, no. 3, pp. 153–157, 2011, doi: 10.1016/j.mechrescom.2011.03.007.
[24] E. Pomponi and A. Vinogradov, "A real-time approach to acoustic emission clustering," *Mech. Syst. Signal Process.*, vol. 40, no. 2, pp. 791–804, 2013, doi: 10.1016/j.ymssp.2013.03.017.
[25] S. Yuyama, Z. wang Li, Y. Ito, and M. Arazoe, "Quantitative analysis of fracture process in RC column foundation by moment tensor analysis of acoustic emission," *Constr. Build. Mater.*, vol. 13, no. 1, pp. 87–97, 1999, doi: 10.1016/S0950-0618(99)00011-2.
[26] A. Carpinteri, G. Lacidogna, G. Niccolini, and S. Puzzi, "Critical defect size distributions in concrete structures detected by the acoustic emission technique," *Meccanica*, vol. 43, no. 3, pp. 349–363, 2008, doi: 10.1007/s11012-007-9101-7.
[27] L. Calabrese, G. Campanella, and E. Proverbio, "Use of Cluster Analysis of Acoustic Emission Signals in Evaluating Damage Severity in Concrete Structures," *J. Acoust. Emiss.*, vol. 28, pp. 129–141, 2010.
[28] E. N. Landis and L. Baillon, "Experiments to Relate Acoustic Emission Energy to Fracture Energy of Concrete," *J. Eng. Mech.*, vol. 128, no. 6, pp. 698–702, 2002.
[29] B. K. R. Prasad and R. V. Sagar, "Relationship between AE Energy and Fracture Energy of Plain Concrete Beams : Experimental Study," vol. 20, no. March, pp. 212–220, 2008, doi: 10.1061/(ASCE)0899-1561(2008)20.
[30] S. Muralidhara, B. K. R. Prasad, H. Eskandari, and B. L. Karihaloo, "Fracture Process Zone Size and True Fracture Energy of Concrete Using Acoustic Emission," *Constr. Build. Mater.*, vol. 24, pp. 479–486, 2010.
[31] Y. Lu and Z. Li, "Study of the Relationship between Concrete Fracture Energy and AE Signal Energy under Uniaxial Compression," no. May, 2012, doi: 10.1061/(ASCE)MT.1943-5533.0000418.
[32] R. V. Sagar and B. K. R. Prasad, "AE energy release during the fracture of HSC beams," vol. 9831, no. 6, pp. 419–435, 2009, doi: 10.1680/macr.2009.61.6.419.
[33] R. V. Sagar and B. K. R. Prasad, "An Experimental Study on Acoustic Emission Energy as a Quantitative Measure of Size Independent Specific Fracture Energy of Concrete Beams," *Constr. Build. Mater.*, no. 25, pp. 2349–2357, 2011.
[34] D. O. Harris and R. L. Bell, "The Measurement and Significance of Energy in Acoustic Emission Testing," *Exp. Mech.*, vol. 17, pp. 347–353, 1977.
[35] Réunion Internationale des Laboratoires d'Essais et de Recherches sur les Matériaux et les Constructions (RILEM) Committee 50-FMC, "Determination of the Fracture Energy of Mortar and Concrete by means of Three-Point Bend Tests on Notched Beams," *Mater. Struct.*, vol. 18, no. 106, pp. 285–290, 1985, doi: 10.1007/BF00962380.
[36] K. Otsuka and H. Date, "Fracture process zone in concrete tension specimen," vol. 65, pp. 1–13, 2000.
[37] A. Tobias, "Acoustic-emission source location in two dimensions by an array of three sensors," *Non-Destructive Test.*, vol. 9, no. 1, pp. 9–12, 1976, doi: 10.1016/0029-1021(76)90027-X.
[38] W. H. Sachse and S. Sancar, "Acoustic emission source location on plate-like structures using a small array of transducers," *J. Acoust. Soc. Am.*, vol. 81, no. 1, pp. 206–206, 1987, doi: 10.1121/1.394998.
[39] F. Zhang, "Evaluation of acoustic emission monitoring of existing concrete structures," Delft University of Technology, 2017.

[40] B. Gutenberg and C. F. Richter, *Seismicity of the Earth and Associated Phenomena*. Princeton University Press, 1954.
[41] J. H. Kurz, F. Finck, C. U. Grosse, and H. W. Reinhardt, "Stress drop and stress redistribution in concrete quantified over time by the b-value analysis," *Struct. Heal. Monit.*, vol. 5, no. 1, pp. 69–81, 2006, doi: 10.1177/1475921706057983.
[42] "JCMS-III B5706. Monitoring method for active cracks in concrete by acoustic emission," *Japan Fed. Constr. Mater. Ind.*, 2003.
[43] R. Vidya Sagar, "Support vector machine procedure and Gaussian mixture modelling of acoustic emission signals to study crack classification in reinforced concrete structures," in *10th International Conference on Fracture Mechanics of Concrete and Concrete Structures, FraMCoS-X*, doi: 10.21012/fc10.235431.
[44] M. F. M. Yusof, C. K. E. Nizwan, S. A. Ong, and M. Q. M. Ridzuan, "Clustering of frequency spectrums from different bearing fault using principle component analysis," *MATEC Web Conf.*, vol. 90, 2016, doi: 10.1051/matecconf/20179001006.
[45] J. O. Owino and L. J. Jacobs, "Attenuation Measurements in Cement-Based Materials Using Laser Ultrasonics," *J. Eng. Mech.*, vol. 125, no. June, pp. 637–647, 1999.
[46] B. M. Das and G. V. Ramana, *Principles of Soil Dynamics*. Cengage Learning, 2011.
[47] S. Suharsono and A. R. Samsudin, "The attenuation effects of surface-wave propagations on rockmass using SASW method," *Bull. Geol. Soc. Malaysia*, vol. 46, no. May, pp. 475–478, 2003, doi: 10.7186/bgsm46200377.
[48] D. Ferreira and J. Manie, Eds., *Diana Documentation 10.3*. Diana FEA, 2019.
[49] E. O. L. Lantsoght *et al.*, "Measurement Report of Prestressed Beams from Helperzoom Viaduct," 2020.
[50] E. O. L. Lantsoght *et al.*, "Analysis Report of Prestressed Beams from Helperzoom Viaduct," 2020.
[51] Y. Li and H. Wu, "2012 International Conference on Solid State Devices and Materials Science A Clustering Method Based on K-Means Algorithm," *Phys. Procedia*, vol. 25, pp. 1104–1109, 2012, doi: 10.1016/j.phpro.2012.03.206.
[52] C. M. R. Fowler, "The solid earth: an introduction to global geophysics," *solid earth an Introd. to Glob. Geophys.*, 1990, doi: 10.1029/90e000309.
[53] M. A. N. Hendriks, A. de Boer, and B. Belletti, "Guidelines for nonlinear finite element analysis of concrete structures," *Rijkswaterstaat Technisch Document (RTD), Rijkswaterstaat Centre for Infrastructure, RTD, 1016:2012*, 2017.
[54] "Local Appraoch to Fatigue of Concrete, Doctoral Dissertation," Delft University of Technology, 1991.
[55] *fib Model Code for Concrete Structures 2010*. 2013.

Appendix A: Comparison Results for HPZ01

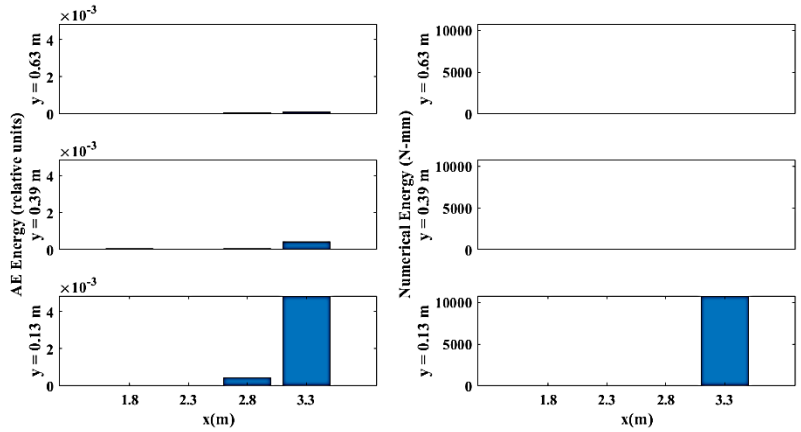

900-1000 kN

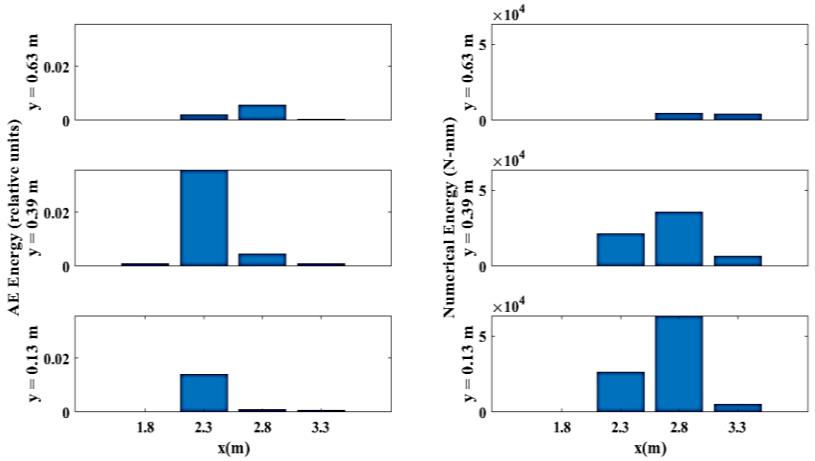

1150-1250 kN

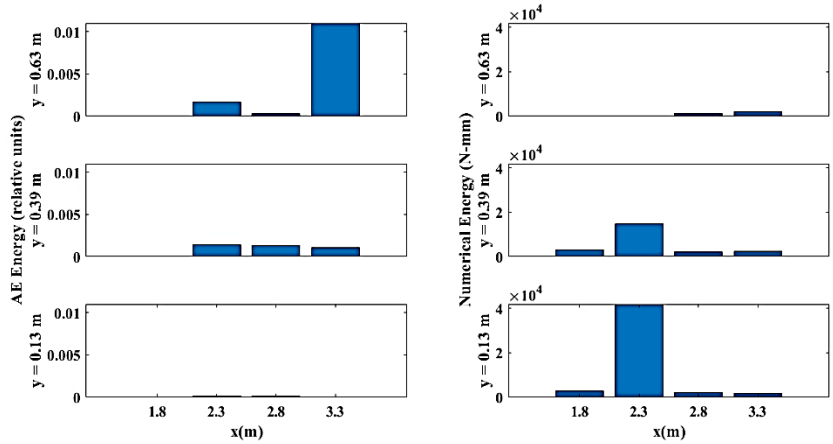

1250-1300 kN

Figure A1: Zonal Comparison plos for HPZ01

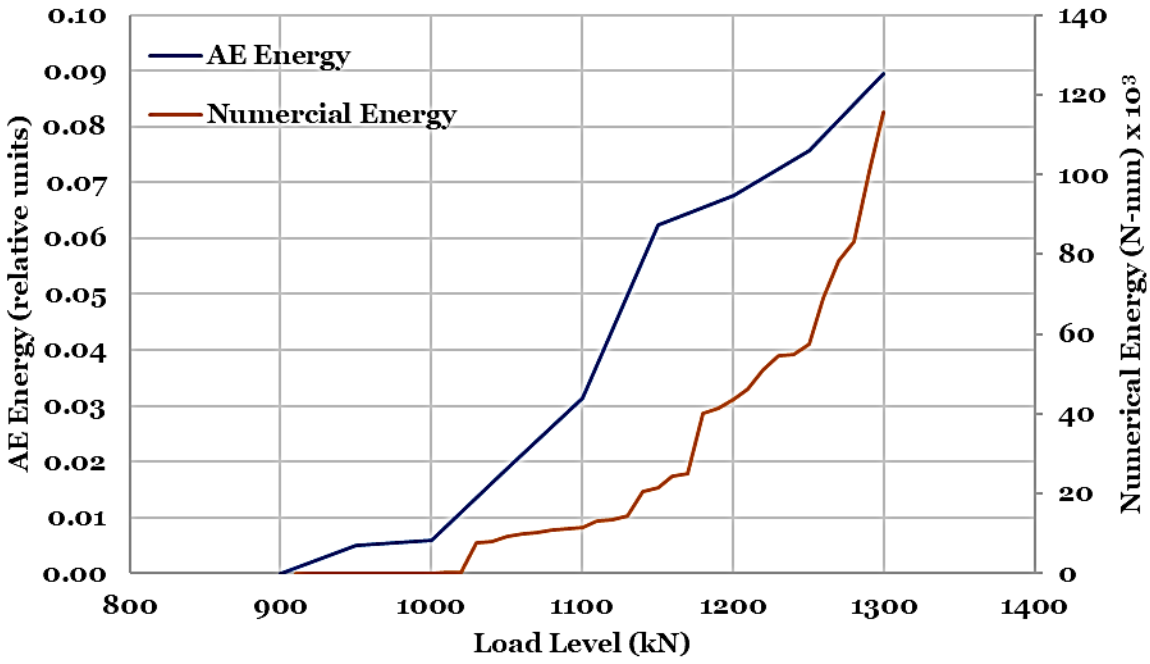

Figure A2: Energy Release in the Flexure Zone for HPZ01